

# A Pre-Landing Assessment of Regolith Properties at the InSight Landing Site

---

Paul Morgan<sup>1</sup>, Matthias Grott<sup>2</sup>, Brigitte Knapmeyer-Endrun<sup>3</sup>, Matt Golombek<sup>4</sup>, Pierre Delage<sup>5</sup>, Philippe Lognonné<sup>6</sup>, Sylvain Piqueux<sup>4</sup>, Ingrid Daubar<sup>4</sup>, Naomi Murdoch<sup>7</sup>, Constantinos Charalambous<sup>8</sup>, William T. Pike<sup>8</sup>, Nils Müller<sup>4</sup>, Axel Hagermann<sup>9</sup>, Matt Siegler<sup>10</sup>, Roy Lichtenheldt<sup>11</sup>, Nick Teanby<sup>12</sup>, Sharon Kedar<sup>4</sup>

**Corresponding Author:** Paul Morgan

Colorado School of Mines, 1801 19<sup>th</sup> St., Golden, CO 80401, USA

Email: [morgan@mines.edu](mailto:morgan@mines.edu)

Tel: [+1] 303 384 2648

## **Affiliations:**

<sup>1</sup> Colorado Geological Survey, Colorado School of Mines, 1801 19<sup>th</sup> St., Golden, CO 80401, USA

<sup>2</sup> DLR Institute for Planetary Research, Rutherfordstr. 2, 12489 Berlin, Germany

<sup>3</sup> Max Plank Institute for Solar System Research, Department Planets and Comets, Justus-von-Liebig-Weg 3, 37077 Göttingen, Germany

<sup>4</sup> Jet Propulsion Laboratory, California Institute of Technology, 4800 Oak Grove Dr., Pasadena, CA 91109, USA

<sup>5</sup> Ecole des Ponts ParisTech, Laboratoire Navier (CERMES), Paris, France

<sup>6</sup> Institut de Physique du Globe de Paris – Sorbonne Paris Cité, Université Paris Diderot, 35 rue Hélène Brion, 75013 PARIS, France

<sup>7</sup> Institut Supérieur de l’Aéronautique et de l’Espace (ISAE-SUPAERO), Université de Toulouse, 31055 Toulouse Cedex 4, France

<sup>8</sup> Imperial College London, Faculty of Engineering, Department of Electrical and Electronic Engineering, London, UK

<sup>9</sup> The Open University, Faculty of Science Technology and Mathematics, Walton Hall, Milton Keynes MK7 6AA, UK

<sup>10</sup> Southern Methodist University, Deadman College of Humanities and Sciences, PO Box 750235, Dallas, TX 75275-0235, USA

<sup>11</sup> DLR Institute for System Dynamics and Control, Münchner Straße 20, 82234 Oberpfaffenhofen-Weßling, Germany

<sup>12</sup> University of Bristol, School of Earth Sciences, Wills Memorial Building, Queens Road, Clifton BS8 1RJ, UK

## **Acknowledgements**

PM was supported for this work by subcontract no. 1479970 for the InSight Mission from the Jet Propulsion Laboratory. A portion of the work described in this paper was supported by the InSight Project at the Jet Propulsion Laboratory, California Institute of Technology, under a contract with the National Aeronautics and Space Administration. This is InSight Contribution Number 39.

## 37 Abstract

38 This article discusses relevant physical properties of the regolith at the Mars InSight landing site as  
39 understood prior to landing of the spacecraft. InSight will land in the northern lowland plains of Mars,  
40 close to the equator, where the regolith is estimated to be  $\geq 3$ -5 m thick. These investigations of  
41 physical properties have relied on data collected from Mars orbital measurements, previously collected  
42 lander and rover data, results of studies of data and samples from Apollo lunar missions, laboratory  
43 measurements on regolith simulants, and theoretical studies. The investigations include changes in  
44 properties with depth and temperature. Mechanical properties investigated include density, grain-size  
45 distribution, cohesion, and angle of internal friction. Thermophysical properties include thermal inertia,  
46 surface emissivity and albedo, thermal conductivity and diffusivity, and specific heat. Regolith elastic  
47 properties not only include parameters that control seismic wave velocities in the immediate vicinity of  
48 the InSight lander but also coupling of the lander and other potential noise sources to the InSight  
49 broadband seismometer. The related properties include Poisson's ratio, P- and S-wave velocities,  
50 Young's modulus, and seismic attenuation. Finally, mass diffusivity was investigated to estimate gas  
51 movements in the regolith driven by atmospheric pressure changes. Physical properties presented here  
52 are all to some degree speculative. However, they form a basis for interpretation of the early data to be  
53 returned from the InSight mission.

54

## 55 Keywords

56 Mars, Regolith, Physical Properties, InSight Landing Site

57 Table of Contents

58 *Acknowledgements* ..... 1

59 Abstract..... 2

60 Keywords ..... 2

61 Introduction ..... 5

62 1. Regolith at the InSight Landing Site ..... 7

63 1.1. Landing Site Overview..... 7

64 1.2. Rock Abundance ..... 9

65 1.3. Regolith Structure Summary..... 10

66 2. Regolith Soil Mechanical Properties..... 10

67 2.1 Introduction ..... 10

68 **2.2 Density** ..... 11

69 16

70 2.3 Cohesion ..... 16

71 2.4 Internal Friction Angle ..... 17

72 2.5. Grain size Distribution ..... 19

73 3. Regolith Thermophysical Properties ..... 21

74 3.1. Surface Emissivity..... 22

75 3.2. Surface Thermal Inertia..... 24

76 3.3. Surface Albedo ..... 26

77 3.4. Thermal Conductivity ..... 27

78 3.5. Specific Heat..... 34

79 3.6. Thermal Diffusivity ..... 35

80      4.    Regolith Elastic Properties .....36

81      4.1.   Seismic Velocities and Poisson’s ratio ..... 36

82      4.2.   Elastic Modulus ..... 42

83           43

84      4.3.   Attenuation Factor ..... 43

85      5.    Mass Diffusivity .....48

86      5.1.   Gas Interactions in Porous Media ..... 49

87      5.2.   Estimating Pore Sizes ..... 51

88      5.3.   Gas Mean Free Path and Range at Landing Site ..... 52

89      5.4.   Calculated Range of Mass Diffusivity at Landing Site ..... 52

90      5.5.   Comparison with Experimental Data ..... 53

91      5.6.   Final Observations..... 54

92      6.    Summary and Conclusions .....56

93      7.    References .....59

94      8.    Appendix .....73

95

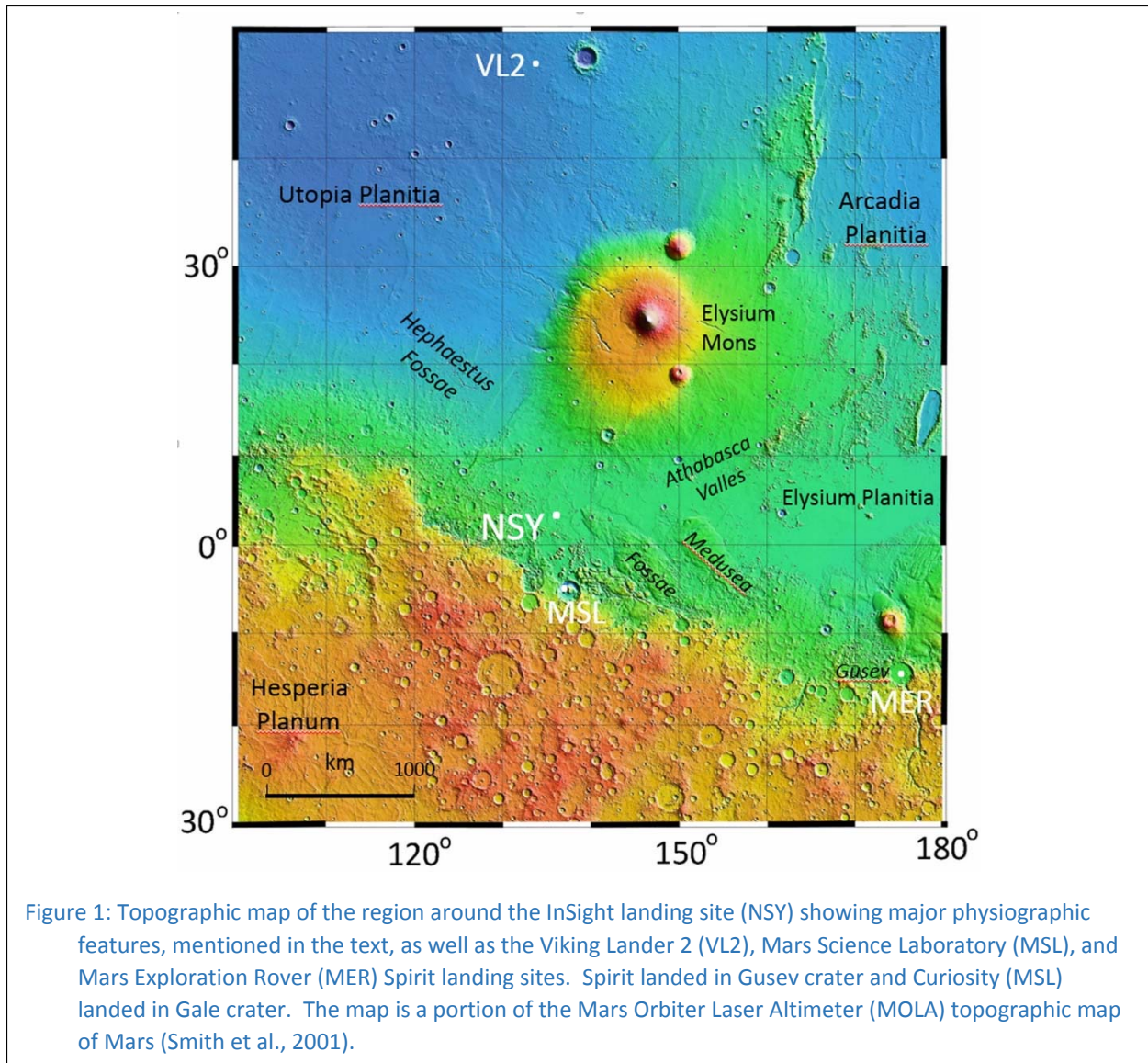
## 96      **Introduction**

97      The InSight mission is the first dedicated geophysical mission to another planet. InSight (Interior  
98      Exploration using Seismic Investigations, Geodesy and Heat Transport) will place a single geophysical  
99      lander on Mars to study its deep interior and to provide information relevant to the fundamental  
100     processes of terrestrial planet formation and evolution (Banerdt et al., 2013). This article discusses  
101     physical properties of the Mars regolith at the InSight landing site based upon information available  
102     approximately one year prior to launch, and eighteen months prior to touchdown of the InSight lander.  
103     The InSight mission represents many years of engineering and scientific design and preparation, based to  
104     some degree on the properties of the regolith at the landing site. Most of the scientific data to be  
105     collected by instruments on the InSight lander will be filtered by the regolith in the immediate vicinity of  
106     the landing site. Therefore to design these instruments and to make realistic predictions of the range of  
107     data characteristics that should be recorded by the instruments, a model of the physical properties of the  
108     landing site regolith has been required. As the science team approaches the final stages of preparation  
109     for first data return from the InSight Mission, we saw benefit in using a consistent set of regolith physical  
110     property values for any required data processing and early publications across the project. At least some  
111     of these property values will be revised at a later date with new data from the InSight instruments.

112     The InSight lander is based on a lander used for the successful Phoenix mission that was launched to  
113     Mars on August 4, 2007 and investigated near-surface ice in the Martian Arctic (Smith et al., 2009).  
114     Scientific instruments on the Phoenix lander have been replaced by a broad-band seismometer that will  
115     be placed on the surface of Mars, a heat-flow probe with an internal hammer mechanism that will  
116     hammer itself into the Martian regolith with an accompanying radiometer to determine the radiative  
117     surface temperature of the regolith close to the lander, and a precision tracking system. Additional  
118     instruments on the lander will measure orbital and local atmospheric parameters of Mars. Some regolith  
119     properties, such as radioactivity and magnetic properties have been omitted in this discussion because  
120     they were either not pertinent to the InSight Mission instruments or they lacked data at the regolith scale.

121     The InSight landing site is shown on a portion of Mars topography in Figure 1. The general landing area  
122     was chosen for basic operational reasons of being close to the equator for year-round solar power for the  
123     lander and smooth topography for the landing site. More specific details of landing site selection are  
124     given in the [Landing Site Overview](#) in section 2.1 below. Mars has two basic terrains, smooth northern  
125     lowland plains (“planitia”) and southern cratered highlands (“terra”), separated by the dichotomy

126 boundary. Four geologic eras have been assigned to terrains on Mars based on crater densities: Pre-  
127 Noachian, 4.5 – 4.1 Ga; Noachian, 4.1 – 3.7 Ga; Hesperian, 3.7 – 3.0 Ga; and Amazonian, 3.0 Ga – present.  
128 The landing site is in lowlands terrain of Early Hesperian or younger age, just north of the dichotomy  
129 boundary.



130 Following this introduction is a description of the regolith at the landing site including the criteria and  
131 process of landing site selection. This section is followed by four regolith physical property sections:  
132 Regolith Soil Mechanical Properties; Regolith Thermo-Physical Properties; Regolith Elastic Properties; and  
133 Mass Diffusivity. The paper closes with a summary and conclusions section. Sections were contributed  
134 by different authors or groups of authors according to their specialty. We have endeavored to make the

135 document flow as smoothly as possible, but it is primarily an informational article. However, what the  
136 paper lacks in style we hope that it contributes in utility.

## 137 **1. Regolith at the InSight Landing Site**

138 This section describes properties of the regolith essential for safe landing and operation of the  
139 spacecraft and instrument deployment.

### 140 **1.1. Landing Site Overview**

141 InSight will land in western Elysium Planitia on Hesperian plains just north of the dichotomy boundary  
142 (Golombek et al., 2017). This location satisfies the three dominant landing site engineering constraints,  
143 which are latitude (3°N-5°N), elevation (<-2.5 km with respect to the MOLA geoid), and a large smooth,  
144 flat surface to place a 130 km by 27 km landing ellipse. Other engineering constraints that are relevant to  
145 the geologic setting include: 1) a load bearing, radar reflective surface with thermal inertia >100–140 J/(m<sup>2</sup>  
146 K s<sup>1/2</sup>), slopes <15° and rock abundance <10% for safe landing and instrument deployment, and a broken  
147 up regolith >3 m thick to facilitate deployment of the heat flow probe (Golombek et al., 2017).

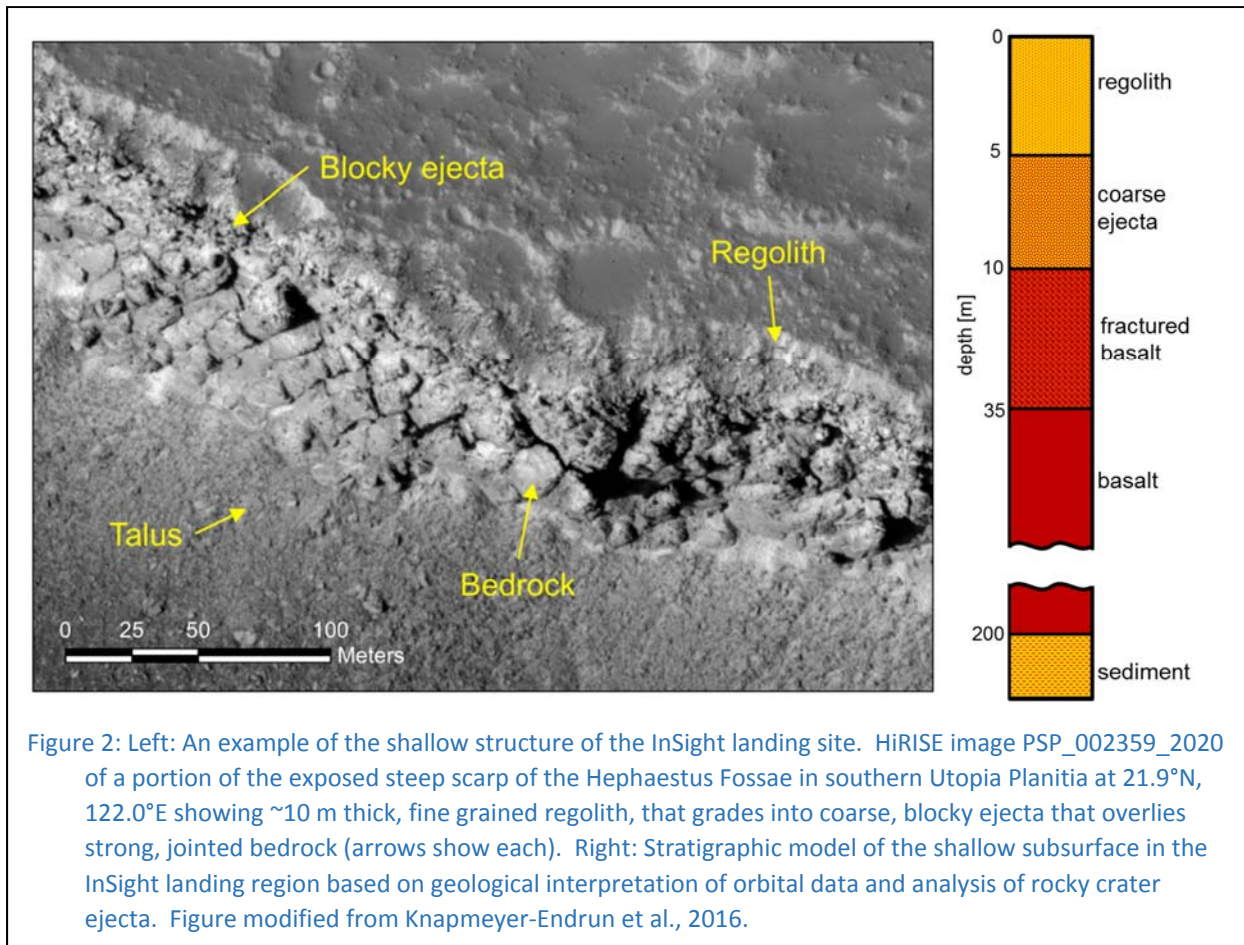
148 The InSight landing ellipse is located on smooth plains with Noachian highlands to the south and west,  
149 a ridge of Medusae Fossae Formation to the southeast and very young lavas from Athabasca Valles to the  
150 east (Golombek et al., 2017). The ellipse is located at 4.5°N, 135.9°E, about 540 km north of the Mars  
151 Science Laboratory landing site. The plains surface on which the InSight ellipse is located is mapped as  
152 Early Hesperian transition unit (eHt) by Tanaka et al. (2014) in the global geologic map of Mars, which  
153 could be sedimentary or volcanic. A volcanic interpretation of the plains is supported by: 1) the presence  
154 of rocks in the ejecta of fresh craters ~0.4 to 20 km diameter suggesting a strong competent layer ~4 to  
155 200 m deep with weaker material above and below (e.g., Golombek et al., 2013; Catling et al., 2011, 2012;  
156 Warner et al., 2017); 2) exposures of strong, jointed bedrock overlain by ~10 m of relatively fine grained  
157 regolith in nearby Hephaestus Fossae in southern Utopia Planitia at 21.9°N, 122.0°E (Golombek et al.,  
158 2013, 2017); 3) platy and smooth Late Hesperian to Early Amazonian lava flows up to 200 m thick mapped  
159 in 6 m/pixel visible images south of the landing site (Ansan et al., 2015); and 4) the presence of wrinkle  
160 ridges, which have been interpreted to be fault-propagation folds, in which slip on thrust faults at depth  
161 is accommodated by asymmetric folding in strong, but weakly bonded layered material (such as basalt  
162 flows) near the surface (e.g., Mueller and Golombek, 2004; Golombek and Phillips, 2010).

163 The landing ellipse has very low rock abundance (Golombek et al., 2017). Most rocks at the landing  
164 site are concentrated around rocky ejecta craters larger than 30 to 200 m diameter, but not around  
165 similarly fresh smaller craters (Golombek et al., 2013, 2017). Because ejecta is sourced from shallow  
166 depths,  $\sim 0.08$  times the diameter of the crater (Melosh, 1989), and based on the assumption that the  
167 surface morphology is fresh and not highly eroded, the onset diameter of rocky ejecta craters has been  
168 used to map the thickness of the broken up regolith. Results indicate a regolith that is 3-17 m thick  
169 (Warner et al., 2014, 2016, 2017), that grades into large blocky ejecta over strong intact basalts (Golombek  
170 et al., 2013, 2017). Because fresh craters larger than 2 km do not have rocky ejecta, material below the  
171 basalts at  $\sim 200$  m depth is likely weakly bonded sediments.

172 Surficial thermophysical properties of the landing site indicate that the soil that makes up the surface  
173 materials is similar to common weakly bonded soils on Earth and conducive to penetration by the heat  
174 flow probe (Golombek et al., 2017). The thermal inertia of the landing ellipse is about  $200 \text{ J}/(\text{m}^2 \text{ K s}^{1/2})$ ,  
175 the albedo is 0.25, and dust cover index is 0.94 (see Section 4.2, and Golombek et al., 2017). Comparison  
176 with the thermal inertias of previous landing sites and the soils at these sites (Golombek et al., 2008a)  
177 suggests the InSight landing site surfaces are composed of cohesionless sand or low cohesion soils  
178 (cohesions of less than a few kPa, angle of internal friction of  $30\text{-}40^\circ$ ), with bulk densities of  $\sim 1000$  to  $1600$   
179  $\text{kg}/\text{m}^3$ , particle sizes of  $\sim 150\text{-}250 \mu\text{m}$  (fine sand), that extend to a depth of at least several tens of  
180 centimeters, and with surficial dust layer less than 1–2 mm thick (Golombek et al., 2017).

181 The albedo and dust cover index are similar to dusty and low-rock abundance portions of the Gusev  
182 cratered plains, which are Hesperian lava flows with an impact generated regolith, modified by eolian  
183 processes (Golombek et al., 2006). Mapping of surface terrains in high-resolution images of the InSight  
184 landing site and surrounding areas, shows these terrains are similarly Hesperian lava flows with an impact  
185 generated regolith modified by eolian processes (Golombek et al., 2017; Warner et al., 2017).

186 An exposed escarpment of nearby Hephaestus Fossae (Figure 2) shows this near surface structure with  
187  $\sim 10$  m thick, relatively fine grained regolith, that grades into coarse, blocky ejecta with meter to ten-  
188 meter scale boulders that overlies strong, jointed bedrock. The grading of finer grained regolith into  
189 coarser, blocky ejecta is exactly what would be expected for a surface impacted by craters with a steeply  
190 dipping negative power-law size distribution in which smaller impacts vastly outnumber larger impacts  
191 that would excavate more deeply beneath the surface (e.g., Shoemaker and Morris, 1969; Hartmann et  
192 al., 2001; Wilcox et al., 2005).



193

## 194 1.2. Rock Abundance

195 The contrast between measurements of thermal emission from the surface at various wavelengths  
 196 using the Viking Orbiter Infrared Thermal Mapper (IRTM) and the Mars Global Surveyor spacecraft  
 197 Thermal Emission Spectrometer (TES) data have been used to determine the rock abundance (the  
 198 fractional area covered by high thermal inertia rocky material) at about 60 and 8 km/pixel scales  
 199 (Christensen, 1986; Nowicki and Christensen, 2007). With the rock abundance and the bulk thermal  
 200 inertia, the thermal inertia of the remaining soil, referred to as the fine-component thermal inertia (Kieffer  
 201 et al., 1977), has also been determined (Christensen, 1986; Nowicki and Christensen, 2007). Rock  
 202 abundance estimated from thermal differencing is 4% and 9% for IRTM pixels of ~60 km (Christensen,  
 203 1986) and around 4% (1%–7%) for TES pixels of ~8 km (Nowicki and Christensen, 2007) in the landing  
 204 ellipse. Because the thermal differencing estimates of rock abundance are relatively low for this area

205 (Christensen, 1986; Nowicki and Christensen, 2007), the fine component thermal inertia is only slightly  
206 lower than the bulk thermal inertia.

207 Rock abundance measured from shadows in HiRISE images fit to model exponential cumulative  
208 fractional area versus diameter curves in 150 m bins (Golombek et al., 2008b, 2012) also indicate a very  
209 low average rock abundance of 1-2% for the InSight landing site (Golombek et al., 2017), although rock  
210 abundance can increase to ~35% around rocky ejecta craters. Fragmentation theory in which the particle  
211 size distribution is described by a negative binomial function (Charalambous, 2014) was applied to the  
212 InSight landing site using cratering size-frequency measurements to derive a synthesized regolith with a  
213 size-frequency distribution similar to the exponential model for ~2-6% rock abundance (Charalambous et  
214 al., 2011; Golombek et al., 2017). The measurements and models of rock abundance combined with the  
215 thermal inertia observations all indicate a relatively fine-grained regolith with low rock abundance in the  
216 upper 5 m of the regolith at the landing site.

### 217 **1.3.Regolith Structure Summary**

218 In summary, the upper 5 m of regolith at the landing site are expected to be dominantly composed of  
219 nearly cohesionless fine basaltic sand, which contains few rocks. The regolith was produced by impact  
220 gardening of basalt flows with eolian sorting and transport of the sand. In contrast with lunar regolith,  
221 the sand grains are rounded to sub-rounded by saltation (e.g., McGlynn et al., 2011). With increasing  
222 depth, larger particles and rocks are expected to become more plentiful until the upper, relatively fine-  
223 grained regolith grades into a coarse-grained breccia or blocky ejecta that overlies fractured basalt flows.  
224 In addition, with increasing depth the effects of impact decreases and basalt would likely be less fractured.  
225 Below ~200 m basalt would transition to sediments or weakly bonded sedimentary rocks.

226

## 227 **2. Regolith Soil Mechanical Properties**

### 228 **2.1 Introduction**

229 The parameters used to characterize the mechanical properties of the regolith at the InSight landing  
230 site are considered in this section. They are also summarized in a table in the Appendix.

231 The Martian regolith is expected to be a complex mix of weathered, indurated, and windblown  
232 material (e.g., Putzig and Mellon, 2007), and apart from engineering safety considerations, the InSight  
233 landing site was chosen to facilitate penetration of the HP<sup>3</sup> thermal probe to a depth of 3-5 m into a  
234 column of fragmented regolith (Golombek et al., 2017). Comparison with data from other landed missions  
235 and orbiters indicates that the regolith is largely cohesionless, has angle of internal friction close to that  
236 of sand (30-40°), and particles are expected to be rounded due to erosion by wind. Indeed, eolian activity  
237 on Mars has occurred throughout geologic time. The surface layer has been subjected to eolian activity  
238 and impacts: after each impact sand size grains have been saltated and rounded and sorted and the entire  
239 column of material has rounded (sub-rounded) grains. As such, the region may be viewed as an eolian  
240 deposit which may be the result of potentially several inflation and deflation periods. Given the values of  
241 thermal inertia ( $200 \text{ J}/(\text{m}^2 \text{ K}^1 \text{ s}^{1/2})$ ), albedo (0.25) and dust cover index (0.94) in the InSight landing place,  
242 and based on comparison with the thermal inertias of previous landing sites, the InSight surfaces are  
243 composed of cohesionless sand or low cohesion soils with particle sizes of ~0.15-0.25 mm (fine sand)  
244 (Golombek et al., 2008a, 2017).

## 245 **2.2 Density**

246 Physical properties of regoliths, such as thermal conductivity, seismic velocity, penetration resistance,  
247 shear strength, compressibility and dielectric constant, depend on bulk density, which depends on grain  
248 size distribution, grain shape, particle surface texture and grain arrangement (Carrier et al., 1973). In dust  
249 powders, repulsive effects of electrostatic forces can result in densities as low as  $1000 \text{ kg}/\text{m}^3$ ; in fine sand,  
250 inter-particle forces are mainly governed by gravity and inter-granular friction, resulting in higher  
251 densities. However, it is likely that the lower gravity on Mars could result in looser arrangements of grains  
252 of same shape and size distribution, compared to the gravity on the earth. Possible values of the regolith  
253 density can be further estimated by considering typical features of granular assemblies and sands,  
254 together with the physical properties of some terrestrial sands and regolith simulants (Mojave simulant,  
255 Eifelsand, and Mars Soil Simulant-D; Delage et al., 2017). A simple illustration providing first order  
256 estimates can be obtained from geometrical considerations of arrangements of spherical particles of the  
257 same diameter. In the densest possible arrangement (tetrahedral), with a minimum void ratio  $e_{min} = 0.351$ ,  
258 with terrestrial sands, often composed of quartz grains with a density of  $2670 \text{ kg}/\text{m}^3$ , this value  
259 corresponds to a maximum bulk density of  $1980 \text{ kg}/\text{m}^3$ , a high density for (non-basaltic) terrestrial sands.  
260 For basaltic sands, as on Mars and in some areas on the earth, the corresponding density would be  $2230$   
261  $\text{kg}/\text{m}^3$  with a grain density of  $3310 \text{ kg}/\text{m}^3$  for basalt. Conversely, the loosest possible assembly of spheres

262 (simple cubic) has a maximum void ratio  $e_{max} = 0.908$ , yielding a minimum bulk density of  $1400 \text{ kg/m}^3$  for  
263 quartz sands and of  $1580 \text{ kg/m}^3$  for basaltic sands. For non-spherical grain shapes, other configurations  
264 are possible. For example, elongated grains, with aspect ratios significantly different from one, may  
265 exhibit rotational interlocking, particles resting against each other building bridges that increase void  
266 space. Limited overburden pressure can prevent particles from rotating and form statically stable  
267 regimes, supported in the low gravity of Mars, and especially prevalent in particle packages that have not  
268 be subject to strong external loading. Once loaded or subject to vibration, these packages will tend to  
269 increase in density.

270 On the Moon, regolith density drastically increases at depths below 20 cm. This increase has been  
271 attributed to the effects of continuing small meteoroid impacts, not filtered by an atmosphere as on Mars.  
272 Small impacts generate a loose, stirred-up surface while at the same time densifying the underlying soil  
273 (Carrier et al., 1973). Details of this process are not fully understood (Heiken et al., 1991), but best  
274 estimates for typical average densities are  $1450$  to  $1550 \text{ kg m}^3$  at depths between 0 and 15 cm and  $1690$   
275 to  $1790 \text{ kg/m}^3$  at depths between 30 and 60 cm. In addition, analyses of the heat flow experiment data  
276 emplaced at the Apollo 15 and 17 sites indicates that the bulk density must be approximately  $1300 \text{ kg/m}^3$   
277 at the surface and must rise steeply in the upper few centimeters in order to be consistent with nighttime  
278 surface temperature data (Keihm et al., 1973; Keihm and Langseth, 1973, 1975; Langseth et al., 1976).  
279 The situation is, however, quite different on Mars because micrometeorites are stopped by the  
280 atmosphere. The primary shallow processes are wind transport and saltation of sand-size particles.

281 In natural sands, a non-uniform grain size distribution provides denser arrangements, with smaller  
282 grains filling voids between larger grains. Irregular angular grains allow for looser packing than spherical  
283 grains. This is expected to be the case for the InSight landing site, with surface densities estimated to be  
284 around  $1300 \text{ kg m}^{-3}$  (see below). Bolton (1986) provided the minimum ( $e_{min}$ ) and maximum ( $e_{max}$ ) void  
285 ratios and densities of a series of terrestrial sands. The loosest sands were two river sands (Welland River,  
286 Canada, and Chattahoochee River, USA) with bulk densities of  $1390$  and  $1290 \text{ kg/m}^3$ , respectively. Note  
287 that river sands are known to be rounded due to transportation in water. Sand on Mars is rounded during  
288 saltation (McGlynn et al., 2011). Both the minimum ( $1290 \text{ kg/m}^3$ ) and maximum ( $1910 \text{ kg/m}^3$ ) densities  
289 provided by Bolton (1986) are not too far from densities obtained from simple geometrical considerations  
290 on the ideal granular arrangements of spheres. In addition, observations made by previous landers and  
291 rovers also showed bulk densities in the range of  $1100$ – $1300 \text{ kg/m}^3$  and  $1150 \pm 150 \text{ kg/m}^3$  for surficial  
292 sand and sandy soil deposits (see, e.g., Golombek et al., 2008a; Herkenhoff et al., 2008, and references

293 therein). Based on the fact that surface thermal inertia values are most compatible with a sand to crusty-  
294 cloddy soil deposits (Golombek et al., 2008a) and given the above considerations on terrestrial sands, the  
295 current best estimate for the regolith surface density is close to  $1300 \text{ kg/m}^3$ . In addition, a friction angle  
296 of about  $30^\circ$  would also correspond to this density range (Delage et al., 2017).

297 In general, density is expected to increase with depth as a function of overburden pressure following  
298 an exponential relation (e.g., Robinson and Gluyas, 1992; Revil et al., 2002), but compressibility of Mars  
299 analogue material was found to be small, with an increase in density of around  $20 \text{ kg/m}^3$  from the surface  
300 to 5 m depth (Delage et al., 2017), such that this effect can generally be neglected for the depth range  
301 relevant here. Regolith particles on Mars initially originate from the comminution caused by impacts on  
302 the surface, prior to being affected by eolian transportation and saltation that result in reducing their  
303 initial angularity to produce rounded or sub-rounded sorted grains. While repeated excavation, breakup,  
304 and movement by wind would result in a rather loose packing of grains, subsequent vibrational  
305 compaction due to, e.g., seismic events may compact the soil to significant depth, as is observed on the  
306 Moon (Carrier et al., 1973, 1974; Heiken et al., 1991). In addition, saltation of grains during the soil  
307 deposition can be a high energy process and compact the soil, and relative densities in excess of 90% have  
308 been observed in accretional deposits on terrestrial sand dunes (Denekamp and Tsur-Lavie, 1981).  
309 Therefore, a model of regolith density for the InSight landing site should allow for some compaction to be  
310 present.

311 Regolith structure may locally deviate from the model proposed above in regions where craters have  
312 been filled with fine grained material due to eolian activity. This has been observed, for example, in the  
313 Gusev plains, where craters with diameters between 20 and 100 m are abundant in all stages of erosion  
314 (Golombek et al., 2006). Given a depth to diameter ratio of typically 0.2 for simple craters, filling by fine  
315 grained material could provide lens of dominantly sand-sized material in the subsurface that have not  
316 been mixed with rocks or other material by subsequent impacts.

317 To describe the lunar density data, a hyperbolic density relationship was established which reasonably  
318 reproduces densities to a depth of 3 m. However, that this description is based on no physical model.  
319 Rather, it was chosen because linearly, superlinearly, or exponentially increasing profiles yield unrealistic  
320 values at the surface or at larger depths (Heiken et al., 1991), although they also fit the available data. In  
321 its general form, density may then be written as:

$$\rho(z) = \rho_{inf} \frac{A + z}{B + z} \tag{1}$$

322 where  $\rho(z)$  is density  $\rho$  as a function of depth,  $\rho_{inf}$  is the density at depth and  $z$  is the depth below the  
 323 Martian surface in meters.  $A$  and  $B$  are constants with the dimensions of length that describe

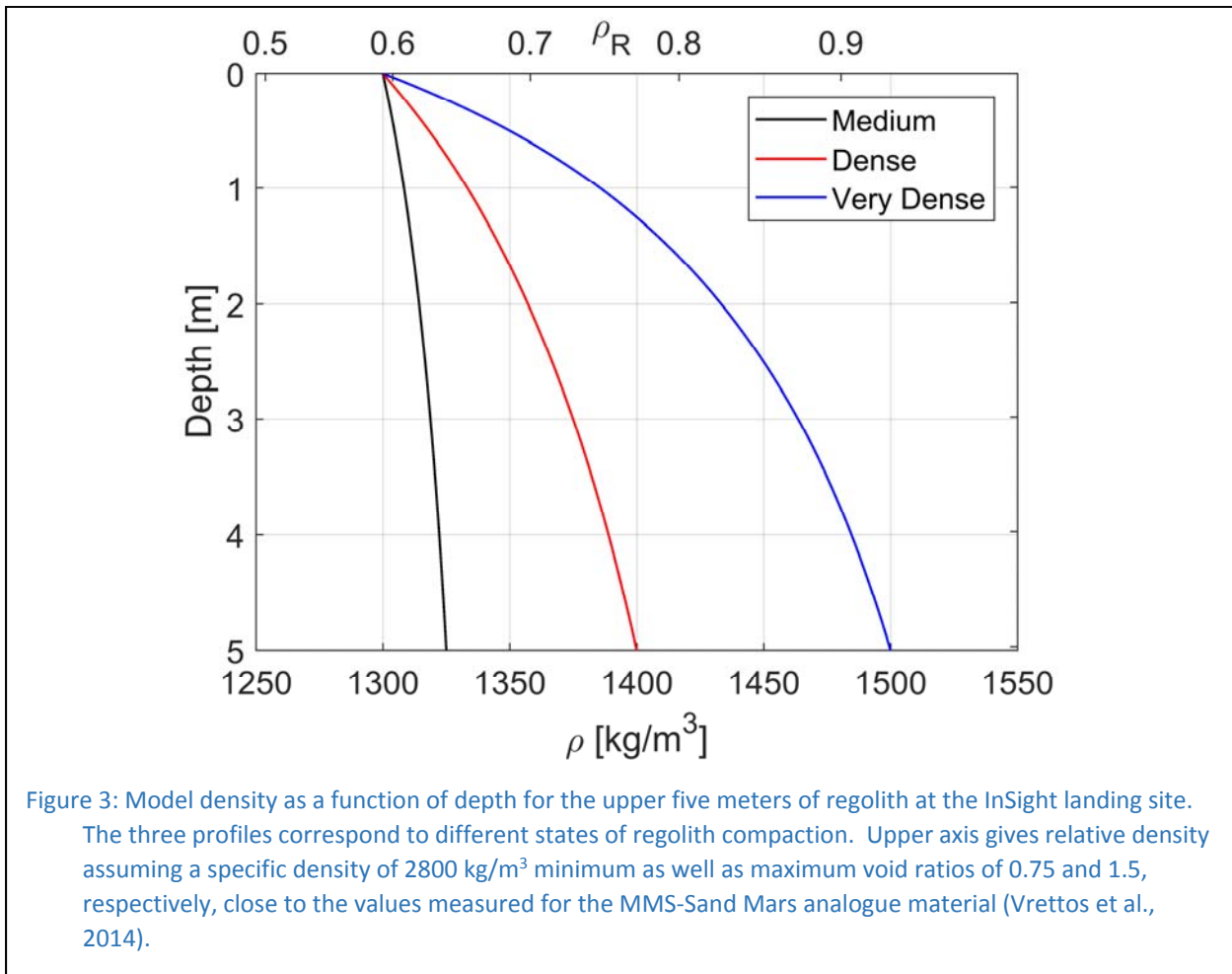
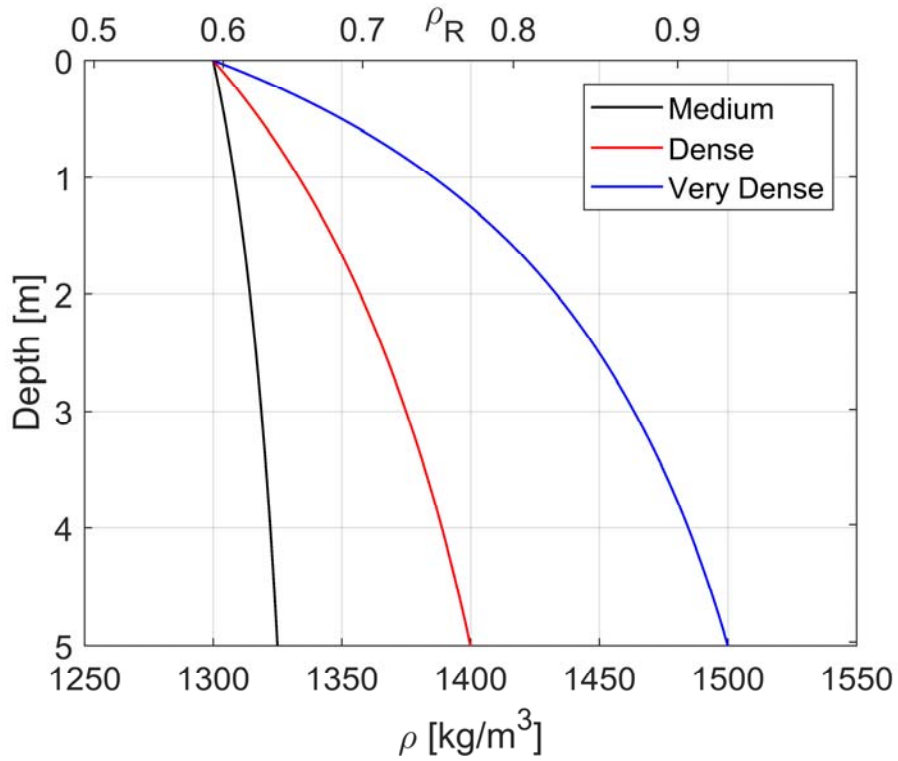


Figure 3: Model density as a function of depth for the upper five meters of regolith at the InSight landing site. The three profiles correspond to different states of regolith compaction. Upper axis gives relative density assuming a specific density of 2800  $\text{kg/m}^3$  minimum as well as maximum void ratios of 0.75 and 1.5, respectively, close to the values measured for the MMS-Sand Mars analogue material (Vrettos et al., 2014).

324

the chosen density profile, and example coefficients corresponding to the cases shown in Figure



325

326 Figure 3 are given in Table 1. As a reference, a surface density of 1300 kg/m<sup>3</sup> seems to be most compatible  
327 with the available constraints, and three different compaction models are shown. If void ratios between  
328  $e_{min} = 0.75$  and  $e_{max} = 1.5$  are assumed in accordance with measurements on Mars regolith analogue  
329 material (Vrettos et al., 2014), relative densities between 0.6 (moderately compacted) and >0.9 (densely  
330 compacted) are obtained at 5 m depth.

331

Table 1: Parameters used to calculate density profiles for the different cases shown in Figure 3.

Case	$\rho_{max}$ (kg/m <sup>3</sup> )	A (m)	B (m)
Medium Compacted	1350	4.81	5
Densely Compacted	1500	4.33	5
Very Densely Compacted	1600	2.03	2.5

332

### 333 2.3 Cohesion

334 Cohesion, a component of the shear strength, of surface materials on Mars has been determined from  
 335 soil mechanics experiments performed by arms and scoops on fixed landers and by the interaction of  
 336 wheels of rovers with surface materials by rovers. The two Viking landers and the Phoenix lander had  
 337 arms that trenched surface materials while monitoring motor currents to yield force, and imaging systems  
 338 to observe the deformed materials (Moore et al., 1977, 1987; Shaw et al., 2009). The Mars Pathfinder  
 339 rover, Sojourner, the two Mars Exploration Rovers, Spirit and Opportunity, and the Mars Science  
 340 Laboratory rover, Curiosity, performed wheel trenching and terramechanics experiments, while  
 341 monitoring motor currents to derive wheel torques, and imaged the deformed materials (Moore et al.,  
 342 1999; Herkenhoff et al., 2008; Sullivan et al., 2011; Arvidson et al., 2014). These experiments determined  
 343 basic soil mechanics measurements of cohesion and angle of internal friction. Imaging and  
 344 thermophysical properties and other relations were used to measure or constrain the particle size of the  
 345 soils and the bulk density (e.g., Moore and Jakosky, 1989; Christensen and Moore, 1992; Herkenhoff et  
 346 al., 2008; Golombek et al., 2008a).

347 Results of these experiments revealed four probable different soil deposits on Mars based on their  
 348 mechanical properties and likely means of formation (e.g., Golombek et al., 2008a). Two types of deposits  
 349 that appear to have been deposited by the wind were found at the landing sites. 1) Bedforms are  
 350 composed of sand size particles that were sorted by the wind and include sand dunes and ripples. They  
 351 are either well sorted by size or poorly sorted and typically cohesionless. Some of the ripples have a  
 352 slightly cohesive near surface layer (few kPa) a few centimeters thick (Sullivan et al., 2011). 2) Drift  
 353 deposits appear to be very fine grained dust (<10  $\mu$ m) that has settled out of the atmosphere (Christensen  
 354 and Moore, 1992; Moore et al., 1999; Paton et al., 2016). This material is also effectively cohesionless  
 355 (and not load bearing). More cohesive soils have also been found. These soils have a cohesive surface

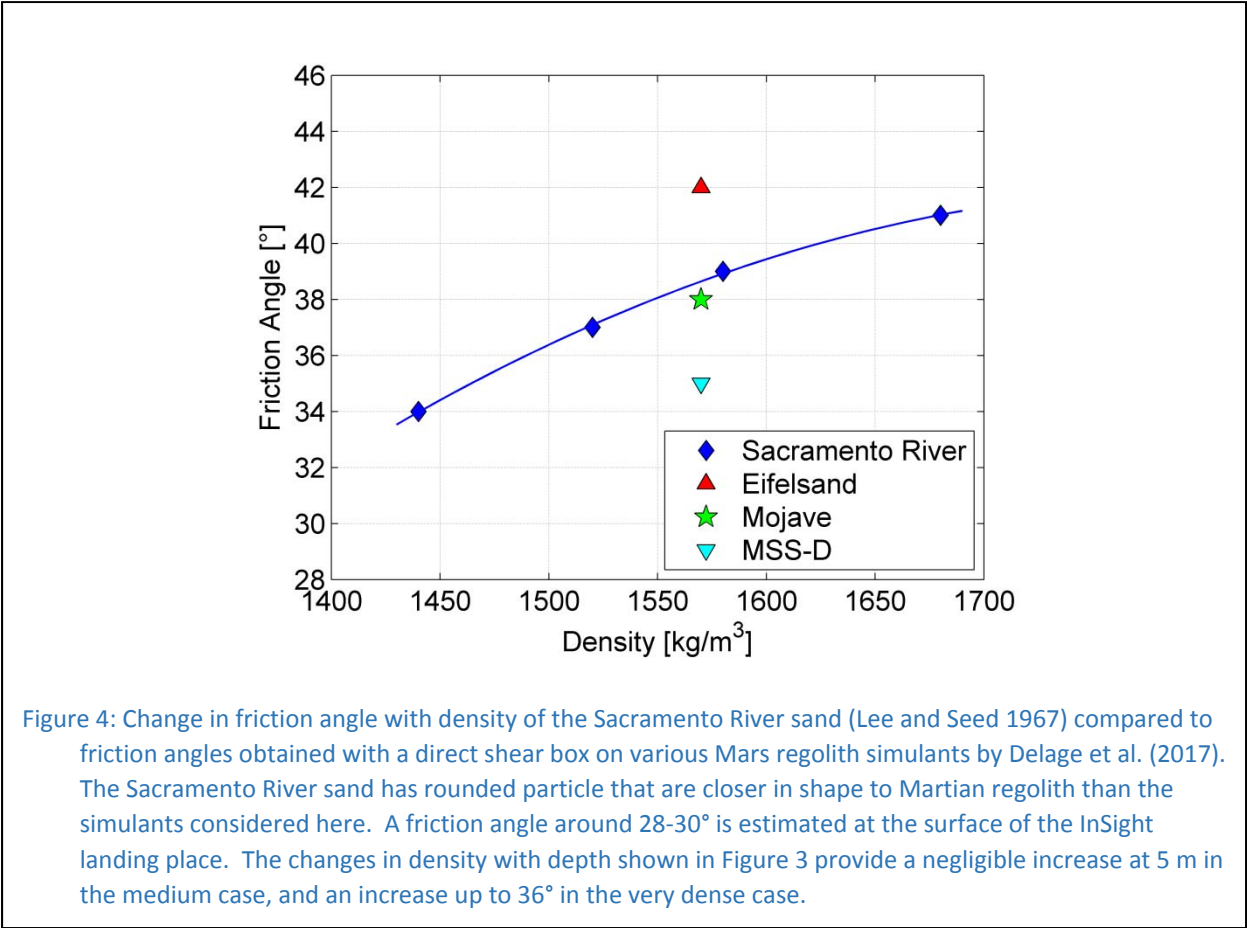
356 crust and/or break up into clods or blocks when deformed. Crusty and cloddy soils have cohesions of less  
357 than 4 kPa and blocky soils have higher cohesions of 3-11 kPa (Moore et al., 1987; Herkenhoff et al., 2008).  
358 Both are composed of dominantly sand size grains with some pebbles. The cohesive soils in most cases  
359 are limited to surface layers of the order of centimeters thick and likely formed by precipitation of salts  
360 from thin films of water interacting with the atmosphere (Haskin et al., 2005; Tosca et al., 2004; Hurowitz  
361 et al., 2006; Martin-Torres et al., 2015).

## 362 **2.4 Internal Friction Angle**

363 The internal friction angle of sands depends on their grain size distribution, grain shape, particle  
364 surface texture, grain arrangement and bulk density. Friction angles are determined by shearing  
365 specimens under constant confining stress, by using either a direct shear box or a triaxial apparatus.  
366 Shearing mobilizes irreversible volume changes. Loose sands decrease in volume due to the entanglement  
367 of grains during shear; dense sands increase in volume due to disentanglement, providing larger  
368 resistance to shear and higher friction angles. At the same density, angular particles provide higher  
369 friction angles than rounded particles. As discussed above, the surficial Martian regolith at the InSight  
370 landing site is expected to be composed of rounded particles in the range ~150-250  $\mu\text{m}$  (fine sand)  
371 (Golombek et al., 2008a, 2017). In this regard, shear tests carried out on lunar regoliths (Scott, 1987) or  
372 lunar regolith simulants (JSC-1 simulant or other crushed basalts, e.g., McKay et al., 1994; Alshibli and  
373 Hasan, 2009; Vrettos, 2012) are not relevant, given the highly angular shape of their grains. As shown in  
374 Delage et al. (2017), various Mars regolith simulants, that have been apparently selected based on  
375 mineralogical considerations, are also somewhat angular. The Mojave Mars Simulant provided by JPL  
376 (MMS, Peters et al., 2008) is crushed Miocene basalt, the Mars Soil Simulant-Dust provided by DLR (MSS-  
377 D; Becker and Vrettos, 2016) is a 50/50 mix of crushed olivine and quartz sand (with a bimodal grain size  
378 distribution curve and olivine particles finer than what is expected at the InSight landing site). The  
379 Eifelsand simulant of DLR is a mix of crushed basalt and volcanic pumice sand (Delage et al., 2017). In this  
380 respect, simulants based on quartz sands (e.g., WF34; Lichtenheldt, 2016) may be mechanically more  
381 representative for what is expected to be present at the InSight landing site, as quartz sands show mainly  
382 rounded to sub-angular grains.

383 Lee and Seed (1967) considered changes in friction angle with density in a terrestrial Sacramento River  
384 (USA) sand, which is composed of rounded grains. These changes are compared in Figure 4 with the  
385 friction angles of a Mojave simulant (a mix of MMS, containing alluvial sedimentary and igneous grains

386 from the Mojave Desert and basaltic pumice), MSS-D, and Eifelsand, determined with a direct shear box  
 387 at a bulk density of 1570 kg/m<sup>3</sup> by Delage et al. (2017). The figure demonstrates the decrease in friction  
 388 angle at lower density with a good correspondence between the Sacramento River sand and the Mojave  
 389 simulant (angle of 38°, compared to 35° for MSS-D and 42° for Eifelsand, probably due to the very angular  
 390 and irregular shape of pumice particles). Extrapolation at bulk density of 1300 kg/m<sup>3</sup> provides a friction  
 391 angle between 28 and 30° for the surficial layer at the InSight landing site.



392 The changes in friction angle with depth can be estimated based on the changes in density shown in  
 393 Figure 3, assuming a density dependence of the friction angle  $\phi$  corresponding to that of the Sacramento  
 394 River sand. A second order fit to the data results in

$$\phi = A\rho^2 + B\rho - C \tag{2}$$

395 where  $\rho$  is given in units of kg/m<sup>3</sup>.  $A$ ,  $B$ , and  $C$  are constants with values of  $-5.9772 \times 10^{-5} \text{m}^6/\text{kg}^2$ ,  
 396  $0.21583 \text{m}^3/\text{kg}$ , and  $152.88^\circ$ , respectively. In the medium compacted case (Figure 3), the increase at 5 m  
 397 is negligible, whereas the friction angle increases up to 36° in the very dense case. As commented above,

398 the increase in density and friction angle also involves the mobilization of dilating behavior of the sand,  
399 which could have some consequence on the penetrability of the mole. Dilation mobilized during  
400 penetration at the sand/mole interface results in an increase in radial stress that makes the penetration  
401 less efficient, as a greater portion of the stroke energy is needed to mobilize the soil.

## 402 **2.5. Grain size Distribution**

403 We base our estimation of the average grain size distribution (GSD) within the InSight landing ellipse  
404 using a combination of observations and modeling. We have previously used this approach to extrapolate  
405 to the larger 10 cm particle size and hence determine the probability of obstruction of the HP<sup>3</sup> mole by a  
406 rock (Golombek et al., 2017). Here we extend the extrapolation down to the smaller 600  $\mu\text{m}$ , an upper  
407 limit of the particles that may be present through eolian processes. The model parameters are derived  
408 for the fragmentation that has produced the observable rocks through meteorite impact, and therefore  
409 extrapolation into a size regime potentially dominated by eolian processes has limited justification.

410 Our previous study applied the negative binomial (NB) fragmentation model (Charalambous,  
411 2014/2015) to the rocks of the compiled HiRISE images from the InSight landing ellipse (Golombek et al.,  
412 2017). We validated this approach by matching rock distributions from HiRISE images of Viking 2, Mars  
413 Pathfinder, Spirit, and Phoenix to subsequent ground truth imaging. We predicted that the surface  
414 population down to 10 cm is likely to be similar to that observed at Columbia Memorial Station (CMS)  
415 (Golombek et al., 2017). The NB model is readily able to extrapolate the particle size distribution of a  
416 surface population used to validate the model down to 5 cm in the case of Spirit and Phoenix.

417 In estimating a cumulative mass fraction of the regolith, it is necessary to match both the surface rocks'  
418 size distribution, and the rock coverage expressed as a cumulative fractional area (CFA). To match both  
419 in general requires an adjustment, in this case an addition, of material below the observable rock size.  
420 The physical basis for such an addition is deposition of eolian material and subsequent mixing by  
421 meteorite impact. This dilution of the fragmentation products by eolian material provides the observed  
422 CFA. The eolian material can only be introduced for particle sizes below the saltation limit which we take  
423 at the upper limit of 600  $\mu\text{m}$ . (Kok et al., 2012). Figure 5 shows the predicted grain size distribution (GSD)  
424 based on these considerations down to the saltating upper size bound which, for the case of the InSight  
425 landing site ellipse (E9), predicts the GSD  $\sim 75\%$  by mass below 600  $\mu\text{m}$ .

426 We can state that the GSD at the InSight landing site is likely to be close to the GSDs of the CMS and  
427 Phoenix landing sites, even though eolian processes might dominate at the InSight landing site. The  
428 thermal inertia in InSight landing ellipse has a value of about  $200 \text{ J}/(\text{m}^2 \text{ K s}^{1/2})$ , similar to that of CMS and  
429 Phoenix landing site. As the thermal inertia is dominated by particles of  $100 \mu\text{m}$  or below in size, this  
430 suggests a common eolian component. On this basis, the predicted grain size distribution for the InSight  
431 landing site is expected to make a transition below  $600 \mu\text{m}$  to match the observed GSD of the sand  
432 determined by the Phoenix microscope station (Pike et al., 2011).

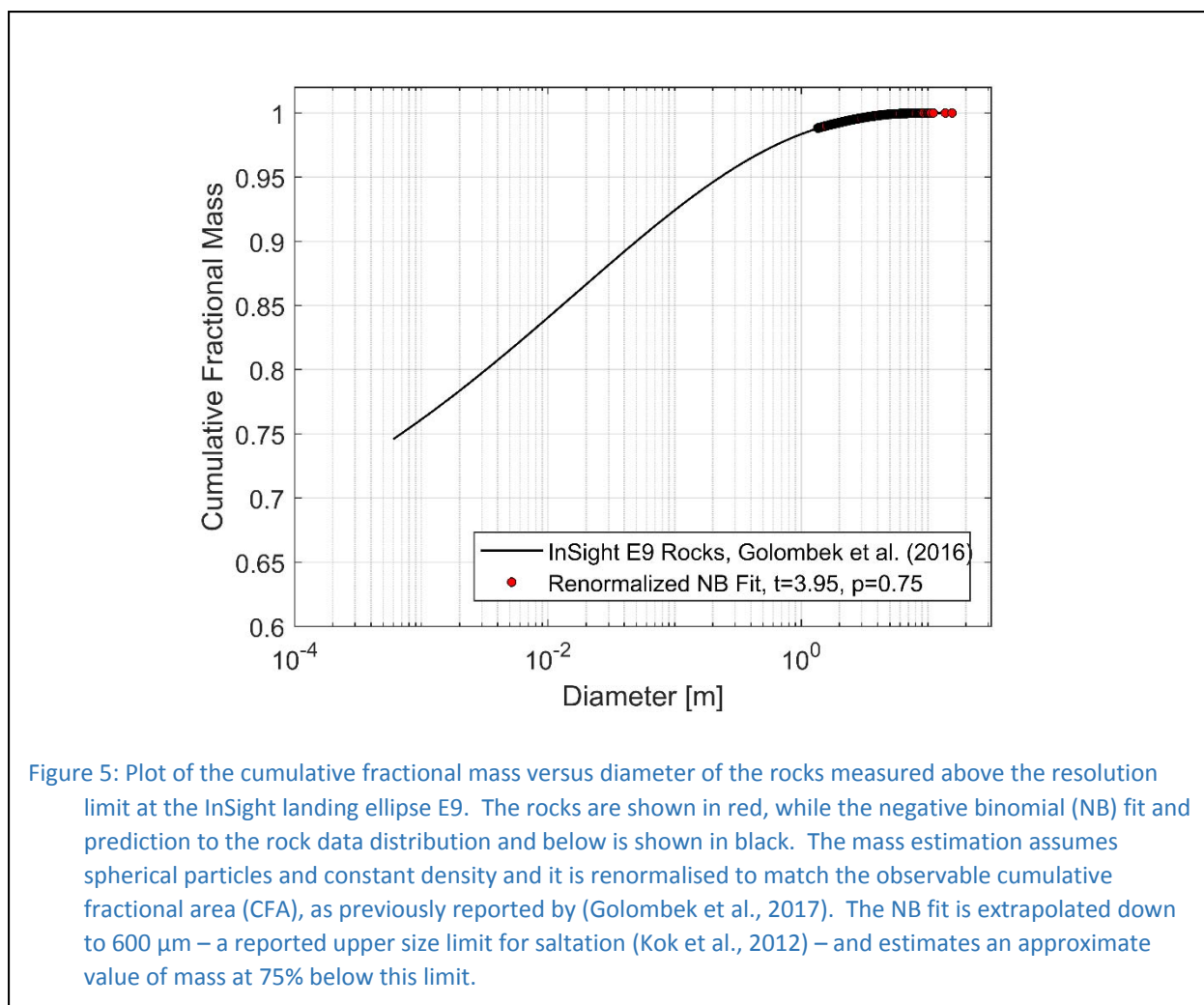


Figure 5: Plot of the cumulative fractional mass versus diameter of the rocks measured above the resolution limit at the InSight landing ellipse E9. The rocks are shown in red, while the negative binomial (NB) fit and prediction to the rock data distribution and below is shown in black. The mass estimation assumes spherical particles and constant density and it is renormalised to match the observable cumulative fractional area (CFA), as previously reported by (Golombek et al., 2017). The NB fit is extrapolated down to  $600 \mu\text{m}$  – a reported upper size limit for saltation (Kok et al., 2012) – and estimates an approximate value of mass at 75% below this limit.

433

434

### 435 3. Regolith Thermophysical Properties

436 This section compiles regolith material parameters needed to calculate subsurface temperatures at  
 437 the InSight landing site. The energy balance of the shallow subsurface is governed by insolation, regolith  
 438 thermal inertia, and heat diffusion into the deeper subsurface. The one dimensional heat diffusion  
 439 equation can be written as:

$$\rho(z)c_p(T)\frac{\partial T}{\partial t} = \frac{\partial}{\partial z}k(z,P,\rho,T,\sigma)\frac{\partial T}{\partial z} \quad (3)$$

440 where  $\rho$  is density,  $c_p$  is specific heat,  $T$  is temperature,  $z$  is depth,  $P$  is CO<sub>2</sub> gas pressure,  $t$  is time,  $\sigma$  is  
 441 ambient (overburden) pressure, the pressure exerted by the gravitational attraction of the mass of the  
 442 column of regolith above the depth of interest, and  $k$  is thermal conductivity. Equation (3) is a second  
 443 order differential equation, which can be solved by prescribing two boundary conditions: One is usually  
 444 given by constant (or zero) heat flux at a depth, while the other is usually given in terms of the surface  
 445 energy balance. For periodic insolation forcing, the surface energy balance takes the convenient form

$$\sigma_B \varepsilon T^4 = (1 - A)S + \varepsilon R + I \sqrt{\frac{\pi}{p}} \left. \frac{\partial T}{\partial z'} \right|_{z'=0} \quad (4)$$

446 where  $\sigma_B$  is the Stefan-Boltzmann constant,  $\varepsilon$  is surface emissivity,  $A$  is albedo,  $S$  is total solar radiative  
 447 flux including scattered radiation,  $R$  is the thermal radiative flux from the atmosphere towards the  
 448 surface,  $p$  is the period of the forcing, and  $z' = z/d_e$  is depth normalized to the thermal skin depth  $d_e =$   
 449  $\sqrt{kp/\rho c_p \pi}$ . In Equation (4), all material parameters have been absorbed in the thermal inertia  $I$ , which is  
 450 defined as

$$I = \sqrt{k\rho c_p} \quad (5)$$

451 Equation (5) is only valid when thermal conductivity is constant, which is not the case (see below).  
 452 However, constant thermal inertia is a convenient way to describe the response of surface temperatures  
 453 to insolation changes, and it is thus a widely used approximation. However, care must be taken when  
 454 converting thermal inertia to material parameters like thermal conductivity, since different combinations  
 455 of material parameters govern the temperature at the surface (thermal inertia) and in the subsurface

456 (thermal diffusivity, see below). The expected values of material parameters and their dependencies will  
457 be discussed for the InSight landing site below.

### 458 **3.1. Surface Emissivity**

459 Emissivity  $\varepsilon$  is defined as the ratio of emitted specific radiance  $I_r$  ( $\text{W}/(\mu\text{m m}^2 \text{ sr})$ ) to the black-body  
460 radiance  $B$  of a surface at temperature  $T$ . Emissivity is a function of the wavelength  $\lambda$  and viewing angle,  
461 but the angle dependence is commonly assumed to be negligible and the radiative heat flux density  $q_{rad}$   
462 ( $\text{W}/\text{m}^2$ ) of thermal emission can be represented via hemispherical integration as

$$q_{rad} = \pi \int_0^{\infty} \varepsilon(\lambda) B(T, \lambda) d\lambda \quad (6)$$

463 Often,  $\varepsilon$  is assumed to be a constant, i.e.,  $\varepsilon = \varepsilon_q$ , where  $\varepsilon_q$  is the weighted spectral average emissivity.  
464 Equation 6 can then be reduced to a form similar to the Stefan-Boltzmann Law:

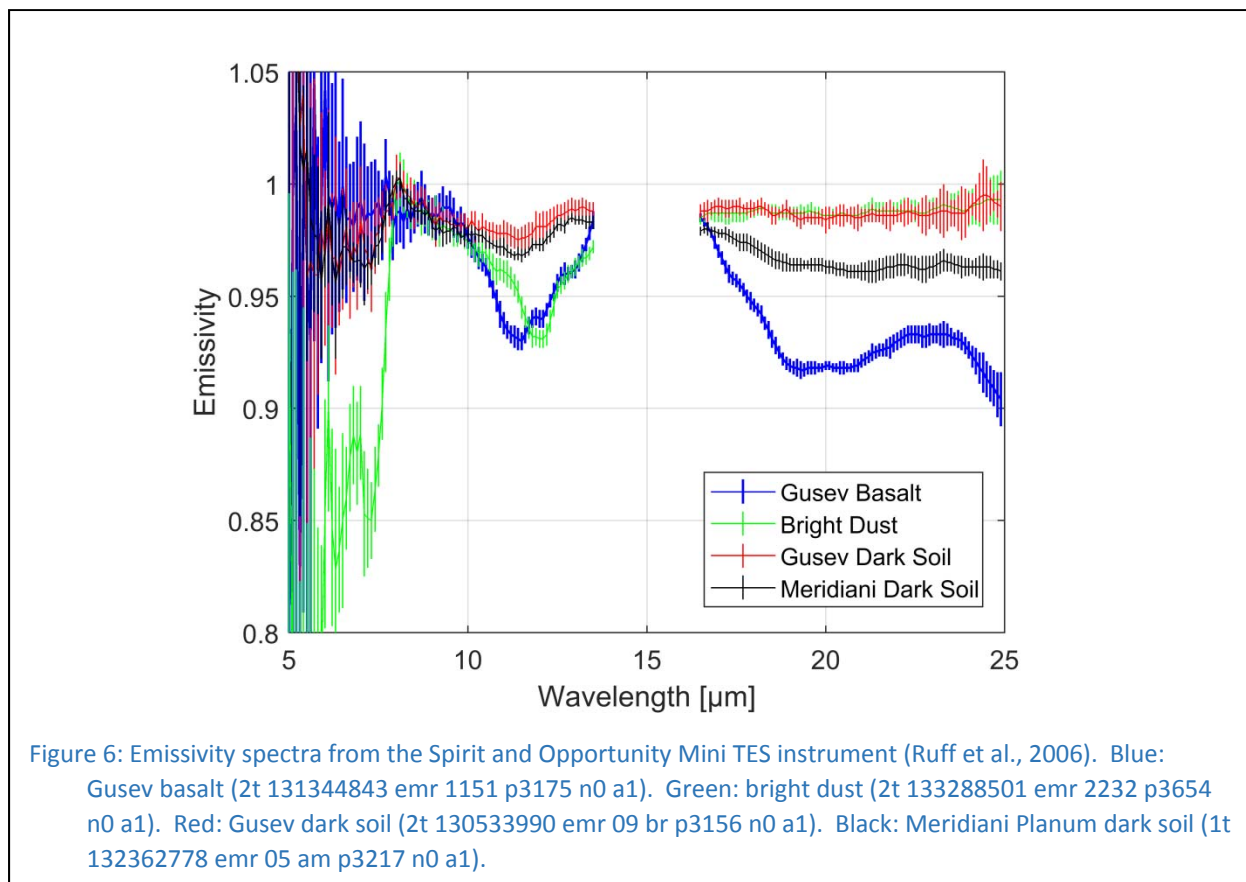
$$q_{rad} = \varepsilon_q \sigma_B T^4. \quad (7)$$

465 where  $\sigma_B$  is the Stefan-Boltzmann constant. This approximation is usually sufficient for thermal models  
466 but has a systematic error as a function of  $T$  if  $\varepsilon$  varies with wavelength.

467 Instruments for Mars surface thermal emission observations include the Thermal Emission  
468 Spectrometer (TES) on Mars Global Surveyor (Christensen et al., 2001), the Thermal Emission Imaging  
469 System (THEMIS) on Mars Odyssey (Christensen et al., 2003a), the Mini-Thermal Emission Spectrometer  
470 (Mini-TES) on the Mars Exploration Rovers (Christensen et al., 2004a, b), the Planetary Fourier  
471 Spectrometer (PFS) on Mars Express (Formisano et al., 2005) and the Ground Temperature Sensor of the  
472 Rover Environmental Monitoring Station (REMS – GTS) on the Mars Science laboratory (Gomez-Elvira et  
473 al., 2012). It should be noted that interpretation of thermal emission is ambiguous because two  
474 unknowns, i.e., surface temperature and emissivity, contribute to the radiance, while only a single  
475 quantity is measured. Therefore, observations aim at measuring radiance close to the Christiansen  
476 wavelength, the wavelength at which the real part of silicate particle refractive index matches that of the  
477 atmosphere, and emissivity is close to unity (Conel, 1969).

478 Assuming soil physical and compositional properties similar to those observed at the two Mars  
479 Exploration Rovers landing sites (Golombek et al., 2005, 2008a; Yen et al., 2005), the InSight site is  
480 expected to be covered by basaltic sand, possibly covered in places with a fine, higher albedo dust. We

481 use Mini-TES spectra analyzed by Ruff et al. (2006) as a basis for emissivity estimates. These spectra are  
 482 shown in Figure 6. They correspond to a bright dust drift (green), a basalt rock cleaned of dust by the  
 483 Rock Abrasion Tool (blue), and to the darker sand exposed at surfaces disturbed by the rovers at Gusev  
 484 crater (red) and Meridiani Planum (black). Data affected by the set of strong CO<sub>2</sub> absorption lines near 15  
 485 μm wavelength have been removed.



486 The constant emissivity  $\epsilon_q$  that best represents the heat flux from the surface is a function of  
 487 composition and surface temperature, because the peak of the blackbody emission changes significantly  
 488 within the range of expected temperatures. For the dark soil, the expected value for  $\epsilon_q$  is in the range of  
 489 0.97 to 0.985, with less than 0.5 % change with temperature. The bright dust and basalt have a similar  $\epsilon_q$   
 490 of 0.96 at 285 K, which increase by 2 % and decrease by 1.5 % towards 185 K, respectively. Therefore,  
 491 based on remote sensing and in-situ data, a constant emissivity value of 0.98 (+1% /-2%) is suitable for  
 492 both thermal modeling and surface temperature derivation at the InSight landing site, and the stated  
 493 uncertainty is equivalent to a deviation in derived thermal inertia of <20 J/(m<sup>2</sup> K s<sup>1/2</sup>) in the model of  
 494 Vasavada et al. (2017). Examples of weighted average thermal emissivities for the HP<sup>3</sup> radiometer filters  
 495 are given in Table 2.

Table 2: Weighted average emissivity for three wavelength bands corresponding to the HP<sup>3</sup> radiometer filters at 235 K for four different soils measured in-situ by the Mars Exploration Rover’s Mini TES instrument.

	8 – 14 $\mu m$	8 – 9.5 $\mu m$	16 – 19 $\mu m$
Gusev dark soil	0.98	0.99	0.99
Meridiani dark soil	0.98	0.98	0.97
Bright dust	0.97	0.99	0.99
Gusev Basalt (Humphrey)	0.96	0.99	0.96

496

### 497 3.2. Surface Thermal Inertia

498 Thermal inertia describes the resistance to a change in temperature of the upper 2–30 cm of the  
 499 surface. Fine particles change temperature quickly and therefore have low thermal inertia; higher thermal  
 500 inertia surfaces are composed of sand, duricrust, rock fragments, or a combination of these materials.  
 501 Bulk orbital thermal inertia observations of Mars include values derived from: (1) Viking Infrared Thermal  
 502 Mapper (IRTM) data at ~60 km per pixel (Kieffer et al., 1977; Palluconi and Kieffer, 1981), (2) Mars Global  
 503 Surveyor TES data (Christensen et al., 1992) at 8 pixels per degree (Mellon et al., 2000; Christensen et al.,  
 504 2001) and at 20 pixels per degree (Putzig et al., 2005; Putzig and Mellon, 2007), and (3) Mars Odyssey  
 505 THEMIS data at ~100 m/pixel (Christensen et al., 2004c; Fergason et al., 2006a; Fergason et al., 2012).  
 506 Surface thermal inertia measurements were also obtained by the Miniature Thermal Emission  
 507 Spectrometer (Mini-TES) on the Spirit and Opportunity rovers during their traverses (Christensen et al.,  
 508 2003b; Fergason et al., 2006b). In addition, Curiosity determined thermal inertia from Ground  
 509 Temperature Sensor (GTS) measurements from the Rover Environmental Monitoring Station (REMS)  
 510 instruments (Hamilton et al., 2014, Vasavada et al., 2017).

511 Bulk thermal conductivity ranges over 3 orders of magnitudes on Mars as a function of the physical  
 512 state of the (sub-)surface (compared to small factors for  $\rho$  and  $c_p$  as a function of the porosity,  
 513 temperature, composition, etc., compare Equation (5)).  $I$  is virtually independent of the product  $\rho c_p$ ,  
 514 whose value is generally close to  $\sim 10^6$  J/(m<sup>3</sup> K) (Neugebauer et al., 1969; Fergason et al., 2006a), and is  
 515 mainly controlled by  $k$ . More precisely,

$$k \approx \frac{I^2}{8 \cdot 10^5} \quad \text{W/(m K)} \quad (8)$$

516 for temperatures and surface densities at the InSight landing site. On Mars, thermal inertia values have  
 517 largely been derived from remote measurements. Because of the strong dependence of its value on grain  
 518 size and degree of cementation, Putzig (2006) distinguished between dust (28-135 J/(m<sup>2</sup> K s<sup>½</sup>)), sand (135-  
 519 630 J/(m<sup>2</sup> K s<sup>½</sup>)) and duricrust (252-513 J/(m<sup>2</sup> K s<sup>½</sup>)). Paton et al. (2016) gave a value for *I* of 81 to 125 J/(m<sup>2</sup>  
 520 K s<sup>½</sup>) for dust around the Viking 1 footpads from direct measurements.

521 The highest resolution TES nighttime thermal inertia determination of the InSight landing site (Putzig  
 522 and Mellon (2007) at 20 pixels per degree range from 138 to 284 J/(m<sup>2</sup> K s<sup>½</sup>) and average 218 J/(m<sup>2</sup> K s<sup>½</sup>)  
 523 (n=314). A regional thermal inertia map (100 m spatial scale) was generated for the landing site  
 524 (Golombek et al., 2017) from predawn temperature data acquired by THEMIS band 9 (12.57 μm)  
 525 (Christensen et al., 2004c) between Mars Year 30 and 32 during low-dust seasons to minimize the  
 526 atmospheric impact on the derived values. The resulting thermal inertia map displays values ranging from  
 527 ~70 J/(m<sup>2</sup> K s<sup>½</sup>) to 390 J/(m<sup>2</sup> K s<sup>½</sup>), but 99% of the area has a thermal inertia of 130 to 220 J/(m<sup>2</sup> K s<sup>½</sup>).  
 528 Within the landing ellipse, the range is even smaller, demonstrating high thermophysical homogeneity at  
 529 the 100 m scale over the entire landing region. The median regional thermal inertia is ~180 J/(m<sup>2</sup> K s<sup>½</sup>),  
 530 corresponding to cohesionless ~170 μm material (fine sand) based on laboratory work and theoretical  
 531 relationships (Presley and Christensen, 1997a; Piqueux and Christensen, 2011). Higher thermal inertia  
 532 values are expected to be associated with medium to coarse sand, and will likely include mixtures of grain  
 533 sizes, including larger clasts such as those surfaces observed at Gusev crater (Golombek et al., 2005,  
 534 2008a; Ferguson et al., 2006b). The corresponding diurnal skin depth values (i.e., depth at which  
 535 maximum amplitude is attenuated to 37% of its surface amplitude) is a maximum of ≤6 cm, indicating that  
 536 the upper few cm of the surface layer are characterized by these thermal inertia values. The lack of  
 537 seasonal variations in thermal inertia indicates that the same thermal inertia and materials extend a few  
 538 tens of cm below the surface (Golombek et al., 2017).

539 The lowest thermal inertia values in the landing region (e.g., ~70 J/(m<sup>2</sup> K s<sup>½</sup>)) are rare, and typically are  
 540 observed within depressions probably that trap atmospheric dust and very fine sand, or on the lee side of  
 541 positive topographic features (Golombek et al., 2017). These low inertia values could result from fine  
 542 sand (100–200 μm) with a very thin coating (<1–2 mm) of dust (several μm diameter particles). The  
 543 highest thermal inertia values (i.e., 350–390 J/(m<sup>2</sup> K s<sup>½</sup>)) are also uncommon, associated with crater rims  
 544 and ejecta blankets, as expected for rocky ejecta craters, but not bedrock at the 100 m spatial scale.

545 Regolith induration is not inconsistent with the derived thermal inertia values, however thermal modeling  
546 of cemented regolith shows that the volume of the cementing phase would need to be minimal (e.g.,  
547 typically <0.1% in volume) with little impact on the mechanical properties (Piqueux and Christensen,  
548 2009a). Comparison of the cohesion of surface soils at other landing sites with their thermal inertia would  
549 limit the cohesion to less than a few of kPa, consistent with very weakly bonded soils on Earth (Golombek  
550 et al., 1997, 2008a).

### 551 **3.3. Surface Albedo**

552 The albedo, or surface reflectivity or brightness of reflected solar energy from the surface in which the  
553 viewing geometry has been taken into account, has been measured globally by both IRTM and TES at 1  
554 pixel and 8 pixels per degree, respectively (e.g., Pleskot and Miner, 1981; Christensen et al., 2001). The  
555 albedo can, for example, be used to infer the dustiness of the surface, as very dusty areas exhibit very  
556 high albedo (and, in addition, very low-thermal inertia) (Christensen and Moore, 1992; Moore and  
557 Jakosky, 1989; Mellon et al., 2008; Putzig et al., 2005; Golombek et al., 2008a). The amount of dust cover  
558 at the landing sites was also evaluated using the TES dust cover index (16 pixels per degree), which  
559 includes a more explicit measure of the particle size and the amount of dust coating the surface (Ruff and  
560 Christensen, 2002).

561 The albedo of the InSight landing site is about 0.25 from IRTM (Pleskot and Miner, 1981) and 0.24 from  
562 TES (Christensen et al., 2001). This relatively high albedo is consistent with atmospherically deposited  
563 dust, which is consistent with its relatively high dust cover index (Ruff and Christensen, 2002). However,  
564 thermal inertia values are nowhere dominated by very fine material at the 100 m scale suggesting that  
565 dust may form an optically thick but thermally thin coating (hundreds of  $\mu\text{m}$ ) on most surface materials  
566 in this region of Mars. This interpretation is supported by the similarity of the dust cover index in the  
567 InSight landing site region (0.94) with the Viking Lander 2 site and dusty locations of the Gusev cratered  
568 plains explored by Spirit (e.g., Golombek et al., 2005, 2006), both of which had very thin dust coatings.

569 All previous landers on Mars have modified the surface during landing (e.g., Moore et al., 1987;  
570 Golombek et al., 1999; Squyres et al., 2004; Soderblom et al., 2004; Smith et al., 2009; Arvidson et al.,  
571 2014; Daubar and McEwan, 2015). The InSight lander will use pulsed retropropulsive thrusters to slow  
572 itself during landing. The thrusters on InSight are the same as those used by the Phoenix lander, which  
573 dispersed 5-18 cm of soil exposing water ice when landing (Mehta et al., 2011). Modeling of this process  
574 showed that pulsed thrusters lead to explosive erosion via cyclic shock waves that fluidize soils, producing

575 ten times greater erosion than conventional jets (Mehta et al., 2011, 2013). Consideration of these effects  
576 for InSight landing indicates that generally circular depressions will form at the jet impingement locations,  
577 but they will not be large enough to appreciably alter the surface topography at the lander footpad  
578 locations and thus won't pose a risk to landing safely (Golombek et al., 2017). Nevertheless, surface soils  
579 will be dispersed away from the lander with sand and pebbles being eroded from the jet impingement  
580 locations and deposited away from the spacecraft.

581 The thin coating of fine-grained dust present at the landing site will be dispersed into the atmosphere  
582 at the time of landing, reducing the albedo of the surface around the lander. This has been observed to  
583 occur around previous landers, and in the cases of Phoenix and Mars Science Laboratory (Curiosity) the  
584 effect can be measured using relative albedo measurements in HiRISE images (Daubar and McEwan,  
585 2015). The quantity of albedo change and rate of subsequent brightening varied depending on the  
586 particular piece of hardware; for the MSL descent stage, the albedo was initially lowered by ~50%. After  
587 the initial darkening, images show a rapid initial brightening that slowed over time, following a logarithmic  
588 function. The majority of the blast zone faded to ~90% of the initial albedo by ~500 days after landing,  
589 but the darkest areas have not faded completely. Although it is located at high latitudes, the Phoenix  
590 landing site is in some ways a better analogy for InSight due to the same landing thrusters; however,  
591 monitoring of the Phoenix site is complicated by seasonal activity and limitations to orbital observations.  
592 The Phoenix landing reduced the surroundings to ~60-80% of the pre-landing albedo. Before subsequent  
593 orbital images could be taken in the same season, the blast zone disappeared, presumably due to seasonal  
594 frosts redistributing surface dust.

595 Based on these observations and the relatively dusty nature of western Elysium Planitia, we would  
596 expect similar changes to the InSight landing site, where the surface albedo can be expected to be reduced  
597 by ~20-50% upon landing, then exhibit a rapid initial brightening, and then gradually return to the  
598 surrounding albedo over the next several Mars years. The reduction in albedo will warm the surface and  
599 the deposition of sand and pebbles from the thrusters could also have a thermal effect.

### 600 **3.4. Thermal Conductivity**

601 This section describes recommended values for the thermal conductivity  $k$  of the regolith expected at  
602 the InSight landing site, based on orbital data and published laboratory/theoretical work. Unless  
603 otherwise specified, the regolith is treated as an idealized discontinuous medium composed of spherical  
604 basaltic grains in stagnant CO<sub>2</sub> gas. The relationship between bulk regolith conductivity and various

605 controlling factors (i.e., pressure, temperature, grain size, porosity, etc.) is quantitatively described in the  
606 literature for a wide range of planetary configurations of atmospheric pressures, compositions, regolith  
607 properties, etc. For the specific case of the InSight landing region, these relationships have been tailored  
608 to the expected subsurface properties for simplicity, and are presented here. We will first discuss an  
609 appropriate choice for the simple case of constant thermal conductivity and then present the more  
610 general case of temperature and depth dependency.

611 Thermophysical properties of the landing region have been characterized from orbital data acquired  
612 by the Thermal Emission Imaging System (THEMIS) (Christensen et al., 2004c). In the landing ellipse,  
613 thermal inertia  $I$  values derived from temperature measurements typically range from 130 to 220 J/(m<sup>2</sup> K  
614 s<sup>1/2</sup>) with a median value of ~180 J/(m<sup>2</sup> K s<sup>1/2</sup>) (Golombek et al., 2017). Using relationships established in  
615 the laboratory (Preseley and Christensen, 1997b) the expected regolith thermal conductivity is  $0.017 < k <$   
616  $0.048$  W/(m K) with median value of 0.032 W/(m K) corresponding to ~150-170  $\mu$ m unconsolidated grains  
617 (Golombek et al., 2017).

618 Published thermophysical studies of Martian subsurface temperatures generally use fixed  $I$  or  $k$  (as  
619 opposed to temperature or pressure-dependent values), because these dependencies are not  
620 straightforward to determine, and because they result in small overall conductivity (Piqueux and  
621 Christensen, 2011) and surface temperature (Kieffer, 2013) changes at the expense of longer processing  
622 time. In the context of the InSight heat-flow experiments. However, subtle conductivity variations may  
623 need to be accounted for. Therefore, the dependence of thermal conductivity on gas pressure,  
624 porosity/density, temperature and overburden pressure/stress will be considered in this section.

625 Because of the discontinuous nature of the solid phase, with inter-grain regions impeding the flow of  
626 heat from grain to grain, the bulk regolith conductivity is strongly influenced by the pore-filling CO<sub>2</sub> gas  
627 conductivity (~0.01 W/(m K) at 220K). In rarefied gas environments, where the mean free path of gas  
628 molecules is similar to the volume that encapsulates them (i.e., the pore space) as is the case in the  
629 Martian regolith, small pressure variations can result in noticeable bulk conductivity changes. Laboratory  
630 experiments have quantified this effect (Fountain and West, 1970; Presley and Christensen, 1997a), and  
631 numerical models also include it (Piqueux and Christensen, 2009b). The effect of gas pressure on the bulk  
632 conductivity is described by the empirical Equation 9 (modified from Presley and Christensen, 1997b):

$$k = (CP^{0.64})d^{-0.125 \log(\frac{P}{K})} \quad (9)$$

633 with  $C = 0.001262$ ,  $K = 107990$  hPa,  $d$  is the grain diameter in  $\mu\text{m}$ , and  $P$  is pressure in hPa. This equation  
 634 is dimensionally unbalanced and was derived by Presley and Christensen (1979b) from log-log plots of  
 635 laboratory measurements of thermal conductivity as a function of gas pressure for different grain sizes in  
 636 the range of 11 to 900  $\mu\text{m}$ . The equation is not based on a theoretical analysis of heat transfer in granular  
 637 media. Figure 7 shows the predicted variation of the bulk conductivity as a function of the atmospheric  
 638 pressure using Equation (9). For a given location, the  $\sim 30\%$  seasonal variation of the atmospheric pressure  
 639 due to the  $\text{CO}_2$  cycle at the poles (Leighton and Murray, 1966; Hess et al., 1979) induces  $\sim 10\%$  of  
 640 conductivity variation. A simplification of Equation (9) gives (Figure 10):

$$k(P + \Delta P) = k_0(P) \cdot (1 + A \cdot \Delta P + B \cdot \Delta P^2) \quad (10)$$

641 where  $k(P + \Delta P)$  is the thermal conductivity at a pressure with  $\Delta P$  the atmospheric pressure deviation  
 642 (in hPa) from the local mean pressure  $P$  and  $k_0(P)$  the nominal regolith conductivity at pressure  $P$ .  $A =$   
 643  $5.173 \text{ hPa}^{-1}$  and  $B = -2.416 \cdot 10^{-1} \text{ hPa}^{-2}$  are coefficients derived from a fit based of Equation (10) and Figure  
 644 7. Coefficients in Equations 9 and 10 are only valid for the range of range of grain sizes and pressures  
 645 used in the Presley and Christensen (1979b) laboratory experiments.

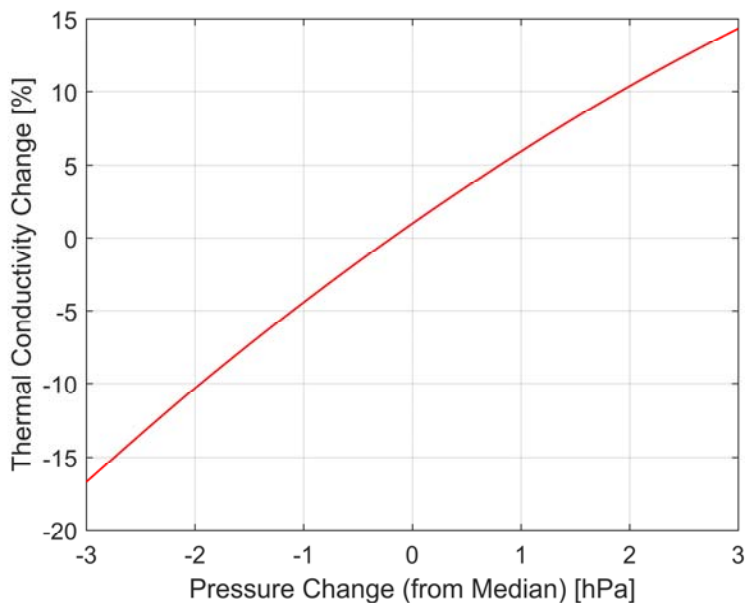


Figure 7: Relationship between thermal conductivity change and atmospheric pressure based on data from Presley and Christensen (1997b).

646 In addition, we note that Equations 9 and 10 do not apply for strongly cemented material. With  
647 indurated material, the relatively low pore-filling gas conductivity that enables heat transfer in the high  
648 impedance inter-grain region is replaced by high-conductivity inter-granular material (solids such as salts  
649 or ices are several orders of magnitude more conductive than rarefied CO<sub>2</sub> gas) and control the  
650 dependence of  $k$  on the temperature and pressure (Piqueux and Christensen, 2009b). As a result, the  
651 bulk thermal conductivity of cemented regolith is less dependent on atmospheric pressure variations.  
652 Equation 10 only provides an upper limit to the dependence on pressure. We note that the interpretation  
653 of remote sensing thermal infrared data is not consistent with a fully encrusted regolith, but does not  
654 exclude a very slight surface induration (Golombek et al. 2017). We anticipate Equation 10 to be adequate  
655 in the nominal landing region.

656 Laboratory experiments (Fountain and West, 1970; Presley and Christensen, 1997a) and theoretical  
657 considerations (Piqueux and Christensen, 2009b) indicate that the porosity of the Martian regolith  
658 partially controls the bulk thermal conductivity. High porosities are generally associated with lower bulk  
659 conductivities.

660 Fountain and West (1970) (their Figure 3) used samples typically finer than those expected at the  
661 InSight landing site (i.e., 37-62  $\mu\text{m}$ ), and they found an  $\sim 200\%$  increase in bulk conductivity for a  $\sim 50\%$   
662 increase of the density (ignoring their very low density samples). Based solely on numerical modeling,  
663 Piqueux and Christensen (2009b) found a doubling of the bulk conductivity associated with a doubling of  
664 the density (their Figure 7). Presley and Christensen (1997b) observed a  $\sim 30\%$  increase of the bulk  
665 conductivity for a 30% increase of the density for Kyanite samples at all pressures tested, a trend  
666 consistent with modeling by Piqueux and Christensen (2009b), but significantly less pronounced than that  
667 by Fountain and West (1970). We propose to adopt a linear conductivity dependency on density that  
668 conforms with the most recent laboratory work models (i.e., work by Presley and Christensen (1997b),  
669 and Plesa et al. (2016)):

$$k(\rho+\Delta\rho)= k_0(\rho) \cdot (1 + 0.005 \cdot \Delta\rho) \quad (11)$$

670 where  $k(\rho+\Delta\rho)$  is the thermal conductivity with  $\Delta\rho$  the change in regolith density (in %) from the nominal  
671 density  $\rho$ , and  $k_0(\rho)$  the conductivity with the nominal density.

672 Under most Martian surface conditions, including those expected at the InSight landing site, although  
673 radiative heat transfer probably dominates in the atmosphere (e.g., Martinez et al., 2014) it is small

674 compared to other mechanisms in the regolith (Vasavada et al., 1999) and is therefore ignored in the  
675 analysis here. Apart from radiative heat transport, temperature also controls the pore-filling gas  
676 conductivity, as well as the solid phase conductivity. The solid phase conductivity is only weakly linked to  
677 the bulk regolith conductivity, such that temperature induced variations of the solid phase conductivity  
678 can usually be ignored.

679 A theoretical quantification of the bulk conductivity dependency on the gas conductivity is a difficult  
680 problem because of the complex geometry of the gaseous phase and its relationship to the solid phase.  
681 Increasing the regolith temperature increases the intrinsic conductivity of the pore filling gas (Vesovic et  
682 al., 1990), but also decreases the mean free path, reducing the efficiency of the gaseous heat transfer. A  
683 quantitative comparison of these two opposite mechanisms requires numerical modeling and indicates  
684 that the reduction of the mean free path has a very small effect compared to the general bulk gas  
685 conductivity increase with temperature (Piqueux and Christensen, 2009b; 2011). As a result, increasing  
686 the temperature in stagnant CO<sub>2</sub> gas and with pressures consistent with Mars increases the bulk  
687 conductivity of the regolith, as confirmed by laboratory measurements (Fountain and West, 1970).  
688 Piqueux and Christensen (2011) compared the temperature effect on  $k$  predicted by their model with the  
689 data published by Fountain and West (1970), and results are shown in Figure 8.

690 Generally, the numerical model predicts a larger temperature-dependency than observed in the  
691 laboratory, over a wide range of material density and temperatures. While Fountain and West (1970) do  
692 not formally provide a relationship between temperature and bulk conductivity, their data indicates a  
693 ~15-20% increase in bulk conductivity over 100K (Figure 8), in line with the expected increase in pore-  
694 filling gas conductivity over this range of temperatures. For comparison, a Piqueux and Christensen (2011)  
695 model emulating these laboratory conditions found a ~30% increase over 100K (Figure 8), which is  
696 remarkably close to the experimental observations given the numerous modeling assumptions. Given  
697 that the temperature dependence of the pore fill gas is the major contribution to the thermal change, we  
698 propose as square-root dependence of regolith thermal conductivity on temperature, consistent with the  
699 kinetic theory of gases. Bulk conductivity as a function of temperature  $k(T)$  where  $T$  is temperature (in  
700 K) is then given by

$$k(T) = k_0(T_0) \sqrt{T/T_0} \quad (12)$$

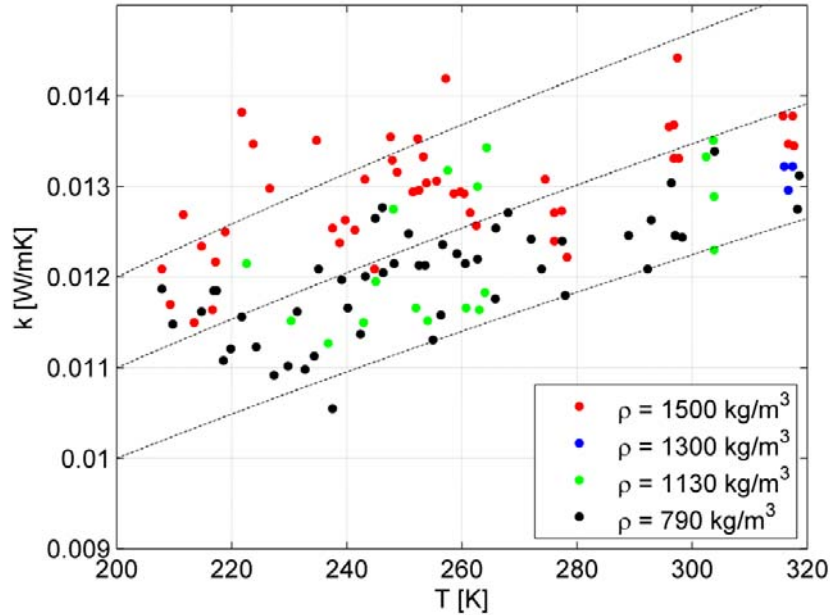


Figure 8: Comparison between thermal conductivity measurements of 37–62  $\mu\text{m}$  particles of basalt under 7 hPa of  $\text{CO}_2$  gas as a function of the temperature by Fountain and West (1970) (dots) and thermal conductivity trend modeled using Equation 6 (dashed lines).

701 where  $T_0$  and  $k_0$  are the nominal temperature (in K) and regolith conductivity (in W/m K), respectively. A  
 702 fit to the data by Fountain and West (1970) is shown in Figure 8, demonstrating that this approximation  
 703 is appropriate for the range of temperatures expected to be encountered on Mars. Again, this trend only  
 704 applies for unconsolidated material in the presence of rarefied gas. In the case of a duricrust, Equation  
 705 12 does not apply because the gas conductivity does not dominate the bulk conductivity, and the thermal  
 706 conductivities of solid (cementing) phases generally decrease with increasing temperature, following a  
 707 trend opposite to Equation 12. As a result, the dependence of  $k$  with  $T$  in the case of indurated material  
 708 is nonlinear and too complicated to predict without ad hoc models (Piqueux and Christensen 2011).

709 An increase of the confining pressure, for example as a result of the progression of the  $\text{HP}^3$  mole, is  
 710 expected to result in an increase of the bulk regolith conductivity by increasing the contact area between  
 711 grains (Hertz, 1895), hence facilitating the flow of heat from grain to grain at the expense of the relatively  
 712 inefficient (but dominating) gaseous heat transfer. Elasticity theory suggests that contact area, and thus  
 713 thermal conductivity, should scale with stress  $\sigma$  to the power of one third, but different scaling relations  
 714 with other power law dependence have also been suggested (e.g., Pilbeam and Vaisnys, 1973). However,  
 715 current laboratory data is most consistent with a power law scaling close to the classical value, and

$$k = k_0 \left( \frac{\sigma}{\sigma_0} \right)^{1/3} \quad (13)$$

716 has been established for monodispersed spheres as well as for lunar analogue material (Sakatani et al.,  
717 2016), where  $k_0$  is the conductivity at pressure  $\sigma_0$ .

718 Apart from the action of the HP<sup>3</sup> mole, stress anisotropy of the regolith itself could have an influence  
719 on regolith thermal conductivity. Stress anisotropy is generally described in terms of the dimensionless  
720 coefficient of lateral stress

$$K_0 = \frac{\sigma_h}{\sigma_v} \quad (14)$$

721 where  $\sigma_h$  and  $\sigma_v$  are the stresses in the horizontal and vertical directions, respectively. For normally  
722 consolidated soils,  $K_0$  is usually between 0.4 and 0.5, consistent with Jaky's formula  $K_0 = 1 - \sin(\phi)$  (Jaky,  
723 1944) for angles of internal friction  $\phi$  close to 30°. Stress anisotropy may then introduce anisotropy into  
724 the thermal conductivity, i.e., conductivity may vary between the horizontal and vertical directions. While  
725 this effect may be pronounced on airless bodies, it will be largely mitigated on Mars by the pore filling CO<sub>2</sub>  
726 gas.

727 In order to estimate the magnitude of the expected effect, the contribution of the pore filling gas to  
728 the total thermal conductivity can be estimated by writing  $k_{h,v} = k_{sol,h,v} + k_{gas}$ , where  $k_{sol}$  and  $k_{gas}$  are the  
729 solid and gas conductivity part of the thermal conductivity, and subscripts  $h$  and  $v$  refer to the horizontal  
730 and vertical direction, respectively. Using Equations (13) and (14), thermal conductivity in the horizontal  
731 direction can then be expressed as

$$k_h = k_{sol,v} K_0^{1/3} + k_{gas} \quad (15)$$

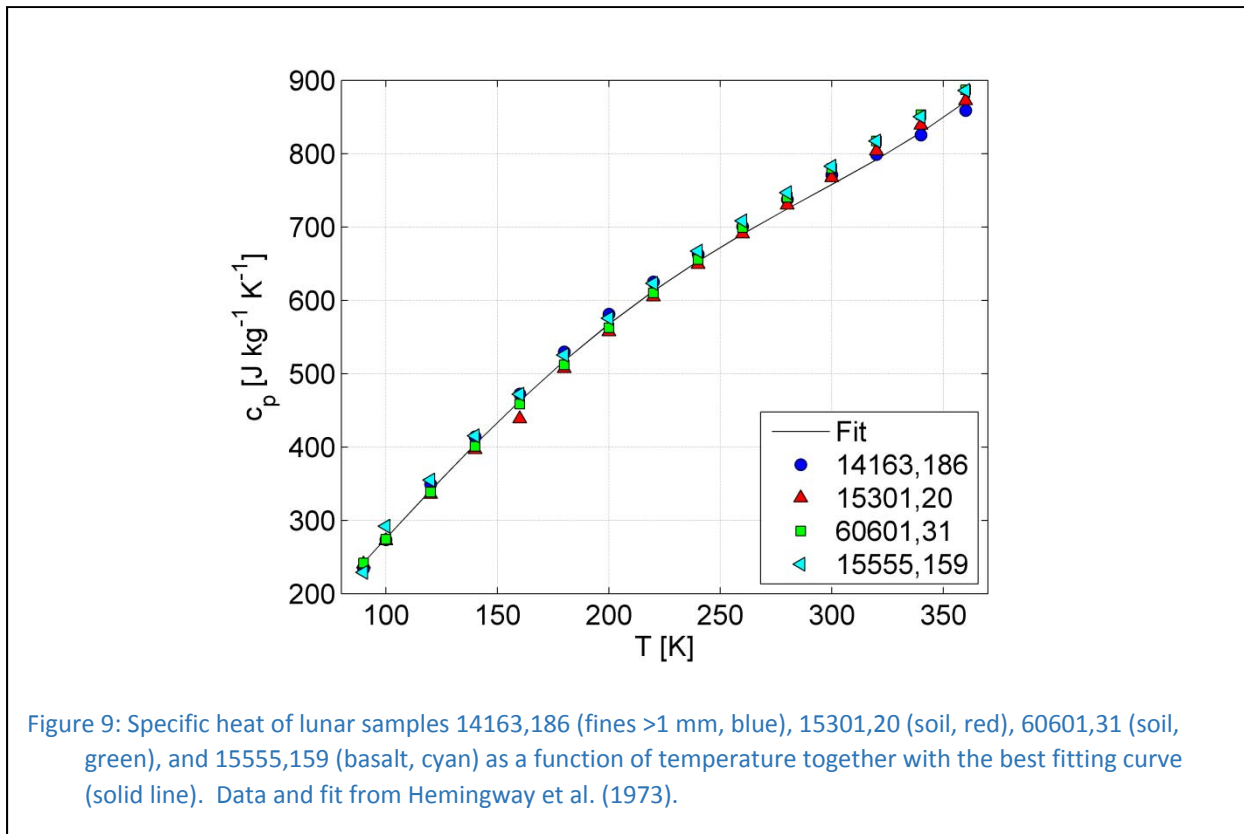
732 Hütter et al. (2008) give thermal conductivities of 0.008 and 0.057 W/(m K) for 100 – 200 µm diameter  
733 glass beads under vacuum and 8 hPa pressure conditions, respectively, and we therefore assume  $k_{gas} =$   
734 0.049 W/m K) and  $k_{sol,v} = 0.008$  W/(m K) respectively. Note that these grain sizes closely correspond to  
735 the expected grain size range at the InSight landing site derived from surface thermal inertia, which results  
736 in 150 µm diameter grains. Then, for normally consolidated soil,  $K_0 = 0.5$  and  $k_h$  is expected to be smaller  
737 than  $k_v$  by about 2-3%. Note that this effect is even less pronounced for larger grain sizes, and can likely  
738 be ignored in the context of the InSight mission.

739 **3.5. Specific Heat**

740 The specific heat of rocks and soils at low temperatures has been studied for lunar samples (Robie et  
 741 al., 1970; Fujii and Osako, 1973; Hemingway et al., 1973), and a strong temperature dependence has been  
 742 found. The suite of materials studied includes particulate material such as lunar fines and soils, but  
 743 brecciated lunar rocks as well as basalts have also been studied. A best fit to the lunar soils data was given  
 744 by Hemingway et al. (1973) and the specific heat can be approximated as

$$c_p = -A + BT + CT^2 - DT^3 + ET^4 \tag{16}$$

745 where  $c_p$  is specific heat in units of J/(kg K), and  $A$ ,  $B$ ,  $C$ ,  $D$ , and  $E$  are constants with values 23.173 J/(kg  
 746 K), 2.127 J/(kg K<sup>2</sup>), 1.5008 x 10<sup>-2</sup> J/(kg K<sup>3</sup>), 7.3699 x 10<sup>-5</sup> J/(kg K<sup>4</sup>), and 9.6552 x 10<sup>-8</sup> J/(kg K<sup>5</sup>), respectively,  
 747 and  $T$  is temperature in K. This best fitting formula is accurate to within 2 percent down to 200 K and to  
 748 within 6% down to 90 K. The fit is shown along with the data in Figure 9.



749 Measurements on lunar material are in good agreement with a thermophysical model of Winter and  
 750 Saari (1969), measurements on the physical properties of meteorites performed by Yomogida and Matsui  
 751 (1983), and meteorite specific heat measurements by Consolmagno et al. (2013). It may be worth noting

752 that a trend exists with respect to the iron content of the samples, with low iron corresponding to high  
753 specific heat (Yomogida and Matsui, 1983). The contribution of the gas phase to the bulk specific heat of  
754 a soil is negligible when compared to the solid phase and is usually ignored (Piqueux and Christensen,  
755 2011).

756 While specific heat thus shows a strong temperature dependence, this is only relevant if the near  
757 surface regolith layer is considered. At depths below a few tens of cm, near surface temperature  
758 perturbations rapidly decay (e.g., Grott et al., 2007; Kieffer, 2013) such that the regolith can be assumed  
759 isothermal for the purpose of determining its specific heat. For the InSight landing site, average regolith  
760 temperatures vary between 220 and 240 K (Plesa et al., 2016), corresponding to specific heat values of  
761 612 and 653 J/(kg K) such that  $c_p = 630$  J/(kg K) may be assumed.

### 762 **3.6. Thermal Diffusivity**

763 Thermal conductivity and specific heat are the most useful quantities in terms of modeling thermal  
764 fluxes in the regolith and are probably the most physically meaningful. In practical applications, however,  
765 they are often replaced by derived quantities that are either directly measurable or convenient shorthand  
766 in equations. Apart from thermal inertia, which describes the reaction of surface temperatures to  
767 harmonic temperature forcing and was introduced in section 3.2, thermal diffusivity can be used to  
768 describe heat diffusion in the subsurface. Thermal diffusivity  $\kappa$  is defined as

$$\kappa = k / (\rho c_p) \quad (17)$$

769 where  $k$  is thermal conductivity,  $\rho$  is density, and  $c_p$  is specific heat. It is a particularly useful quantity if  
770 material parameters can be assumed to be constant, and in this case the heat diffusion equation (Equation  
771 3) takes a particularly convenient form. As can be seen from Equation (17), an increase in thermal  
772 conductivity has the effect of a corresponding decrease in specific heat, which implies that thermal  
773 diffusivity is somewhat less sensitive to changes in density (which is most sensitive to porosity in the  
774 regolith) than thermal conductivity. Over a narrow temperature and depth range,  $\kappa$  can therefore be  
775 approximated as a constant, thus facilitating analytical solutions of the heat conduction equation. It is  
776 worth noting that estimates of thermal diffusivity from the attenuation of the diurnal temperature wave  
777 on the Moon did not show any systematic effects below a depth of 50 cm (Langseth et al., 1976), and this  
778 may be a valid approximation for the Martian subsurface as well. In this case,  $\kappa = 3.6 \times 10^{-8}$  m<sup>2</sup>/s would be  
779 a reasonable estimate at the InSight landing site.

780 For planetary regoliths in general, it is the thermal conductivity whose effect dominates the behavior  
781 of  $\kappa$  which on Mars can span two orders of magnitude and be strongly temperature-dependent, whereas  
782 the range of both density  $\rho$  and specific heat  $c_p$  are usually rather narrowly constrained. If depth  
783 dependence of thermal diffusivity is deemed to be important, appropriate values for  $\kappa(P, \rho, T, c_p(T))$  can  
784 easily be computed by inserting Equations 10, 11, 12, and 16 into Equation 17.

785

## 786 **4. Regolith Elastic Properties**

787 This section deals with the elastic properties of the regolith, which characterize its influence on the  
788 seismic wavefield as recorded by the SEIS (Seismic Experiment for Interior Structure) instrument. The  
789 relevant parameters discussed here are compressional wave velocity  $v_p$ , shear wave velocity  $v_s$ , Poisson's  
790 ratio  $\nu$  which can be derived from these velocities, elastic modulus  $E$  which can be expressed in terms of  
791 the above quantities and density  $\rho$ , as well as the seismic quality factor  $Q$ .

### 792 **4.1. Seismic Velocities and Poisson's ratio**

793 Poisson's ratio  $\nu$  describes the relation between transverse strain  $\varepsilon_{\perp}$  and axial strain  $\varepsilon_{\parallel}$  when a uniaxial  
794 stress is applied

$$\nu = - \frac{d\varepsilon_{\perp}}{d\varepsilon_{\parallel}} \quad (18)$$

795 It is directly related to the seismic P- and S-wave velocities  $v_p$  and  $v_s$  by

$$\nu = \frac{\left(\frac{v_p}{v_s}\right)^2 - 2}{2\left(\left(\frac{v_p}{v_s}\right)^2 - 1\right)} \quad (19)$$

796 with higher values of  $\nu$  related to smaller shear resistance, and higher  $v_p / v_s$ .

797 In contrast to thermophysical properties, for which estimates can be based on remote sensing data  
798 from Mars, or other mechanical properties, for which data are available from other Martian landing sites,  
799 there are currently no in situ measurements of seismic velocities of the Martian regolith. Estimates thus

800 have to be based on laboratory experiments with analogue materials on Earth while also considering field  
801 and lab data gathered for lunar regolith and terrestrial sands.

802 Both  $v_p$  and  $v_s$  were determined by Delage et al. (2017) for three Martian regolith soil simulants  
803 under various confining pressures corresponding to lithostatic stresses from 5 m to more than 60 m  
804 depth on Mars. The Mojave simulant, provided by JPL, is a mixture of MMS simulant, containing alluvial  
805 sedimentary and igneous grains from the Mojave Desert, with basaltic pumice. The Eifelsand simulant  
806 from DLR is a mixture of crushed basalt and volcanic pumice sand. The MSS-D simulant, also from DLR,  
807 is an artificial sediment made of a 50/50 mixture of crushed olivine and quartz sand, with a bimodal  
808 grain-size distribution, and olivine particles smaller than expected at the InSight landing site. As the  
809 MSS-D particles are in the silt-size range (50% of particles smaller than 70  $\mu\text{m}$ , and as small as 2  $\mu\text{m}$ ),  
810 much finer than the particle sizes estimated for the regolith at the landing site (Golombek et al., 2017),  
811 and are angular rather than rounded, the results more relevant to the InSight landing site are those for  
812 the Mojave and Eifelsand simulants. The ejecta that form the Martian regolith are expected to be  
813 rounded due to long term exposure to wind action in low atmospheric pressure conditions, in contrast  
814 to lunar regolith particles that are not submitted to any wind and, as a result, are more angular. The  
815 Mojave simulant contains both rounded and more angular grains and their particle size distribution is  
816 closer to the landing site estimates, at least when using only particles smaller than 2 mm, as was done in  
817 the laboratory measurements.

818 During the laboratory tests on Mojave simulant, Delage et al. (2017) observed no effect of stress cycles  
819 on the values of seismic velocities, and hence no difference between the effect of either plastic (first stress  
820 application) or elastic response along the compression strain. They found that the increase in velocity  
821 was more sensitive to the increase in inter-granular forces resulting from an increase in confining stress,  
822 and, to a lesser extent, to the corresponding increase in density. Data along three successive stress paths  
823 as well as from tests carried out on two different samples showed good agreement. The smallest confining  
824 stress used in these tests was 25 kPa, which approximately corresponds to 5 m depth on Mars, so the  
825 properties of the regolith at shallower depth have to be extrapolated.

826 For all regolith simulants, a power-law increase of velocities with depth was observed, defined in  
827 relation to confining stress  $\sigma_0'$  (in kPa) by an empirical law (Santamarina et al., 2001) given as:

$$v = \alpha \left( \frac{\sigma_0'}{1 \text{ kPa}} \right)^\beta \quad (20)$$

828 and where  $\alpha$  and  $\beta$  are experimentally determined.  $\alpha$  is the velocity of the velocity of the material  
 829 subjected to 1 kPa confinement;  $\beta$  is non-dimensional. This kind of velocity-depth dependence is also  
 830 common for terrestrial soils (e.g., Faust, 1951; Prasad et al., 2004). Fitting the laboratory measurements  
 831 for  $v_p$  resulted in a value of 0.3 for the exponent  $\beta$  and, using the velocity values of 250 m/s at 25 kPa and  
 832 600 m/s at 500 kPa, a value of  $\alpha = 95$  m/s for the compressional velocity at 1 kPa confining stress. Surface  
 833 velocities are derived assuming an atmospheric pressure of 0.6 kPa, and 81.5 m/s and 48.8 m/s for P- and  
 834 S-waves, respectively. Theoretical estimates based on contact theory result in values of 1/6 for  $\beta$  for  
 835 Hertzian contacts between elastic spheres and 1/4 for cone to plane contacts (expected for rough to  
 836 angular particles) as well as for spherical particles with yield. Observed values for  $\beta$  for terrestrial sands  
 837 vary from 1/3 to 1/6 (e.g., Zimmer et al., 2007).

838 Calculating the increases of confining stress with depth corresponding to the three density curves  
 839 presented in Figure 3 leads to three corresponding velocity-depth profiles (Figure 10). However,  
 840 differences between the three profiles are barely distinguishable, which is to be expected given the  
 841 reported limited influence of density on the velocity increase with depth.

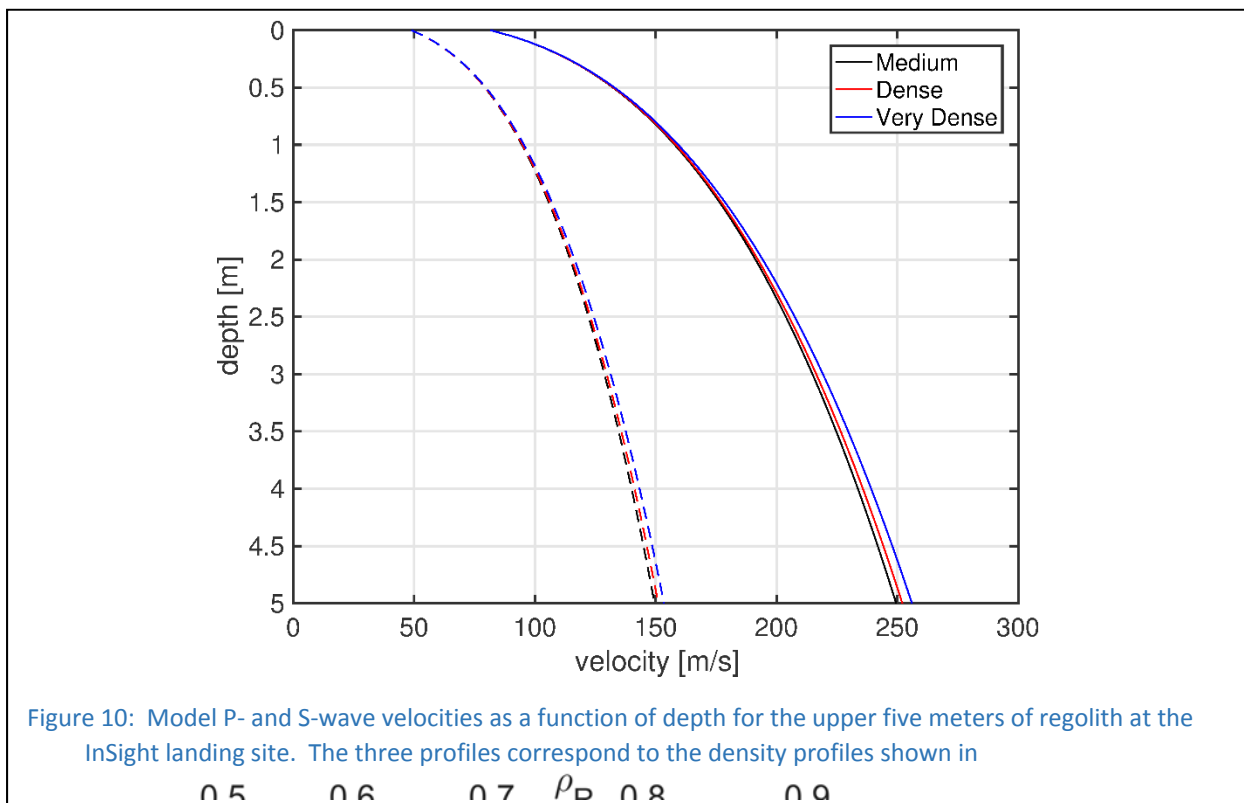


Figure 10: Model P- and S-wave velocities as a function of depth for the upper five meters of regolith at the InSight landing site. The three profiles correspond to the density profiles shown in

0.5 0.6 0.7  $\rho_D$  0.8 0.9

842 Equation 20 and the velocity measurement on the Mojave simulant have already demonstrated an  
843 important application in modeling the different seismic noise sources that may affect the InSight  
844 seismometers at various frequencies (Mimoun et al., 2017), although strictly speaking this model is only  
845 sensitive to the shear modulus and Poisson's ratio as the model is mostly integrating noise sources from  
846 static loading. For example, atmospheric pressure fluctuations on Mars induce an elastic response in the  
847 ground creating ground tilt, detectable as a gravity signal on the InSight seismometer SEIS. The amplitude  
848 of this pressure noise depends on the shear modulus and Poisson's ratio of the ground that are related,  
849 and may be derived from the seismic velocities and an assumed bulk density (Murdoch et al, 2017a). A  
850 further example is dynamic pressure due to wind that results in stresses on the InSight lander body and  
851 leading to ground deformation at the lander feet (Murdoch et al., 2017b). To calculate the resulting  
852 ground deformation at the seismometer's ground position for a given wind dynamic pressure and  
853 direction, local elastic properties beneath each foot of the lander are required. Seismic velocities may be  
854 obtained from equation 20 by taking into account the pressure exerted by the lander mass under Martian  
855 gravity and the elastic properties (shear modulus and Poisson's ratio) can then be derived. The noise  
856 maps produced by Murdoch et al. (2017b), based on these calculations, will assist in deploying SEIS at a  
857 site with little noise due to wind-induced ground deformation generated by the lander.

858 For  $v_s$ , no relation corresponding to Equation (20) was derived by Delage et al. (2017). However, it was  
859 found that the ratio between  $v_p$  and  $v_s$  remained rather constant for different confining stresses and for  
860 the different simulants tested. Thus, the values of  $v_s$  shown in Figure 10 are derived from  $v_p$  using the  
861 measured ratio of 1.669. The Poisson's ratio  $\nu$  calculated via Equation (19) accordingly is 0.22 (Delage et  
862 al., 2017).

863 The velocity profiles in Figure 10 assume that the regolith is composed purely of sandy material. Rock  
864 abundance at the landing site is low (see section 1.2), though, and a fraction of 5% or 10% rocks would  
865 increase velocities  $v_p$  and  $v_s$  by less than 0.5% and less than 1.25%, respectively, for all three models. This  
866 estimate is based on using the Reuss average, as in Delage et al. (2017), and assuming rock properties of  
867  $v_p = 3000$  m/s,  $v_s = 1700$  m/s and  $\rho = 2760$  kg/m<sup>3</sup> derived from terrestrial data obtained for fractured  
868 basalt (Planke et al., 1999; Vinciguerra et al., 2005; Stanchits et al., 2006; Fortin et al., 2011) as well as a  
869 negligible influence of compression on the rocks within the upper 5 m of the regolith. An example of  
870 extending the velocity model to greater depths to include the coarse ejecta layer and the transition from  
871 fractured to pristine basalt can be found in Knapmeyer-Endrun et al. (2017).

872 Terrestrial lab measurements on unconsolidated dry quartz sand result in P-wave velocities around  
873 250 m/s and S-wave velocities around 150 m/s for confining stresses below 50 kPa (e.g., Velea et al., 2000;  
874 Zimmer et al., 2002; Prasad et al., 2004). A terrestrial field experiment on soil with a low water content  
875 yielded P-wave velocities as low as 150 m/s and S-wave velocities as low as 100 m/s directly at the surface  
876 (Uyanik, 2010), whereas field measurements on beach sand showed P-wave velocities as low as 40 m/s  
877 and an average of 160 m/s above the water table at 1.4 m depth (Bachrach et al., 1998). A summary of  
878 terrestrial field results from exploration studies also finds P-wave velocities around 200 m/s in shallow  
879 soils (Ohsaki and Iwasaki, 1973). Thus, the regolith velocity models are within the range observed for  
880 terrestrial unconsolidated sands and soils.

881 The measured Poisson's ratio of 0.22 is low compared to values typically assumed for terrestrial  
882 sediments. It is close to laboratory data for dry quartz sands: saturated sands show much larger Poisson's  
883 ratios, in excess of 0.4, and corresponding  $v_p/v_s$  ratios up to and larger than 5 (Ohsaki and Iwasaki, 1973;  
884 Prasad et al., 2004). The field experiment on beach sand also yielded a low Poisson's ratio of 0.15  
885 independent of depth (Bachrach et al., 2000). The field measurements by Uyanik (2010) resulted in a  $v_p/v_s$   
886 ratio of 1.5, corresponding to a Poisson's ratio of 0.1, for the upper tens of cms of dry unconsolidated top-  
887 soil, indicating a porous and air-filled environment. These observations demonstrate the strong influence  
888 of water content on Poisson's ratio in unconsolidated sands and soils. As no free near-surface water is  
889 expected in the regolith at the landing site, but the layer is expected to be porous and to exchange gases  
890 with the atmosphere, the low Poisson's ratio and  $v_p/v_s$  ratio corresponding to values obtained from the  
891 laboratory experiments are plausible first estimates for the InSight landing site.

892 For the Moon, seismic velocities at the surface initially derived from the touchdown of the Surveyor  
893 spacecraft yielded very low values of 45 m/s for  $v_p$  and 23 m/s for  $v_s$ , corresponding to a Poisson's ratio  
894  $\nu$  of 0.32 (Sutton and Duennebie, 1970). Active seismic experiments of Apollo 14, 16 and 17 found  
895 somewhat higher P-wave velocities of the lunar regolith of 100 to 114 m/s in the upper 4 to 12.2 m, with  
896 higher velocities in the range of 250 to 330 m/s at greater depth (Kovach and Watkins, 1972; Watkins and  
897 Kovach, 1972, 1973; Cooper et al., 1974). The  $v_p$  values for the uppermost regolith layer agree well with  
898 estimates based on the recordings of the lunar module liftoff with the passive seismic experiments at  
899 Apollo 12, 14 and 15, which are in the range of 99 to 103 m/s (Nakamura et al., 1975). Laboratory  
900 measurements on lunar soils returned to Earth gave similarly low values for P-wave velocities of 125 m/s  
901 at 4 kPa (Johnson et al., 1982). Gangi and Yen (1979) interpreted the data from the Apollo 14 and 16  
902 active seismic experiments in terms of a power-law increase of P-wave velocity with depth in the regolith

903 layer, with an exponent of  $1/6$  as predicted by contact theory and a velocity of 110 m/s at the surface,  
904 which was, however, contested by Watkins and Kovach (1973), claiming that this velocity law does not  
905 provide a good fit to the layered Apollo models.

906 Shear wave arrivals were only tentatively identified in the active recordings of Apollo 14, resulting in  
907 an S-wave velocity estimates of 62 m/s and a Poisson's ratio  $\nu$  of 0.23 for the lunar regolith (Kovach and  
908 Watkins, 1973), quite similar to the proposed model for the InSight landing site. Additional information  
909 has been derived from the passive lunar experiments, e.g., horizontal-to-vertical spectral ratios (H/V) of  
910 artificial and natural impacts as well as deeper events (Mark and Sutton, 1975; Horvath et al., 1980). Lunar  
911 S-wave velocities were in the range of 32 to 40 m/s at the surface, with values greater than 100 m/s found  
912 only below 10 m depth. Resulting Poisson's ratios are 0.41 to 0.43 at the surface, decreasing to 0.33  
913 below. Analysis of Rayleigh waves extracted from ambient noise correlations at the Apollo 17 geophone  
914 array yielded S-wave velocity values of 50 m/s for the uppermost 2 m, increasing to 70 m/s at 4 m depth,  
915 and a Poisson's ratio around 0.33 (Larose et al., 2005; Sens-Schönfelder and Larose, 2010). A recent re-  
916 analysis of horizontal to vertical spectral ratio (H/V) curves in combination with Rayleigh wave dispersion  
917 from the active experiments at Apollo 14 and 16 yielded S-velocities of 50 to 60 m/s for the upper 12 to  
918 15 m (Dal Moro, 2015), and Poisson's ratios around 0.33. In contrast, re-analysis of Apollo 17 active  
919 seismic data using wavefield gradient analysis resulted in S-wave velocities of 40 m/s for the upper 4 m,  
920 underlain by 110 m/s. A Poisson's ratio  $\nu$  of around 0.41 was indicated in the shallowest layer (Sollberger  
921 et al., 2016).

922 While the low velocities of the lunar regolith are surely due to a high porosity (Tittmann et al., 1972),  
923 which also has a profound effect on velocities in terrestrial field experiments (Watkins et al., 1972), the  
924 vacuum does not play a major role. In experiments using a granular material consisting of glass beads,  
925 Griffiths et al. (2010) observed no difference between seismic velocities measured in vacuum and in  
926 ambient air, and only a relatively small decrease of a few percent for vacuum compared with 0.6%  
927 interstitial water, even at low confining pressure. In fact, the P-wave velocities for the shallowest layer  
928 measured during the Apollo program are in good agreement with terrestrial field measurements on sand  
929 and the predictions for the InSight landing site. The velocity law derived by Gangi and Yen (1979) predicts  
930 a much smaller increase of velocity with depth compared to the InSight landing site model (Figure 10). To  
931 a large extent, the resulting lower velocities at depth can be explained by reduced compaction under the  
932 diminished gravity of the Moon, although variations in grain size with depth might also affect the profile  
933 (Pilbeam and Vaišnys, 1973). Most measured lunar S-velocities are somewhat lower, and the Poisson's

934 ratio accordingly higher, than predicted for the InSight landing site and found in dry terrestrial samples.  
935 However, the spread in  $v_s$  estimates, and correspondingly Poisson's ratio, for the lunar regolith is  
936 significantly larger than for  $v_p$ , which may explain part of the discrepancy.

## 937 **4.2. Elastic Modulus**

938 Based on Hooke's law, the elastic or Young's modulus  $E$  describes the ratio between uniaxial tensile  
939 stress  $\sigma$  and the proportional deformation, or extensional strain,  $\varepsilon$ , and thus the stiffness of a material:

$$\sigma = E\varepsilon \quad (21)$$

940 It can be expressed in terms of the shear wave velocity  $v_s$ , Poisson's ratio  $\nu$  and density  $\rho$  as

$$E = 2v_s^2\rho(1 + \nu) \quad (22)$$

941 Depth profiles of Young's modulus for the three different models of regolith compaction are given in  
942 Figure 3. The values are lower than those obtained for some field tests on terrestrial soil, that found  $E$   
943 increasing from 30 to 90 MPa in the upper 0.6 m (Uyanik, 2010), and on sand, that deduced  $E$  between  
944 20 to 70 MPa in the uppermost meter (Jaksa et al., 2004). In their overview, Bowles (1966) quote values  
945 between 5 and 25 MPa for  $E$  in silty to loose sand and a range of 50 to 81 MPa for dense sands, though,  
946 in good agreement with values calculated here. Teanby et al. (2016) also obtained low values for the  
947 effective  $E$  in the range of 1.1 to 4.4 MPa when applying elastic theory at two sites located on very loose  
948 basaltic sands in Iceland. These values are likely appropriate only for the uppermost few centimeters of  
949 the subsurface, whereas the profiles in Figure 11 show slightly larger values around 7.5 MPa.

950 In situ measurements of Young's modulus for the Moon were not reported but Alshibli and Hasan  
951 (2009) determined  $E$  by laboratory experiments for the JSC-1A lunar regolith simulant, which is mined  
952 from a volcanic ash deposit in a commercial quarry. They measured values in the ranges of 11.1 to 15.5  
953 MPa and 10.3 to 27.6 MPa for loose and dense packing, respectively, at pressures corresponding to 2 and  
954 4 m depth on Mars (10 and 20 kPa). These values are considerable lower than the values for  $E$  calculated  
955 here, but JCS-1A has a large proportion of small grains, with more than 55% of grains smaller than 100  
956  $\mu\text{m}$ . Thus, JSC-1A is not a good analogue of the regolith at the InSight landing site.

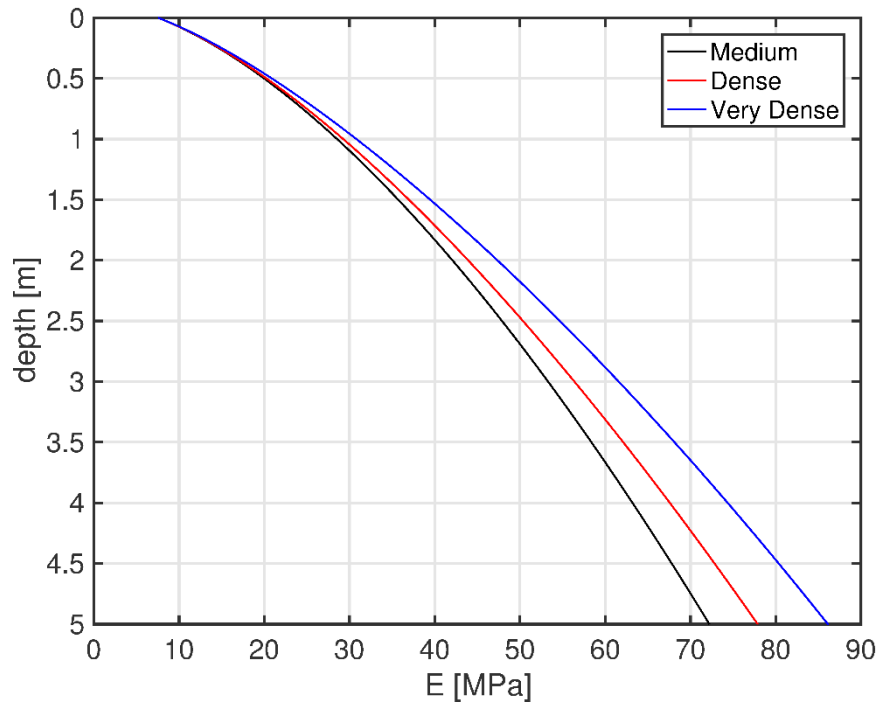


Figure 11: Models of Young's modulus as a function of depth for the upper five meters of regolith at the InSight landing site. The three profiles correspond to the density profiles shown in Figure 3 based on different states of regolith compaction.

957

### 958 4.3. Attenuation Factor

959 Seismic attenuation is the dissipation of energy through internal friction and other non-elastic  
 960 processes and affects the amplitude of seismic signals propagating through natural materials. Attenuation  
 961 is quantified by the dimensionless seismic quality factor  $Q$ , defined via the decrease of amplitude  $A$  at  
 962 frequency  $f$  after travelling a distance  $x$  through a medium with seismic velocity  $v$

$$A(x) = A_0 e^{-\left(\frac{f\pi}{Qv}\right)x} \quad (23)$$

963 (Lay and Wallace, 1995). Note that this equation defines attenuation caused by intrinsic anelasticity and  
 964 does not include apparent attenuation due to scattering, i.e., the redistribution of energy to the coda of  
 965 a seismic phase due to small-scale heterogeneity along the wave path. For the Moon, attenuation due to  
 966 intrinsic anelasticity is much lower than on Earth, while scattering in the lunar crust is much larger, which,  
 967 in combination, result in the characteristic signal shapes of lunar seismograms (e.g., Dainty and Toksöz,

968 1981). The envelope of these seismograms can be fairly well modeled by diffusion theory (see Lognonné  
969 et al., 2009; Gillet et al., 2017; for recent applications). No laboratory measurements of  $Q$  are available  
970 for Martian regolith analogues. Thus, the discussion is focused on available theories and on data from the  
971 Moon and Earth, which are clearly different, and what can be deduced from these for Mars.

972 S-wave quality factors  $Q_S$ , obtained by borehole measurements in terrestrial sediments and soils, lie  
973 between 3 and 35 (e.g., Gibbs et al., 1994; Assimaki et al., 2008; Parolai et al., 2010; Fukushima et al.,  
974 2016). From surface measurements on Quaternary sediments, Malagnini (1996) determined a frequency  
975 dependence in  $Q$  for both P- and S-waves, with  $Q_P = Q_S = 9$  at 10 Hz, compared to a value of 2 previously  
976 found at 1 Hz (Malagnini et al., 1995). Frequency dependence in  $Q$  at frequencies of a few Hz is generally  
977 attributed to the influence of scattering (e.g., Kinoshita, 2008), which we do not consider further here.  
978 Jongmans (1990) found similarly low values, on the order of 5, for  $Q_P$  in field measurements on  
979 unsaturated sand. Laboratory measurements on dry quartz sands showed  $Q_S$  in the range of 15 to 50 at  
980 lowest confining pressures below 0.3 MPa and  $Q_P$  around 10 to 15 (Prasad and Meissner, 1992).

981 In contrast to terrestrial data, Apollo experiments determined unusually high  $Q$  values in the lunar  
982 interior, ranging from 3000 to 3600 in the upper crust (Latham et al., 1970a, b) to 4000 to 4800 in the  
983 upper mantle for both P- and S-waves (Nakamura et al., 1976; Nakamura and Koyama, 1982). These high  
984  $Q$  values also extended up to the near-surface material, including the lunar regolith and the somewhat  
985 faster layer below, for which Nakamura (1976) determined 2000 as a lower limit for  $Q$  from interpretation  
986 of rover signals. Analysis of the Apollo 14 seismic experiment data gave an estimate of 50-100 for  $Q$  of  
987 the near-surface lunar material (Kovach and Watkins, 1972). Recently, Dal Moro (2015) found that high  
988  $Q_S$  values of at least 100 in the uppermost regolith and 300 below the slowest layer to a few 100 m depth  
989 in the shallow crust are essential in obtaining a good fit to measured H/V curve amplitudes. As these data  
990 cannot differentiate further between  $Q_S$  values of either a few hundred or significantly larger ( $\geq 1000$ ),  
991 they are not in conflict with previous higher estimates which averaged over larger depth ranges.

992 As demonstrated in laboratory experiments, high  $Q$  values are caused by extremely low water content  
993 in the rocks from which even thin layers of adsorbed water have been removed by strong outgassing  
994 under vacuum conditions (Tittmann, 1977; Schreiber, 1977; Tittmann et al., 1979). As discussed by  
995 Tittmann et al. (1972), laboratory measurement of  $Q$  factors on returned lunar samples failed to  
996 reproduce the high values measured in situ on the Moon when exposing the samples to laboratory air  
997 during the measurements, and values around 50 to 100 were obtained. Only by outgassing the samples

998 under high vacuum, could  $Q$  values of 3000 to 4500 be achieved, in agreement with the in situ estimates  
999 for lunar rocks. However,  $Q$  returned to the low original values after a few minutes re-exposure to  
1000 laboratory air (Tittmann et al., 1979). However, all of these measurements pertain to lunar rocks, not  
1001 fines. A similar observation was reported by Pandit and Tozer (1970) for porous terrestrial rocks, with an  
1002 increase in  $Q$  by a factor of 5 between terrestrial atmospheric pressure and 1.5 Pa. Tittmann et al. (1980),  
1003 working with porous sandstone, showed that the first monolayer of adsorbed water has the strongest  
1004 effect and decreases  $Q$  by a factor of about 5 compared to the vacuum-dry case. In the Martian crust an  
1005 evacuation of trapped fluids comparable to the lunar situation is prevented by atmospheric pressure, as  
1006 it requires successive heating cycles at pressures below 1.5 Pa (Lognonné and Mosser, 1993). Accordingly,  
1007  $Q$  is predicted to be larger by at most a factor of two compared to Earth for Martian crustal rocks.

1008 A laboratory experiment on fines was conducted by Jones (1972). Jones used powdered basalt with a  
1009 mean particle diameter of 5  $\mu\text{m}$  and a mean density of 1340  $\text{kg}/\text{m}^3$ , significantly finer than the sand at the  
1010 InSight landing site, but with a similar surface density to that estimated here. At 10 Hz Jones found a clear  
1011 increase in  $Q$  with decreasing pressure, from values of  $Q_p$  around 50 at ambient conditions to 100 at Mars  
1012 surface atmospheric pressure, to 120 at about 5 Pa. Jones inferred that remnants of lubricating water  
1013 films are still present at these pressures as compared to measurements made in a vacuum. For glass  
1014 beads, 400-800  $\mu\text{m}$  in diameter, Griffiths et al. (2010) reported differences in  $Q$  by a factor of 4.5 between  
1015 200 in ambient air with about 25% humidity, and 900 in a vacuum. Brunet et al. (2008) obtained a  $Q$  of  
1016 295 for a similar granular material of glass beads, 600-800  $\mu\text{m}$  in diameter, dried in a furnace, and  
1017 measured under ambient conditions. According to contact theory for spherical particles, certain variables,  
1018 including  $Q$ , are proportional to particle radius (Brunet et al., 2008), which could explain the different  
1019 values obtained for  $Q$  in the different experiments.

1020 Laboratory measurements on dry quartz sand yield  $Q_p/Q_s$  ratios ranging from 0.2 to 1.8 (Prasad and  
1021 Meissner, 1992; Prasad et al., 2004). Studies on porous sandstones yield equal values for  $Q_p$  and  $Q_s$  at  
1022 low confining pressures when performing measurements under ambient laboratory conditions and after  
1023 drying the samples in a laboratory oven (Toksöz and Johnson, 1979). Based on the limited information  
1024 available, we assume that  $Q_p$  and  $Q_s$  are approximately equal at the InSight landing site.

1025 One of the main factors controlling  $Q$  is the regolith water content. Laboratory measurements have  
1026 shown that a single monolayer of adsorbed water can drastically reduce the high  $Q$  values observed in  
1027 outgassed lunar or terrestrial samples (Tittmann et al., 1979, 1980). Pandit and Tozer (1970) reported

1028 that the large change in  $Q$  they observed was connected to a change in water content of less than 0.05  
1029 wt.%. Any liquid or frozen surface water would not be in equilibrium in the equatorial regions of Mars  
1030 targeted by the InSight lander and would quickly sublimate (Golombek et al., 2017). However, water  
1031 within the regolith could still be present in the form of a few monolayers of adsorbed water (Möhlmann,  
1032 2008), which would maintain liquid-like properties down to temperatures of  $-70^{\circ}\text{C}$  (Lorek and Wagner,  
1033 2013). This adsorbed water is supposed to reside mainly below depths of a few tens of cm, outside the  
1034 range of the Martian diurnal and seasonal thermal cycles (Möhlmann, 2004). Such a two-layered regolith  
1035 structure would be consistent with a model for regolith water content derived from neutron spectroscopy  
1036 data (Feldman et al., 2004), which assumes a relatively desiccated near surface layer with 2 wt.% water  
1037 and a more water-rich layer below, with at least 6 wt.% water. Furthermore, given that the Martian  
1038 regolith is expected to be in exchange with the atmosphere (see Section 6 below), it seems reasonable to  
1039 assume that monolayers of water could be present, but the amount of water in the regolith depends on  
1040 latitude and season (Martinez et al., 2017). This would also be consistent with degassing experiments  
1041 performed by the SAM (Sample Analysis on Mars) instrument suite on the Curiosity rover at Gale crater  
1042 (Leshin et al., 2013), which found loosely bound water degassing from the samples starting at around  
1043  $100^{\circ}\text{C}$ .

1044 Therefore, we provide models for  $Q$  values for the Martian regolith that are based on Mindlin theory  
1045 (Figure 12), as used by Brunet et al. (2008) to interpret their data from measurements with dry beads.  
1046 The resulting values are consistent with results obtained in lab experiments on basalt fines and granular  
1047 materials in dry, but non-vacuum conditions, taking into account estimates for regolith particle size. The  
1048 theory predicts a dependence of  $Q$  on pressure with an exponent of  $2/3$ , which is within the observed  
1049 range of 0.5 to 0.9 for spherical grains (Pilbeam and Vaišnys, 1973). Observations for angular grains found  
1050 a smaller pressure dependence with an exponent of 0.3 to 0.4 (Pilbeam and Vaišnys, 1973). The increase  
1051 of  $Q$  with depth could thus be lower if the particle grains at the landing site are less than perfectly  
1052 spherical. In addition,  $Q$  also depends on particle size. We used a particle radius of  $100\ \mu\text{m}$ , in the center  
1053 of the range for fine sand when calculating the curves in Figure 12. However, a non-uniform particle size  
1054 will result in deviation in the predicted values for  $Q$ . Specifically, if particle size increases in the upper 5  
1055 m of the regolith, the increase in  $Q$  with depth will be larger. Finally, Mindlin theory also predicts an  
1056 inverse dependence of  $Q$  on displacement amplitude which was not observed in some low pressure  
1057 experiments (Pilbeam and Vaišnys, 1973). Here we consider amplitudes related to the low end-member  
1058 strain analyzed by Brunet et al. (2008), on the order of  $5 \times 10^{-6}$ , to avoid decreasing  $Q$ .

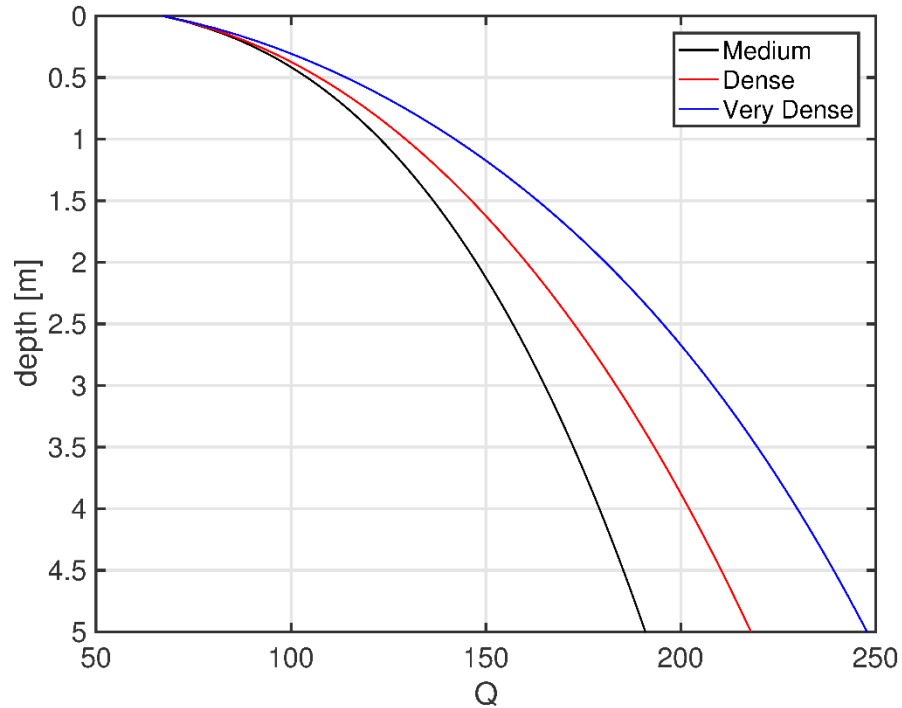


Figure 12: Models of  $Q$  as a function of depth for the upper five meters of regolith at the InSight landing site. The three profiles correspond to the density profiles shown in Figure 3 based on different states of regolith compaction.

1059 The  $Q$  values estimated here are lower than some of the estimates for the lunar regolith, but distinctly  
 1060 higher than terrestrial values. However, it is worth repeating that if no adsorbed water is present in the  
 1061 Martian regolith, Both  $Q_P$  and  $Q_S$  could be larger than the values given here by up to an order of  
 1062 magnitude.

1063 Surface waves have their amplitude maximum at one-third of their wavelengths. Thus, short period  
 1064 surface waves with a period of 7 Hz, such as those observed in autocorrelations of Apollo 17 geophone  
 1065 data from the Moon, and a group velocity of about 100 m/s based on the estimates in Section 5.1, are  
 1066 strongly influenced by the regolith layer. The range of  $Q$  deduced here would indicate approximately 5  
 1067 to 6 s of propagation time for one  $Q$  cycle, or 500 to 600 m of propagation distance for these waves.  
 1068 Amplitude could be reduced by a factor of two after 500 to 600 m of propagation, limiting the  
 1069 observational range of the waves.

1070

1071 **5. Mass Diffusivity**

1072 The section concerns the *mass diffusivity*, or *coefficient of mass diffusion*, of the Mars atmosphere with  
1073 respect to the porous medium of the regolith at the InSight landing site. This parameter is important  
1074 because the atmosphere flows in and out of the regolith in response to changes in atmospheric pressure,  
1075 and has the potential to convectively transfer heat in and out of the regolith. Convective heat transport  
1076 associated with atmospheric pressure changes could be indicated by transients in the HP<sup>3</sup> temperature  
1077 data and/or variations in calculated heat flow with depth. Mass diffusivity is somewhat analogous to  
1078 thermal diffusivity where thermal diffusivity can be used to describe heat diffusion in the subsurface (see  
1079 subsection 4.6 Thermal Diffusivity above). In a simplified form, effective mass diffusivity,  $D_{eff}$ , may be  
1080 defined by the following equation (*cf.*, Scanlon et al., 2002, equation 8.31):

$$\frac{\partial M}{\partial t} = D_{eff} \frac{\partial^2 PM}{\partial z^2} \quad (24)$$

1081 where  $M$  is mass of the diffusing gas,  $t$  is time, and  $z$  is depth. Unlike heat flow, however, in porous media  
1082 the gas molecules flow through the pores rather than through the minerals grains (heat may also be  
1083 transferred through pores by radiation). Gas molecules have random motion, influenced by pressure  
1084 gradients, and their interactions with the minerals depend on the molecular gas mean free path,  $\lambda$ , relative  
1085 to the average pore radius,  $r$ .

1086 Mass diffusivity has been measured in terrestrial regoliths (soils and subsoils) under the same  
1087 conditions of atmospheric pressure change as we are interested in Mars. Cyclic changes in atmospheric  
1088 pressure that propagate into the subsurface are commonly known as *barometric pumping* or *atmospheric*  
1089 *breathing*. On Earth they are of interest in studies of gas exchange associated with plant growth in the  
1090 vadose zone and in studies of vertical transport of contaminated gases in the porous subsurface (*e.g.*,  
1091 Nilson et al., 1991; Massmann and Farrier, 1992; Rossabi and Falta, 2002; Massmann, 2006; Rossabi,  
1092 2006). These studies are applicable to barometric pumping on Mars at the macro scale, *i.e.*, in the  
1093 pumping theory, but miss an important difference in the pressure diffusivity at the molecular scale  
1094 between Earth and Mars. As a consequence of Mars' low atmospheric pressure, molecules in the regolith  
1095 of Mars have a much higher mean free path than molecules in the terrestrial regolith. They interact more  
1096 with the pore walls than with their neighboring gas molecules, whereas terrestrial gas molecules generally  
1097 interact more with each other except in very fine-grained materials, such as shales. Terrestrial gas  
1098 molecules in porous media interact with the pore walls when the pores are very small. Pore-wall

1099 interactions are important in terms of the permeability and pressure diffusivity of the Mars regolith, and  
1100 are discussed below. There is one set of experimental measurements of pressure diffusivity under Mars  
1101 surface atmospheric conditions (Fanale et al., 1982a): these results are discussed and compared with  
1102 theoretical calculations after presentation of molecular gas interactions in porous media.

## 1103 5.1. Gas Interactions in Porous Media

1104 At low mass concentrations and in small pore passages, diffusion of gas molecules in porous media  
1105 involves collisions between the gas molecules and the porous media in addition to molecular interactions  
1106 among the gas molecules. Mass diffusivity and permeability are both parameters that relate to the flow  
1107 of fluids through porous media, but they are not simply related because mass diffusivity includes the  
1108 effects of compressibility, especially when the fluid is a gas (e.g., Liang et al., 2001). However, some of  
1109 the interactions among gas molecules with pore walls that apply to mass diffusivity were first studied and  
1110 observed in permeability. One of the interactions of gas molecules with pore walls is slip of gas molecules  
1111 near a solid wall. Klinkenberg (1941) first addressed how this interaction can affect the measured  
1112 permeability of a gas, and he proposed a linear permeability correction. Four modes of diffusion have  
1113 been described which are usually distinguished by the Knudsen number,  $K_n$  (e.g., Ziarani and Aguilera,  
1114 2012):

$$K_n = \frac{\lambda}{\delta} \quad (25)$$

1115 where  $\lambda$  is mean free path of the gas molecules and  $\delta$  is a characteristic length, such as the pore diameter.  
1116 Three of the four modes of diffusion are illustrated in Figure 13 and the four modes and their relations to  
1117 the Knudsen number are described in Table 3.

1118 For small Knudsen numbers that are applicable to most terrestrial gas flows in natural porous media,  
1119 pressure diffusivity coefficients representative of Darcy flow are appropriate. However, as the Knudsen  
1120 number increases to where slip flow on pore boundaries dominates, a new diffusion coefficient, the  
1121 Knudsen diffusivity, is more accurate (see Table 3). The Knudsen diffusion coefficient,  $D_k$ , is given by (e.g.,  
1122 Huizenga and Smith, 1986; Roy et al., 2003; Javadpour et al., 2007):

$$D_k = \frac{\delta_p}{3} \sqrt{\frac{8RT}{\pi M}} \quad (26)$$

1123 where  $\delta_p$  is the pore diameter  $R$  is the universal gas constant,  $T$  is absolute temperature, and  $M$  is the gas  
 1124 molar mass. Under conditions of Knudsen diffusion (Table 3,  $K_n > 10$ ),  $D_k$  is the appropriate diffusion  
 1125 coefficient to use in Equation 24 in place of  $D_{eff}$ .

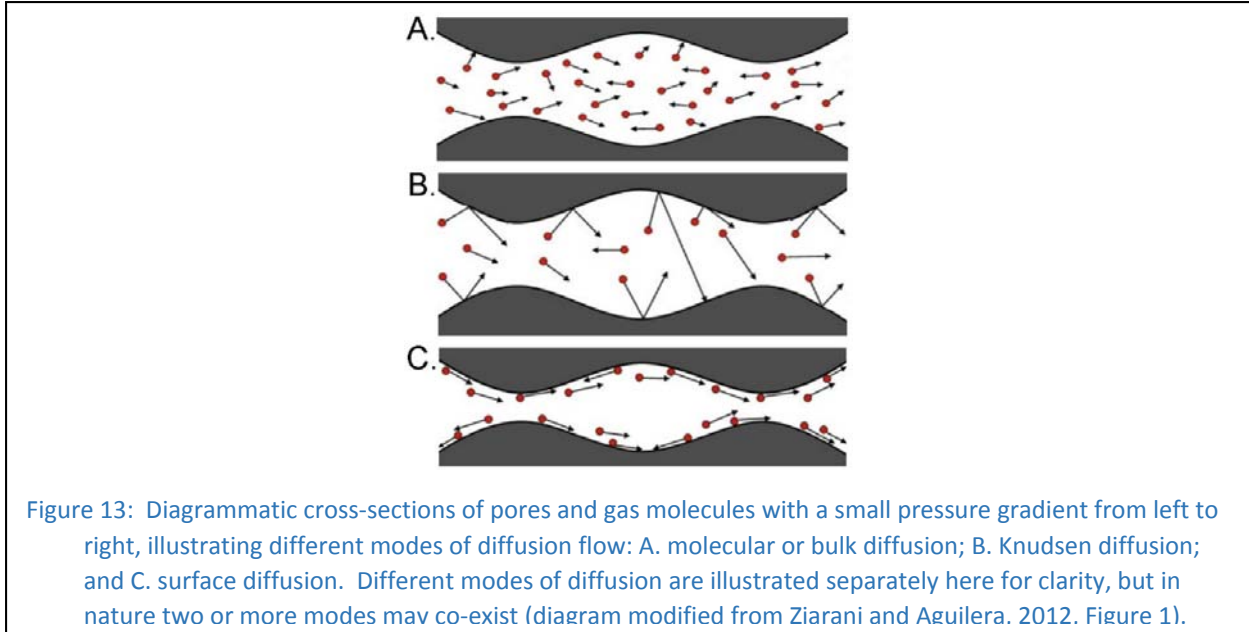


Table 3: Knudsen number and flow regimes classification for porous media (after Karniadakis et al., 2005). Calculations indicate that atmospheric flow in the regolith at the landing site is in the Transition flow regime ( $0.1 < K_n < 10$ ).

Flow Regime	Knudsen Number	Model Applied	Comment
Continuum (viscous) flow <sup>1</sup>	$K_n < 0.01$	Darcy's equation for laminar flow; Forchheimer's equation <sup>2</sup> for turbulent flow.	Assumes immobile fluid at pore wall. Hence, no permeability correction generally required.
Slip flow	$0.01 < K_n < 0.1$	Darcy's equation with Klinkenberg or Knudsen's correction.	Knudsen's equation more accurate, but Klinkenberg correction easier.
Transition flow	$0.1 < K_n < 10$	Darcy's equation with Knudsen's correction or Burnett's equation with slip boundary conditions <sup>3</sup> .	Knudsen's diffusion equation more reliable, especially when $K_n$ close to 10.
Knudsen's (free molecular) flow	$K_n > 10$	Knudsen's diffusion equation <sup>4</sup> ; alternative methods are DSMC and Lattice Boltzmann methods <sup>3</sup> .	Usually applies to shale where pore-throat radii are very small.

<sup>1</sup> Some references suggest  $K_n < 0.001$  as a limit for continuum flow (e.g., Roy et al., 2003);  
<sup>2</sup> e.g., Whitaker (1996);  
<sup>3</sup> For more detail see Agarwal et al. (2001). DSMC = Direct Simulation of Monte Carlo;  
<sup>4</sup> Knudsen diffusion can coexist with bulk and surface diffusion

## 1126 5.2. Estimating Pore Sizes

1127 Many variables contribute to the pore radii in sediments and porous rocks, including grain size, degree  
1128 of sorting, compaction, cementation, moisture content, diagenesis, and growth of secondary minerals.  
1129 There is evidence of wind and water processes on the surface of Mars, both of which would tend to sort  
1130 and round grains in the regolith. Impact processes produce angular fragments and poorly sorted  
1131 materials. The landing ellipse for the InSight landing site was chosen to be on smooth, flat terrain that  
1132 generally has a very low rock abundance and as few impact craters visible in high-resolution orbital images  
1133 as possible (Golombek et al., 2017). Selection criteria for the landing site in the northern lowlands and  
1134 with a paucity of impact craters should make impact fragmentation subordinate to abrasion as a  
1135 mechanical weathering process at the landing site. The particles in the landing site regolith may therefore  
1136 be expected to be well-sorted, rounded grains, as described in Section 2 above.

1137 Although relations have been proposed, no universal simple relation exists in sediments between grain  
1138 size and pore radii from which the pore radii may be estimated. Kaviany (1994) proposed a relation among  
1139 average pore size, particle diameter and porosity for spherical particles in random packing. If a fractional  
1140 porosity of 0.399 is assumed, representative of random packing of uniform spheres, this relation gives a  
1141 ratio of average pore size to grain size,  $\delta_p/d_g$ , of 0.072, where  $\delta_p$  is pore size and  $d_g$  is the grain diameter.  
1142 Minimum pore throat diameters were calculated geometrically assuming the most inefficient regular  
1143 packing of uniform spheres (Cubic packing, 0.476 porosity), and the most efficient regular packing of  
1144 uniform spheres (Triclinic, or hexagonal close packing, 0.260 porosity). For cubic packing the minimum  
1145 throat diameter is given by  $0.207d_p$  ( $\delta_p/d_g = 0.21$ ); for triclinic packing the minimum throat diameter is  
1146 given by  $0.0774d_p$  ( $\delta_p/d_g = 0.077$ ). Assuming a porosity representative of random packing, the ratios of  
1147 pore diameter or pore throat diameter to grain size ( $\delta_p/d_g$ ) calculated from the from the Kaviany (1994)  
1148 equation are very similar to those calculated geometrically for triclinic (close-hexagonal) packing, 0.072  
1149 versus 0.077, respectively. Cubic packing is improbable in sorted spherical grains as they are unlikely to  
1150 be balanced in vertical columns.

1151 One further complication in determining pore size from grain size is that the methods discussed above  
1152 all assume uniform spherical grains, a condition that may not exist in the Mars regolith. Variations in grain  
1153 size and deviations from spherical shape are both likely to reduce pore size as smaller grains would fill  
1154 larger pore spaces and flattening of the grains would result in compaction: reduced pore size would  
1155 reduce pressure diffusivity. However, at the InSight landing site the surface regolith sediment is likely to

1156 be well-sorted and rounded from eolian processes. Using the estimated range of grain size of 0.125 to  
1157 0.25 mm (radii 0.0625 to 0.125 mm) from Subsection 2.1 Landing Site Overview above, and an average  
1158  $\delta_p/d_g$  ratio of 0.075, a range of pore throat diameters of 9.4 to 18.8  $\mu\text{m}$  was calculated. At the InSight  
1159 landing site these pores would be subject to an atmospheric pressure range of 6 to 8.5 hPa.

### 1160 **5.3. Gas Mean Free Path and Range at Landing Site**

1161 The mean free path of molecules in a gas is estimated by considering the volume of a cylinder that  
1162 represents the gas molecules effective collision area, including the area of target molecules in this area,  
1163 with respect to the distance travelled by the molecules and the number of molecules per unit volume  
1164 (*e.g.*, Nave, 2016). The number of molecules per unit volume of gas may be approximated by assuming  
1165 that the systems behaves as an ideal gas (Tan, 2014). The calculation must also recognize that both the  
1166 colliding and the target molecules are moving (Nave, *op. cit.*). These assumptions yield the result that  
1167 the molecular mean free path,  $\lambda$ , may be estimated by:

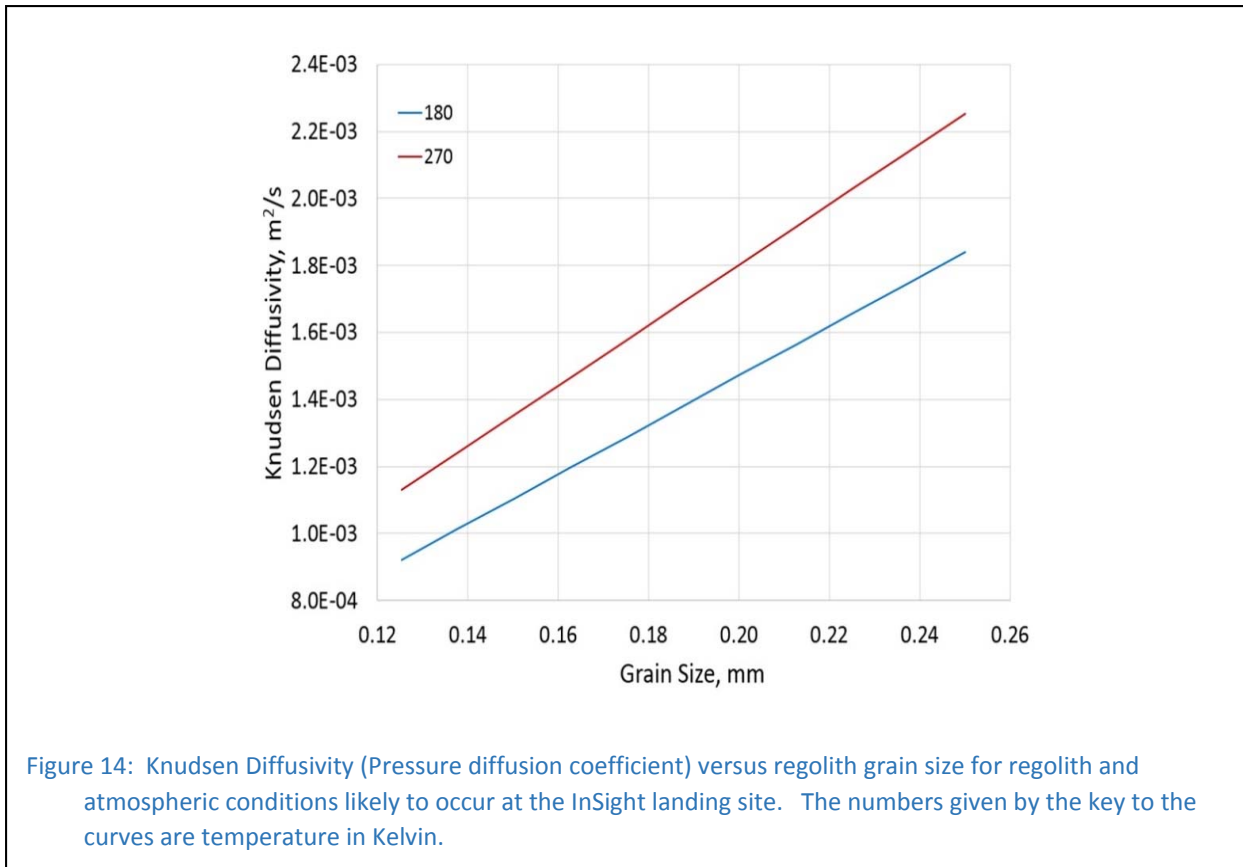
$$\lambda = \frac{RT}{\sqrt{2}\pi\gamma^2 N_a P} \quad (27)$$

1168 where  $R$  is the universal gas constant,  $T$  is absolute temperature,  $\gamma$  is the effective collisional diameter of  
1169 the molecules,  $N_a$  is the Avogadro number, and  $P$  is pressure. The effective collisional diameter of  $\text{CO}_2$  is  
1170 330 pm (*e.g.*, Albrecht et al., 2003), and at a temperature of 180 K and pressures of 6 and 8.5 hPa,  
1171 molecular mean free paths of 8.56 and 6.04  $\mu\text{m}$  were calculated for  $\text{CO}_2$ . At a temperature of 270 K and  
1172 pressures of 6 and 8.5 hPa, molecular mean free paths of 12.8 and 9.06  $\mu\text{m}$  were calculated. This array of  
1173 conditions and calculated molecular mean free paths should cover the range of likely diffusivity  
1174 environments to be encountered at the InSight landing site.

### 1175 **5.4. Calculated Range of Mass Diffusivity at Landing Site**

1176 Knudsen numbers were calculated using the molecular mean free paths calculated with equation 27  
1177 for the range of pore diameters estimated above, and corresponding Knudsen diffusion coefficients were  
1178 calculated using equation 27. These results indicate that gas flow in the shallow regolith at the InSight  
1179 landing site will probably be in the Knudsen Transition Flow range with Knudsen diffusivities ranging from  
1180 of 1 to 2  $\times 10^{-3}$   $\text{m}^2/\text{s}$ . To give a direct comparison of Knudsen diffusivity with grain size when in the pore  
1181 and pressure range for which the Knudsen diffusivity equation is applicable, Knudsen diffusivity is plotted

1182 as a function of grain size in Figure 14 for the expected range of grain sizes for the near-surface regolith  
1183 at the InSight landing site.



### 1184 5.5. Comparison with Experimental Data

1185 Fanale et al. (1982a) built an experimental system to determine the mass diffusivity of a *Mars simulant*  
1186 *soil* (45% smectite, 45% finely-ground basalt, and 10% iron oxide) with a density of 1300 kg/m<sup>3</sup> at  
1187 temperatures of -40°C (233 K) and -70°C (203 K). Diffusivity was determined by measuring the rate of  
1188 penetration of a CO<sub>2</sub> pressure wave with a starting pressure of ~6 hPa and a pressure step of ~2 hPa. The  
1189 experimentally estimated diffusivities were 2.5 x 10<sup>-6</sup> and 1 x 10<sup>-6</sup> m<sup>2</sup>/s for temperatures of 233 and 203K,  
1190 respectively. Fanale et al. (1982a) did not give an estimate of the average pore diameter of their Mars  
1191 simulant soil, but presumably the pores were very small as 90% of the simulant was smectite and finely-  
1192 ground basalt. Their determined diffusivity range is three orders of magnitude smaller than the  
1193 diffusivities calculated above. The primary difference in the diffusivities determined experimentally and  
1194 the diffusivities calculated here may be explained by the smaller pore sizes in the experimental regolith  
1195 simulant.

1196 An additional phenomenon, discussed by Fanale et al. (1982b), is the adsorption of CO<sub>2</sub> onto the grains  
1197 of the regolith. The adsorption of gases, including CO<sub>2</sub>, onto the surface of clays had been previously  
1198 reported (*e.g.*, Aylmore et al., 1970; Fanale and Cannon, 1979). The adsorption of molecules onto grain  
1199 surface tends to decrease pore diameters but does not reduce slip flow as molecules can slip over  
1200 molecules adsorbed onto grains. CO<sub>2</sub> molecules are less than 0.001 μm in their longest dimension which  
1201 much smaller than the pore sizes discussed above (9.4 to 18.8 μm). Thus, even if several layers of CO<sub>2</sub>  
1202 molecules adhere to the pore walls the reduction in pore size would be small. The effect would be to  
1203 increase the Knudsen number, but it would be unlikely to move out of the transition flow mode, with a  
1204 small accompanying decrease in mass diffusivity. These effects are likely to be very minor: a 0.01μm (10-  
1205 20 layers of CO<sub>2</sub> molecules) reduction in the minimum pore size (9.4 μm) would result in a 0.11% increase  
1206 in the Knudsen number and a 0.11% reduction in the Knudsen diffusivity. Adsorption of CO<sub>2</sub> could also  
1207 impact the mass diffusivity by acting as a temporary reservoir for CO<sub>2</sub>, storing CO<sub>2</sub> by adsorption during  
1208 pressure increases and releasing the adsorbed CO<sub>2</sub> during pressure decreases. This effect could result in  
1209 a hysteresis in atmospheric breathing that could be complicated by the temperature sensitivity of  
1210 adsorption.

## 1211 **5.6. Final Observations**

1212 Mass diffusivity is an important parameter to the InSight mission because it constrains the flow of the  
1213 Mars atmosphere into and out of the regolith at the landing site in response to changes in atmospheric  
1214 pressure. This is a well-known phenomenon on Earth. Although the pumping process is similar on Mars  
1215 to Earth, the molecular processes controlling mass diffusivity are different as a consequence of the low  
1216 pressure of the Mars atmosphere: on Earth gas molecular collisions are dominantly with neighboring gas  
1217 molecules; on Mars gas molecular interactions are dominantly with regolith grain surfaces. Using a  
1218 calculated range of pore sizes based on the assumption of uniform-size, spherical grains at the landing  
1219 site, a range of mass diffusivities of 1 to 2 x 10<sup>-3</sup> m<sup>2</sup>/s was calculated. This is probably a high estimate as  
1220 grains of variable size and non-spherical grains would generally result in smaller pores than uniform-size  
1221 spherical grains. The calculated diffusivity range based on simplified grain geometry is significantly higher  
1222 than an experimentally determined range of mass diffusivities for the Mars regolith of 1 x 10<sup>-6</sup> to 2.5 x 10<sup>-6</sup>  
1223 m<sup>2</sup>/s (Fanale et al., 1982a). A probably explanation for the difference between the calculated and  
1224 experimentally determined diffusivity ranges is that the regolith simulant used by Fanale et al. (1982a) in  
1225 their diffusivity determination was very fine grained. The inclusion of 45% smectite, a clay, in their sample  
1226 suggests that at least part of their sample had a grain size in the range of ~0.1 to 0.4 μm. Assuming the

1227 same pore size to grain size as used above, a range of Knudsen numbers equivalent to the curves in Figure  
1228 14 of 20 to 43 was calculated corresponding to Knudsen diffusivity range of  $1.0$  to  $2.6 \times 10^{-5} \text{ m}^2/\text{s}$  for 203  
1229 K and  $1.1$  to  $2.6 \times 10^{-5} \text{ m}^2/\text{s}$  for 233 K. These results are about an order of magnitude lower than the  
1230 diffusivities estimated experimentally, the differences probably being caused by the assumption of  
1231 uniform spherical grains in the pore size approximation for the calculations: clays have platy grains and  
1232 the average pore sizes in the experimental mixture were likely to be smaller than assumed here resulting  
1233 in a lower experimental diffusivity. However, a grain size range of  $0.125$  to  $0.25 \text{ mm}$  and the calculated  
1234 effective mass diffusivity with this grain-size range is thought to be more representative of the InSight  
1235 landing site.

1236 What are the implications of the calculated mass diffusivities for the penetration of periodic  
1237 atmospheric pressure waves into the regolith at the landing site? If we make the assumption that the  
1238 regolith is homogeneous and isotropic, a penetration skin depth  $\delta$  can be calculated as  $\delta =$   
1239  $\sqrt{(2\pi D_{eff}/\omega)}$ , where  $\omega$  is the angular frequency of the period wave. The skin depth is the depth at which  
1240 the maximum amplitude of the pressure change is  $1/e$  ( $\sim 37\%$ ) of the maximum surface pressure change.  
1241 For a wave with a period of 1 sol (24 hours 40 min),  $\delta = 9.4 \text{ m}$  for  $D_{eff} = 1.0 \times 10^{-3} \text{ m}^2/\text{s}$ , and  $\delta = 13.2 \text{ m}$  for  
1242  $D_{eff} = 2.0 \times 10^{-3} \text{ m}^2/\text{s}$ . For a wave with a period of Mars year (687 days),  $\delta = 244 \text{ m}$  for  $D_{eff} = 1.0 \times 10^{-3} \text{ m}^2/\text{s}$ ,  
1243 and  $\delta = 345 \text{ m}$  for  $D_{eff} = 2.0 \times 10^{-3} \text{ m}^2/\text{s}$ . These are large depths relative to the maximum penetration of  
1244 the HP<sup>3</sup> probe of  $5 \text{ m}$ . The time for a diffusive disturbance to travel a characteristic length  $L_c$  of  $5 \text{ m}$  is  
1245 about  $0.29 \text{ sol}$  for a diffusivity of  $1.0 \times 10^{-3} \text{ m}^2/\text{s}$ , and about  $0.14 \text{ sol}$  for a diffusivity of  $2.0 \times 10^{-3} \text{ m}^2/\text{s}$  (using  
1246 the approximation  $L_c^2 = D_{eff} t$ , where  $t$  is time). However, the effect of flow of atmospheric gases in and  
1247 out of the regolith in terms of heat transport and the HP<sup>3</sup> heat-flow determination depends on the relative  
1248 efficiencies of convective gas heat transport and conductive heat transport (possibly aided by  
1249 intergranular radiative heat transport. This problem has been examined by Morgan et al. (2017). Their  
1250 highest estimate of mass diffusivity was an order of magnitude lower than we have concluded here for  
1251 the regolith at the InSight landing site, but they concluded that the diffusivity would need to be higher by  
1252 a factor of about 100 for convection to be more efficient than conduction with reasonable estimates of  
1253 the thermal conductivity of the regolith. This conclusion is based on several estimated parameters, but  
1254 current information indicates that atmospheric gases will be forced into the regolith by changes in  
1255 atmospheric pressure, but thermal convection by these movements will be insignificant.

1256

## 1257 **6. Summary and Conclusions**

1258 There were a number of primary engineering criteria for the InSight landing site which to some extent  
1259 affected the physical properties of the landing site. These criteria included latitude (equatorial for solar  
1260 power), low elevation (avoid cold temperatures), smooth plains with few rocks and craters (safe landing  
1261 site), and fragmented regolith (to be penetrated by the self-hammering, heat-flow probe – HP<sup>3</sup>). These  
1262 criteria resulted in the selection of a 130 x 27 km landing ellipse at 4.5°N, 135.9°E in western Elysium  
1263 Planitia on Hesperian plains in the southernmost lowlands.

1264 Thermophysical properties used in the site-selection process indicated a regolith at this site similar to  
1265 weakly-bonded terrestrial soils, capable of being penetrated by the HP<sup>3</sup> probe. The properties indicated  
1266 that the soil was cohesionless sand or low cohesion soil with a bulk density of ~1,000 to 1,600 kg m<sup>-3</sup> and  
1267 grain sizes of ~0.15 -0.25 mm (fine sand). A cover of surficial dust was indicated, less than 1-2 mm thick,  
1268 and with low rock abundance. The upper 5 m of the regolith were predicted to be composed of nearly  
1269 cohesionless, fine, well-sorted, rounded to sub-rounded, basaltic sand, which included few rocks.

1270 Based on studies of terrestrial soils and from heat-flow observations on the Moon, the regolith density  
1271 is likely to significantly increase with depth as a result of compaction. The lunar heat-flow results required  
1272 a rapid increase in thermal conductivity associated with compaction with depth. Compaction caused by  
1273 gravity and impacts have resulted in models based on lunar compaction but the models are uncalibrated  
1274 for Mars.

1275 Information covering cohesion of the Mars Regolith at the InSight landing site has been compiled from  
1276 mechanical arms from Mars landers and the wheels of rovers. Cohesions range from cohesionless to  
1277 weakly cohesive soils, less than 4 kPa, with blocky soils having higher cohesions of 3-11 kPa. The landing  
1278 site will probably have a thin layer of cohesionless to weakly cohesive eolian deposits at the surface. These  
1279 deposits may be blown away by the pulsed jets of the lander, below which the regolith will be weakly  
1280 cohesive.

1281 Internal friction angle is sensitive to factors including material grain shape and bulk density. Many  
1282 Mars regolith simulants have had angular grains that are probably not representative of the rounded to  
1283 sub-rounded grains subject to wind erosion at the landing site. Extrapolation of experiments with  
1284 rounded grains and a bulk density of 1,300 kg/m<sup>3</sup> have provided a friction angle of 28° to 30° for the

1285 landing site. If the assumption is made that particle shape does not change with depth, internal friction  
1286 angle may be predicted as a function of bulk density and depth.

1287 Grain size is an important factor in many physical properties and is primarily constrained to be in the  
1288 range of 150-250  $\mu\text{m}$  (fine sand) by the thermal inertia of the landing site. Theoretical studies and  
1289 observations at the Phoenix landing site in the Martian Arctic indicate that there is a transition below 600  
1290  $\mu\text{m}$  from larger clasts to the dominant fine sand grain size. Finer material may be found in this surficial  
1291 dust layer.

1292 At this stage, thermophysics properties have been assumed to change only with depth. Measurements  
1293 of surface emissivity on Mars has been from satellite sensors and from a sensor on the Mars Science  
1294 Laboratory rover. These data have allowed weighted average emissivities to be derived for the three  
1295 wavelength bands corresponding to the HP<sup>3</sup> radiometer filters at 235 K for four different types of soils  
1296 measured *in situ* by the Mars Exploration Rovers' mini-thermal emission spectrometer instruments.

1297 Surface thermal inertia controls the rate of change in temperature of the upper 2-30 cm of the regolith,  
1298 and is strongly related to the square root of thermal conductivity. The lowest thermal inertias in the  
1299 landing region are typically observed where atmospheric dust and very fine sand are trapped; the highest  
1300 thermal inertias are associated with coarse regolith on crater rims and ejecta blankets.

1301 Surface albedo from different areas of Mars has been measured at different resolutions from orbiting  
1302 satellite systems. Landers with retropropulsive thrusters have changed the surface albedo by temporarily  
1303 removing the surface dust layer at all landing sites where the thrusters have been used. A temporary  
1304 albedo reduction of ~20-50% at the InSight landing site during landing is anticipated.

1305 Based on in situ determinations of the thermal conductivity of the lunar regolith during two of the  
1306 Apollo missions, and a number of published experiments simulating lunar and Mars regolith conditions,  
1307 the thermal conductivity of the shallow regolith at the landing site is anticipated to be of the order of 0.01  
1308 W/(m K), about two orders of magnitude lower than the thermal conductivity of damp terrestrial soils. As  
1309 bulk density changes with depth, thermal conductivity is anticipated to change with depth. In addition,  
1310 although atmospheric pressure is much lower, the fractional changes in atmospheric pressure during the  
1311 diurnal and annual cycles are much greater on Mars than on Earth. As heat transfer through the gas in  
1312 pore spaces is significant on Mars, the bulk thermal conductivity is sensitive to changes in atmospheric  
1313 pressure.

1314 Studies of the heat capacity (units J/K) or specific heat (units J/(kg K)) of lunar, geologic, and meteorite  
1315 materials at low temperatures indicate that these parameters are strongly temperature dependent,  
1316 increasing with increasing temperature. This temperature dependence is most significant in the near-  
1317 surface regolith layer where there are large temperature perturbations associated with diurnal and annual  
1318 temperature variations. Below a few tens of cm these perturbations decay and an average heat  
1319 capacity/specific heat may be used.

1320 Thermal diffusivity is the parameter in thermal conduction associated with the propagation of  
1321 temperature changes, such as transmission of the annual temperature variation into the regolith. As with  
1322 other thermal parameters, it is probably most variable in the upper few tens of cm of the regolith at the  
1323 landing site, and is fairly constant below this depth.

1324 Subsurface elastic properties are of particular importance to the data to be collected by the  
1325 seismometer experiment (SEIS) when operating at its highest rate and for short period surface waves  
1326 above 5 Hz. There are no remote sensing data or existing lander results from which these properties may  
1327 be derived and thus at present they are estimated from laboratory measurements. Seismic body wave  
1328 measurements indicate that seismic velocities are very slow within the regolith but a significant increase  
1329 in velocities may be expected between the surface and 5 m depth. In contrast, experiments on Mars  
1330 regolith simulants and similar materials indicate that Poisson's ratio will be relatively constant with depth  
1331 in dry, shallow regolith, but lower than most estimates for the Moon or measured in water-saturated  
1332 terrestrial soils. Young's Modulus increases rapidly with depth, similar to the body-wave velocities.  
1333 Seismic attenuation (dissipation of seismic energy by non-elastic processes), as measured by the seismic  
1334 quality factor,  $Q$ , is expected to be relatively high in the Mars regolith, but depends to a large extent on  
1335 the presence of adsorbed water, a parameter for which there are no direct observations at the InSight  
1336 landing site.  $Q$  was measured to be very high, both in the regolith and at depth, on the Moon relative to  
1337 terrestrial values, reflecting the very dry state of the Moon. A very small amount of water, monolayers in  
1338 thickness, on the grains in the Mars regolith could be sufficient to significantly reduce  $Q$  by an order of  
1339 magnitude, however. If no water is present  $Q$  would be close to lunar values.

1340 Mass diffusivity of the landing site regolith is the parameter that relates the flow of the Mars  
1341 atmosphere in and out of the regolith in response to changes in surface atmospheric pressure. Most  
1342 landing site physical parameters change from Earth to the Mars regolith because of differences in water  
1343 saturation, atmospheric pressure, compaction, composition, etc. Mass diffusivity changes from Earth to

1344 Mars, except in a few special terrestrial examples, in that the mode of gas transport is dominated by  
1345 molecule-grain collisions in the landing site regolith and a mass diffusivity equation appropriate to this  
1346 mode (Knudsen diffusivity) must be used. The results of one experiment to measure mass diffusivity have  
1347 been published, but the grain size of the material used in this experiment was much smaller than is  
1348 thought to apply to the landing site. However, when the grain size and shape are included in estimation  
1349 of the pore size, the calculated Knudsen diffusivity is close to the experimental results. The effective mass  
1350 diffusivity calculated for the landing site is three orders of magnitude larger than the experimental results,  
1351 but consistent with different grain size and shape.

1352 Physical properties of the regolith at the InSight landing site presented here are all speculative. Some  
1353 of the properties are based on circular reasoning because they are based on data that were used to select  
1354 the landing site, such as surface thermophysical properties. However, even these properties are  
1355 ultimately based on correlations of remote sensing properties (satellite or rover) with ground truth data.  
1356 Many of the properties are based on extensive experimental data with carefully refined models for the  
1357 Mars regolith. However, with the exception of a shallow trench dug by the Phoenix lander in the southern  
1358 polar region, and extrapolations from limited cliff exposures, there are no direct stratigraphic data  
1359 describing the Mars regolith. We will gain much of these data during the penetration of the HP<sup>3</sup> probe  
1360 and from the data collected during the InSight mission.

1361

## 1362 **7. References**

- 1363 R. K. Agarwal, Y. Keon-Young, R. Balakrishnan, *Phys. Fluids* 13, 3061 (2001)
- 1364 E. Albrecht, G. Baum, T. Bellunato, A. Bressan, S. Dalla Torre, C. D'Ambrosio, M. Davenport, M.  
1365 Dragicevic, S. Duarte Pinto, P. Fauland, S. Ilie, G. Lenzen, P. Pagano, D. Piedigrossi, F. Tessarotto,  
1366 and O. Ullaland, *Nuclear Inst. and Methods in Res. A* 510, 262 (2003)
- 1367 K. A. Alshibli, A. Hasan, *J. Geotech. Environ. Eng.* 135, 673 (2009)
- 1368 V. Ansan, V., T. Dezert (and the DLR group), InSight Science Team Presentation, Zurich, Switzerland,  
1369 September 5–9, 2015, and written communication (2015)
- 1370 R. E. Arvidson, P. Bellutta, F. Caley, A. A. Fraeman, J. B. Garvin, O. Gasnault, J. A. Grant, J. P.  
1371 Grotzinger, V. E. Hamilton, M. Heverly, K. A. Lagnemma, J. R. Johnson, N. Lanza, S. Le Mouélic, N.  
1372 Mangold, D. W. Ming, M. Hehta, R. V. Morris, H. E. Newsom, N. Rennó, D. Rubin, J. Schieber, R.

1373 Sletten, N. T. Stein, F. Thuillier, A. R. Vasavada, J. Vizcaino, R. C. Wiens, J. Geophys. Res. Planets,  
1374 119, 1322 (2014) doi:10.1002/2013JE004605

1375 D. Assimaki, W. Li, J. H. Steidl, K. Tsuda, Bull. Seism. Soc. Am. 98, 301 (2008) doi: 10.1785/0120070030

1376 L. A. Aylmore, G., I. D. Sills, J. P. Quirk, Clay and Clay Minerals 18, 91 (1970)

1377 R. Bachrach, J. Dvorkin, A. Nur, Geophysics 63, 1234 (1998)

1378 R. Bachrach, J. Dvorkin, A. Nur, Geophysics 65, 559 (2000)

1379 W. B. Banerdt, S. Smrekar, K. Hurst, P. Lognonné, T. Spohn, S. Asmar, D. Banfield, L. Boschi, U.  
1380 Christensen, V. Dehant, W. Folkner, D. Giardini, W. Goetz, M. Golombek, M. Grott, T. Hudson, C.  
1381 Johnson, G. Kargl, N. Kobayashi, J. Maki, D. Mimoun, A. Mocquet, P. Morgan, M. Panning, W. T.  
1382 Pike, J. Tromp, T. vanZoest, R. Weber, M. Wiezorek, and the InSight Team, 44th Lunar and Planetary  
1383 Science Conference (Lunar and Planetary Institute, Houston, Abstract #1915, 2013)

1384 Becker A., C. Vrettos C., 5<sup>th</sup> ASCE International Conference on Engineering, Construction, and Operations  
1385 in Challenging Environments. Earth and Space 2016, 9 (2016)

1386 M. D. Bolton, Géotechnique 36, 65 (1986)

1387 J. E.. Bowles, Foundation analysis and design (McGraw-Hill, New York, 1996)

1388 Th. Brunet, X. Jia, P. Mills, Phys. Rev. Lett. 101, 138001 (2008) doi: 10.1103/PhysRevLett.101.138001

1389 W. D. Carrier, Earth Moon Planets 10, 183 (1974) doi:10.1007/BF00655719.

1390 W. D. Carrier, J. K. Mitchell, A. Mahmood, Proc. Lunar Sci. Conf., 4th, 4, 118 (Lunar and Planetary  
1391 Institute, Houston, 1973)

1392 D. C. Catling, C. B. Leovy, S. E. Wood, M. D. Day, 42nd Lunar and Planetary Science Conference (Lunar  
1393 and Planetary Institute, Houston, Abstract #2529, 2011)

1394 D. C. Catling, C. B. Leovy, S. E. Wood, M. D. Day, Third Conference on Early Mars (Lunar and Planetary  
1395 Institute, Houston, Abstract #7031, 2012)

1396 C. Charalambous, On the evolution of particle fragmentation with applications to planetary surfaces  
1397 (Doctoral dissertation/thesis, Imperial College London, 2014/2015).

1398 C. Charalambous, W.T. Pike, AGU Fall Meeting Abstracts, # P23B-3986 (2014)

1399 C. Charalambous, W.T. Pike, W. Goetz, M.H. Hecht, U. Staufer, AGU Fall Meeting Abstracts, # P43B-  
1400 1669 (2011)

1401 P. R. Christensen, Icarus 68, 217 (1986)

1402 P. R. Christensen, H.J. Moore, in MARS, ed. By H.H. Kieffer, B.M. Jakosky, C.W. Snyder, M.S. Matthews  
1403 (University of Arizona Press, Tucson, 1992), p. 686

1404 P. R. Christensen, D.L. Anderson, S.C. Chase, R.N. Clark, H.H. Kieffer, M.C. Malin, J.C. Pearl, J. Carpenter,  
1405 N. Bandiera, F.G. Brown, S. Silverman, J. Geophys. Res 97, 7719 (1992)

1406 P. R. Christensen, J.L. Bandfield, V.E. Hamilton, S.W. Ruff, H.H. Kieffer, T.N. Titus, M.C. Malin, R.V.  
1407 Morris, M.D. Lane, R.L. Clark, B.M. Jakosky, M.T. Mellon, J.C. Pearl, B.J. Conrath, M.D. Smith, R.T.  
1408 Clancy, R.O. Kuzmin, T. Roush, G.L. Mehall, N. Gorelick, K. Bender, S. Dason, E. Greene, S. Silverman,  
1409 M. Greenfield, J. Geophys. Res. 106, 23823 (2001)

1410 P. R. Christensen, P. R., J. L. Bandfield, J. F. Bell III, N. Gorelick, V. E. Hamilton, A. Ivanov, B. M.  
1411 Jakosky, H. H. Kieffer, M. D. Lane, M. C. Malin, T. McConnochie, A. S. McEwen, H. Y. McSween  
1412 Jr., G. L. Mehall, J. E. Moersch, K. H. Nealson, J. W., Rice Jr., M. I. Richardson, S. W. Ruff, M. D.  
1413 Smith, T. N. Titus, M. B. Wyatt, Science 300, 2056 (2003a)

1414 P. R. Christensen, G. L. Mehall, S. H. Silverman, S. Anwar, G. Cannon, N. Gorelick, R. Kheen, T.  
1415 Tourville, D. Bates, S. Ferry, T. Fortuna, J. Jeffryes, W. O'Donnell, R. Peralta, T. Wolverton, D. Blaney,  
1416 R. Denise, J. Rademacher, R. V. Morris, S. Squyres, J. Geophys. Res. 108 (2003b)  
1417 doi:10.1029/2003JE002117

1418 P. R. Christensen, S. W. Ruff, R. L. Fergason, A. T. Knudson, S. Anwar, R. E. Arvidson, J. L. Bandfield,  
1419 D. L. Blaney, C. Budney, W. M. Calvin, T. D. Glotch, M. P. Golombek, N. Gorelick, T. G. Graff, V.  
1420 E. Hamilton, A. Hayes, J. R. Johnson, H. Y. McSween Jr., G. L. Mehall, L. K. Mehall, J. E. Moersch,  
1421 R. V. Morris, A. D. Rogers, M. D. Smith, S. W. Squyres, M. J. Wolff, M. B. Wyall, Science 305, 837  
1422 (2004a)

1423 P. R. Christensen, M. B. Wyatt, T. D. Glotch, A. D. Rogers, S. Anwar, R. E. Arvidson, J. L. Bandfield,  
1424 D. L. Blaney, C. Budney, W. M. Calvin, A. Fallacaro, R. L. Fergason, N. Gorelick, T. G. Graff, V. E.  
1425 Hamilton, A. G., Hayes, J. R. Johnson, A. T. Knudson, H. Y. McSween Jr., G. L. Mehall, L. K. Mehall,  
1426 J. E. Moersch, R. V. Morris, M. D. Smith, S. W. Squyres, S. W. Ruff, M. J. Wolff, Science 306, 1733  
1427 (2004b)

1428 P. R. Christensen, P. R., B.M. Jakosky, H.H. Kieffer, M.C. Malin, H.Y. McSween Jr., K. Nealson, G.L.  
1429 Mehall, S.H. Silverman, S. Ferry, M. Caplinger, M. Ravine, Space Sci. Rev. 110, 85 (2004c)

1430 F. Civan, F., Trans. Porous. Media 82, 375 (2010)

1431 J. E. Conel, J. Geophys. Res. 74,1614 (1969)

1432 G. J. Consolmagno, M. W. Schaefer, B. E. Schaefer, D. T. Britt, R. J. Macke, M. C. Nolan, E. S. Howell,  
1433 Planetary and Space Science 87, 146 (2013)

1434 M. R. Cooper, R.L. Kovach, J. S. Watkins, Rev. Geophys. Space Phys. 12, 291 (1974)

1435 A. M. Dainty, N. M. Toksöz, Phys. Earth Planet. Int. 26, 250 (1981)

- 1436 G. Dal Moro, *Icarus* 254, 338 (2015) doi:10.1016/j.icarus.2015.03.017
- 1437 I. J. Daubar, A. S. McEwen, M. P. Golombek, 46th Lunar and Planetary Science Conference (Lunar and  
1438 Planetary Institute, Houston, Abstract #2225, 2015)
- 1439 P. Delage, F. Karakostas, A. Dhemaied, M. Belmokhtar, P. Lognonné, M. Golombek, E. De Laure, J.-C.  
1440 Dupla, S. Kedar, Y.J. Cui, B. Banerdt, *Space Sci. Rev.* ( 2017) doi:10.1007/s11214-017-033907.
- 1441 S. A. Denekamp, Y. Tsur-Lavie, *Journal of Geotechnical and Geoenvironmental Engineering* 107, 439  
1442 (1981)
- 1443 F. P. Fanale, W. A. Canon, *J. Geophys. Res.* 84, 8404 (1979)
- 1444 F. P. Fanale, W. B. Banerdt, R. S. Saunders, L. A. Johansen, J. R. Salvail, *J. Geophys. Res.* 87, 10,215  
1445 (1982a)
- 1446 F. P. Fanale. J. R. Savail, W. B. Banerdt, R. S. Saunders, *Icarus* 50, 381 (1982b)
- 1447 L. Y. Faust, *Geophysics*, 16, 192 (1951)
- 1448 W. C. Feldman, F. H. Prettyman, S. Maurice, J. J. Plaut, D. L. Bish, D. T. Vaniman, M. T. Mellon, A.  
1449 E. Metzger, S. W. Squyres, S. Karunatillake, W. V. Bounton, R. C. Elphic, H. O. Funsten, D. J.  
1450 Lawrence, R. L. Tokar, *J. Geophys. Res.* 109, E09006, (2004) doi:10.1029/2003JE002160
- 1451 R. L. Fergason, P. R. Christensen, H. H. Kieffer, *J. Geophys. Res.* 111, E12004 (2006a)  
1452 doi:10.1029/2006JE002735
- 1453 R. L. Fergason, P. R. Christensen, J. F. Bell III, M. P. Golombek, K. E. Herkenhoff, H. H. Kieffer, *J.*  
1454 *Geophys. Res.* 111, E02S21 (2006b) doi:10.1029/2005JE002583
- 1455 R. L. Fergason, P. R. Christensen, M. P. Golombek, T. J. Parker, *Space Sci. Rev.* 170, 739 (2012)  
1456 doi:10.1007/s11214-012-9891-3
- 1457 C. N. Foley, T. Economou, R. N. Clayton, *J. Geophys. Res.* 108, 8096 (2003) doi:10.1029/2002JE002019
- 1458 V. Formisano, F. Angrilli, G. Arnold, S. Atreya, G. Bianchini, D. Biondi, A. Blanco, M. I. Blecka, A.  
1459 Coradini, L. Colangeli, A. Ekonomov, F. Esposito, S. Fonti, M. Giuranna, D. Grassi, V. Gnedykh, A.  
1460 Grigoriev, G. Hansen, H. Hirsh, I. Khatuntsev, A. Kiselev, N. Ignatiev, A. Jurewicz, E. Lellouch, J.  
1461 Lopez Moreno, A. Marten, A. Mattana, A. Maturilli, M. Michalska, V. Moroz, B. Moshkin, F. Nespoli,  
1462 Y. Nikolsky, R. Orfei, P. Orleanski, V. Orleanski, V. Orofino, E. Palomba, D. Patsaev, G. Piccioni, M.  
1463 Rataj, R. Rodrigo, J. Rodriguez, M. Rossi, B. Saggin, D. Titov, L. Zasova, *Planet. Space Sci.* 53, 963  
1464 (2005) doi:10.1016/j.pss.2004.12.006
- 1465 J. Fortin, S. Stanchits, S. Vinciguerra, Y. Guéguen, *Tectonophysics*, 503, 60 (2011)  
1466 doi:10.1016/j.tecto.2010.09.028
- 1467 J. A., Fountain, E. A. West, *J. Geophys. Res.* 75, 4063 (1970)

1468 N. Fujii, M. Osako, *Earth Planet. Sci. Lett.* 18, 65 (1973) doi:10.1016/0012-821X(73)90035-6

1469 R. Fukushima, H. Nakahara, T. Nishimura, *Bull. Seismol. Soc. Am.* 106, 552 (2016)

1470 doi:10.1785/0120150059

1471 A. F. Gangi, T. E. Yen, *Moon and Planets*, 20, 439 (1979)

1472 J. F. Gibbs, D. M. Boore, W. B. Joyner, T. E. Fernal, *Bull. Seism. Soc. Am.* 84, 76 (1994)

1473 K. L. Gillet, M. Margerin, M. Calvet, M. Monnereau, *Phys. Earth. Planet. Int.* 262, 28 (2017)

1474 doi:10.1016/j.pepi.2016.11.001

1475 M. P. Golombek and the Mars Pathfinder Science Team, *J. Geophys. Res.* 104, 8523 (1999)

1476 M. P. Golombek, R.J. Phillips, in *Planetary Tectonics*, ed. by T.R. Watters, R.A. Schultz (Cambridge

1477 University Press, Cambridge, Chap. 5, p. 183, 2010)

1478 M. P. Golombek, R.A. Cook, H.J. Moore, T.J. Parker, *J. Geophys. Res.* 102, 3967 (1997)

1479 M. P. Golombek, R. E. Arvidson, J. F. Bell III, P. R. Christensen, J. A. Crisp, L. S. Crumpler, B. L.

1480 Ehlmann, R. L. Fergason, J. A. Grant, R. Greeley, A. F. C. Haldermann, D. M. Kass, T. J. Parker, J.

1481 T. Schofield, S. W. Squyres, R. W. Zurek, Assessment of Mars Exploration Rover landing site

1482 predictions. *Nature* 436, 44 (2005) doi:10.1038/nature03600

1483 M. P. Golombek, L. S. Crumpler, J. A. Grant, R. Greeley, N. A. Cabrol, T. J. Parker, J. W. Rice Jr., J. G.

1484 Ward, R. E. Arvidson, J. E. Moersch, R. L. Fergason, P. R. Christensen, A. Castaño, R. Castaño, A.

1485 F. C. Haldermann, R. Li, J. F. Bell III, S. W. Squyres, *J. Geophys. Res.* 110, E02S07 (2006)

1486 doi:10.1029/2005JE002503

1487 M. P. Golombek, A. F. C. Haldemann, R. A. Simpson, R. L. Fergason, N. E. Putzig, R. E. Arvidson, J.

1488 F. Bell III, M. T. Mellon, in *The Martian Surface: Composition, Mineralogy and Physical Properties*, ed.

1489 by J. F. Bell III (Cambridge University Press, Cambridge, Chap. 21, pp. 468, 2008a)

1490 M. P. Golombek, A Huertas, J. Marlow, B. McGrane, C Klein, M Martinez, R. E. Arvidson, T. Heet, L.

1491 Barry, K. Seelos, D. Adams, W. Li, J. R. Matijevic, T. Parker, H. G. Sizemore, M. Mellon, A. S.

1492 McEwen, L. K. Tamppari, Y. Cheng, *J. Geophys. Res.* 113, E00A09 (2008b) doi:10.1029/2007JE003065

1493 M. P. Golombek, A. Huertas, D. Kipp, F. Calef, *Mars* 7, 1 (2012) doi:10.1555/mars.2012.0001

1494 M. P. Golombek, N. Warner, C. Schwartz, J. Green, 2013, 44th Lunar and Planetary Science Conference

1495 (Lunar and Planetary Institute, Houston, Abstract #1696, 2013b)

1496 M. P. Golombek, D. Kipp, N. Warner, I. J. Daubar, R. Ferguson, R. Kirk, R. Beyer, A. Huertas, S. Piqueux,

1497 N. Putzig, B. A. Campbell, G. A. Morgan, C. Charalambous, T. Pike, K. Gwinner, F. Calef, J. Ashley,

1498 D. Kass, M. Mischna, C. Bloom, N. Wigton, C. Schwartz, H. Gengl, L. Remond, J. Sweeney, E.

1499 Sklyanskiy, M. Lisano, J. Benardino, S. Smrekar, and B. Banerdt, *Space Sci. Rev.* 211, 5 (2017)  
1500 doi:10.1007/s11214-016-0321-9.

1501 J. Gomez-Elvira, C. Armiens, L. Castañer, M. Domínguez, M. Genzer, F. Gómez, R. Haberle, A.-M. Harri,  
1502 V. Jiménez, H. Kahanpää, L. Kowalski, A. Lepinette, J. Martin, J. Martínez-Frías, I McEwan, L. Mora,  
1503 J. Moreno, S. Navarro, M. A. de Pablo, A. Peña, J. Polkko, M. Ramos, N. O. Renno, J. Ricart, M.  
1504 Richardson, J. Rodríguez-Manfredi, J. Romeral, E. Sebastián, J. Serrano, M. de la Torre Juárez, J.  
1505 Torrez, F. Torrero, R. Urquí, L. Vázquez, T. Velasco, J. Verdasca, M.-P. Zorzano, J. Martin-Torres,  
1506 *Space Sci. Rev* 170, 583 (2012)

1507 S. Griffiths, A. Rescaglio, C. Krause, *Ultrasonics*, 50, 139 (2010) doi:10.1016/j.ultra.2009.09.034

1508 M. Grott, J. Helbert, R. Nadalini *J. Geophys. Res.*, 112, E09004 (2007) doi:10.1029/2007JE002905.

1509 B. Gundlach, J. Blum, *Icarus* 223, 479 (2013)

1510 V. E. Hamilton, A. R. Vasavada, E. Sebastián, M. de la Torre Juárez, M. Ramos, C. Armiens, R. E.  
1511 Arvidson, I. Carrasco, P. R. Christensen, M. A. de Pablo, W. Goetz, J. Gómez-Elvira, M. T. Lemmon,  
1512 M. B. Madsen, F. Javier Martin-Torres, J. Martínez-Frías, A. Molina, M. C. Palucis, S. C. R. Rafkin,  
1513 M. I. Richardson, R. A. Yingst, M.-P. Zorzano, *J. Geophys. Res.* 119, 745 (2014)  
1514 doi:10.1002/2013JE004520.

1515 W. K. Hartmann, J. Anguita, M. de la Casa, D. Berman, E.V. Ryan, *Icarus* 149, 37 (2001)

1516 L. A. Haskin, A. Wang, B. L. Jolliff, H. Y. McSween, B. C. Clark, D. J. Des Marais, S. M. McLennan, N.  
1517 J. Tosca, J. A. Hurowitz, J. D. Farmer, A. Yen, S. W. Squyres, R. E. Arvidson, G. Klingelhöfer, C.  
1518 Schröder, P. A. De Souza Jr., D. W. Ming, R. Gellert, J. Zipfel, J. Brückner, J. F. Bell III, K Herkenhoff,  
1519 P. R. Christensen, S. Ruff, D. Blaney, S. Gorevan, N. A. Cabrol, L. Crumpler, J. Grant, L. Soderblom,  
1520 *Nature* 436, 66 (2005).

1521 G. Heiken, D. Vaniman, B. French, eds., *Lunar Sourcebook* (Cambridge Univ. Press, Cambridge, U. K.,  
1522 1991)

1523 B. S. Hemingway, R. A. Robie, W. H. Wilson, *Proceedings of the Lunar Science Conference* 4, 2481  
1524 (1973)

1525 K. E. Herkenhoff, M. P. Golombek, E. A. Guinness, J. B. Johnson, A. Kusack, L. Richter, R. J. Sullivan,  
1526 S. Gorevan, in: J.Bell, ed., *The Martian Surface* (Cambridge University Press, Cambridge, UK, 2008)

1527 H. Hertz, *Gesammelte Werke* (v. 1, p. 155, Leipzig, 1895)

1528 S. L. Hess, R. M. Henry, J. E. Tillman (1979), *J. Geophys. Res.* 84, 2923 (1979)  
1529 doi:10.1029/JB084iB06p02923.

1530 P. G., Horvath, V. Latham, Y. Nakamura, H. J. Dorman, *J. Geophys. Res.*, 85, 6572 (1979)

1531 D. G. Huizenga, D. M. Smith, Am. Inst. Chem. Eng (AIChE) J. 32, 1 (1986)

1532 J. A. Hurowitz, S. M. McLennan, N. J. Tosca, R. E. Arvidson, J. R. Michalski, D. W. Ming, C. Schröder,  
1533 S. W. Squyres, J. Geophys. Res. 111, E02S19 (2006).

1534 E. S. Hütter, N. I. Koemle, G. Kargl, E. Kaufmann, J. Geophys. Res. 113, E12004 (2008)  
1535 doi:10.1029/2008JE003085

1536 M. B. Jaksa, K. S. Yeong, K. T. Wong, S. L. Lee, Proc. 9th Australia New Zealand Conference on  
1537 Geomechanics (Auckland, New Zealand, p. 289-294, 2004)

1538 J. Jaky, J. Soc. Hung. Eng. Arch. (Magyar Mernok es Epitesz-Egylet Kozlonye, in Hungarian, p. 355 1944)

1539 F. Javadpour, D. Fisher, M. Unsworth, J. Canadian Petrol. Tech. 46 55 (2007)

1540 D. M. Johnson, A. L. Frisillo, J. Dorman, G. V. Latham, D. Strangway, J. Geophys. Res. 87, 1899 (1982)

1541 B. W. Jones, Proceedings Third Lunar Sci. Conf. p. 2545 (1972)

1542 D. Jongmans, Eng. Geology 29, 99 (1990)

1543 M. G. Kaganer, J. Eng. Phys. 11, 19 (1966)

1544 G. Karnidakis, A. Beskok, N. Aluru, 2005, Microflows and Nanoflows: Fundamentals and Simulation,  
1545 (Springer, New York. 2005)

1546 M. Kaviany, Principles of Convective Heat transfer (Springer, 2<sup>nd</sup> edn. 2001)

1547 S. J. Keihm , K Peters, M. G. Langseth Jr., J. L. Chute Jr., Earth Planet. Sci. Lett. 19, 337 (1973)

1548 S. J. Keihm and Langseth Jr., Proceed. 4<sup>th</sup> Lunar Sci. Conf. 3, 2503 (1973)

1549 S. J. Keihm, M. G. Langseth Jr., Icarus 24, 211 (1975)

1550 H. H. Kieffer, J. Geophys. Res. Planets 118, 451 (2013)

1551 H. H. Kieffer, T. Z. Martin, A. R. Peterfreund, B. M. Jakosky, E. D. Miner, F. D. Palluconi, J. Geophys.  
1552 Res. 82, 4249 (1977)

1553 S. Kinoshita, Bull. Seism. Soc. Am. 98, 463 (2008) doi:10.1785/0120070070

1554 L. J. Klinkenberg, API Drilling and Production Practices (New York, p. 200, 1941)

1555 B. Knapmeyer-Endrun, M.P. Golombek, M. Ohrnberger, Space Sci Rev., doi: 10.1007/s11214-016-0300-  
1556 1

1557 J. F. Kok, E. J. Parteli, T. I. Michaels, D. B. Karam, 2012, Reports on Progress in Physics, 106901 (2012)

1558 R. L. Kovach, J. S. Watkins, Lunar Planet. Sci. Conf. 3, 461 (1972)

1559 R. L. Kovach, J.S. Watkins, Moon, 7, 63 (1973)

1560 M. G. Langseth Jr, S. J. Keihm, K. Peters, Proc. 7th Lunar Sci. Conf. (Lunar and Planet. Inst. Houston, p.  
1561 3143, 1976)

1562 E. Larose, A. Khan, Y. Nakamura, M. Campillo, *Geophys. Res. Lett.*, 32, L16201 (2005)  
1563 doi:10.1029/2005GL023518

1564 G. V. Latham, M. Ewing, F. Press, G. Sutton, J. Dorman, Y. Nakamura, N. Toksöz, R. Wiggins, J. Derr,  
1565 F. Duennebier, *Passive seismic experiment. Science* 167, 445 (1970a)

1566 G. V. Latham, M. Ewing, J. Dorman, F. Press, N. Toksöz, G. Sutton, R. Meissner, F. Duennebier, Y  
1567 Nakamura, R. Kovach, M. Yates, 170, 620 (1970b)

1568 T. Lay, T. C. Wallace, in *Modern Global Seismology* (Academic Press, San Diego, p.104, 1995)

1569 K. Lee, H. Seed, *J. Soil Mech. Foundation Divn. ASCE* 93, 117 (1967)

1570 R. B. Leighton, B.C. Murray, *Science*, 153, 136 (1966)

1571 L. A. Leshin, P. R. Mahaffy, C. R. Webster, M. Cabane, P. Coll, P. G. Conrad, P. D. Archer Jr., S. K.  
1572 Atreya, A. E. Brunner, A. Buch, J. L. Eigenbrode, G. J. Flesch, H. B. Franz, C. Freissinet, D. P. Glavin,  
1573 A. C. McAdam, K. E. Miller, D. W. Ming, R. V. Morris, R. Navarro-González, P. B. Niles, T. Owen,  
1574 R. O. Pepin, S. Squyres, A. Steele, J. C. Stern, R. E. Summons, D. Y. Sumner, B. Sutter, C. Szopa, S.  
1575 Teinturier, M. G. Trainer, J. J. Wray, J. P. Grotzinger and MSL Science Team, *Science*, 341, (2013)  
1576 doi:10.1126/science.1238937

1577 Y. Liang, J. D. Price, D. A. Ward, E. B. Watson, *J. Geophys. Res.* 106, 529 (2001)

1578 R. Lichtenheldt, *Lokomotorische Interaktion planetarer Explorationssysteme mit weichen Sandböden*  
1579 (Verlag Dr. Hut, ISBN 978-3-8439-2704-8, Munich, 2016)

1580 P. Lognonné, B. Mosser, *Surv. Geophys.* 14, 239 (1993)

1581 P. Lognonné, M. Le Feuvre, C. L. Johnson, R. C. Weber, *J. Geophys. Res.* 114, E12003 (2009)  
1582 doi:10.1029/2008JE003294

1583 A. Lorek, N. Wagner, *Cryosphere*, 7, 1839 (2013) doi:10.5194/tc-7-1839-2013

1584 L. Malagnini, *Bull. Seism. Soc. Am.*, 86, 1471 (1996)

1585 L. Malagnini, R. B. Herrmann, G. Biella, R. de Franco, *Bull. Seism. Soc. Am.*, 85, 900 (1995)

1586 N. Mark, G. H. Sutton, *J. Geophys. Res.*, 80, 4932 (1975)

1587 F. J. Martin-Torres, M.-P. Zorzano, P. Valentin-Serrano, A.-M. Harri, M. Genzer, O. Kemooinen, E. G.  
1588 Rivera-Valentin, I. Jun, J. Wray, M. B. Madsen, W. Goetz, A. S. McEwen, C. Hardgrove, N. Renno,  
1589 V. F. Chevrier, M. Mischna, R. Navarro-González, J. Martinez-Frías, P. Conrad, T. McConnochie, C.  
1590 Cockell, G. Berger, A. R. Vasavada, D. Sumner, David. Vaniman, *Nature Geosci.* 8, 357 (2015)  
1591 doi:10.1038/ngeo2412

1592 G. M. Martinez, N. Rennó, E. Fischer, C. S. Borlina, B. Hallet, M. De la Torre Juárez, A. R. Vasavada, M.  
 1593 Ramos, V. Hamilton, J. Gomez-Elvira, R. M. Haberle, *J Geophys Res Planets* 119, 1822, (2014)  
 1594 doi:10.1002/2014JE004618  
 1595 G. M. Martinez, A. De-Vicente-Retortillo, A. G. Fairén, E. Fischer, S. D. Guzewich, R, M, Haberle, H.  
 1596 Kahanpää, O. Kempainen, M. Lemmon, C. Newman, N. Renno, M. Richardson, M. D. Smith, M. Torre-  
 1597 Juárez, A. Vasavada, *Space Sci Rev* 212, 295 (2017) doi:10.1007/s11214-017-0360-x  
 1598 W. J. Massmann, *J. Geophys. Res.* 111, (2006) doi:10.1029/2006JG000163.  
 1599 J. Massmann, D. F. Farrier, *Water Resources Res.*, 28, 777 (1992)  
 1600 I. O. McGlynn, C. M. Fedo, H. Y. McSween Jr., *J. Geophys. Res.*, 116, E00F22, (2011)  
 1601 doi:10.1029/2010JE003712.  
 1602 D. S. McKay J. L. Carter W. W. Boles C. Allen C., J. Allton J., *Engineering, Construction, and Operations*  
 1603 *in Space IV American Society of Civil Engineers*, p. 857 (1994)  
 1604 M. Mehta, N. O. Renno, J. Marshall, M. R. Grover, A. Sengupta, N. A. Rusche, J. F. Kok, R. E. Arvidson,  
 1605 W. J. Markiewicz, M. T. Lemmon, P. H. Smith, *Icarus* 211, 172 (2011)  
 1606 doi:10.1016/j.icarus.2010.10.003  
 1607 M. Mehta, A. Sengupta, N. O. Rennó, J. W. Norman, P. G. Van, Huseman, D. S. Gulick, M. Pokora,  
 1608 M., *AIAA J.* 51, 2800 (2013) doi:10.2514/1.J052408  
 1609 H. J. Melosh, H. J., *Impact Craters, A Geologic Process* (Oxford University Press, London, 1989)  
 1610 M. T. Mellon, B.M. Jakosky, H.H. Kieffer, P.R. Christensen, *Icarus* 148, 437–455 (2000)  
 1611 M. T. Mellon, R. L. Fergason, N. E. Putzig, in *The Martian Surface: Composition, Mineralogy and Physical*  
 1612 *Properties*, ed. by J.F. Bell III (Cambridge University Press, Cambridge, Chap. 19, p. 399, 2008)  
 1613 P.-Y. Meslin, O. Gasnault, O. Forni, S. Schröder, A. Cousin, G. Berger, S. M. Clegg, J. Lasue, S. Maurice,  
 1614 V. Sautter, S. Le Mouélic, R. C. Wiens, C. Fabre, W. Goetz, D. Bish, N. Mangold, B. Ehlmann, N.  
 1615 Lanza, A.-M. Harri, R. Anderson, E. Rampe, T. H. McConnochie, P. Pinet, D. Blaney, R. Lévillé, D.  
 1616 Archer, B. Barraclough, S. Bender, D. Blake, J. G. Blank, N. Bridges, B. C. Clark, L. DeFlores, D.  
 1617 Delapp, G. Dromart, M. D. Dyar, M. Fisk, B. Gondet, J. Grotzinger, K. Herkenhoff, J. Johnson, J.-L.  
 1618 Lacour, Y. Langevin, L. Leshin, E. Lewin, M. B. Madsen, N. Melikechi, A. Mezzacappa, M. A. Mischna,  
 1619 J. E. Moores, H. Newsom, A. Ollila, R. Perez, N. Renno, J.-B. Sirven, R. Tokar, M. de la Torre, L.  
 1620 d’Uston, D. Vaniman, A. Yingst and MSL Science Team, *Science*, 341 (2013)  
 1621 doi:10.1125/science.128670  
 1622 R. E. Milliken, J.F. Mustard, F. Poulet, D. Jouglet, J.-P. Bibring, B. Gondet and Y. Langevin, *J. Geophys.*  
 1623 *Res.*, 112, E08S07 (2007) doi:10.1029/2006JE002853

1624 D. Mimoun, D. Murdoch, P. Lognonné, K. Hurst, W. T. Pike, J. Hurley, T. Nébut, W. B. Banerdt and  
1625 the SEIS Team, *Space Sci. Rev.* 211, 383 (2017) doi:10.1007/s11214-017-0409-x

1626 D. T. F. Möhlmann, *Icarus* 168, 318 (2004) doi:10.1016/j.icarus.2003.11.008

1627 D. T. F. Möhlmann, *Icarus* 195, 131 (2008) doi:10.1016/j.icarus.2007.11.026

1628 H. J. Moore, B.M. Jakosky, *Icarus* 81, 164 (1989)

1629 H. J. Moore, R. E. Hutton, G. D. Clow, C. R. Spitzer, USGS Prof. Paper 1389, 222pp., 2 plates (1987)

1630 H. J. Moore, R. E. Hutton, R. F. Scott, C. R. Spitzer, R. W. Shorthill, *J. Geophys. Res.* 82, 4497 (1977)

1631 H. J. Moore, D. B. Bickler, J. A. Crisp, H. J. Eisen, J. A. Gensler, A. F. C. Haldemann, J. R. Matijevic,  
1632 L. K. Reid, F. Pavlics, *J. Geophys. Res.* 104, 8729 (1999)

1633 P. Morgan, S. E. Smrekar, R. Lorenz, M. Grott, O. Kroemer, N. Müller, *Space Sci. Rev.* 211, 277 (2017)  
1634 doi:10.1007/s11214-017-0388-y

1635 K. Mueller, M. P. Golombek, *Ann. Rev. Earth Planet. Sci.* 32, 435 (2004)

1636 N. Murdoch, B. Kenda, T. Kawamura, A. Spiga, P. Lognonné, D. Mimoun, W. B. Banerdt, *Space Sci.*  
1637 *Rev.* 211, 457 (2017a) doi:10.1007/s11214-017-0343-y

1638 N. Murdoch, D Mimoun, R. F. Garcia, W. Rapin, T. Kawamura, P. Lognonné, D. Banfield, W. B. Banfield,  
1639 *Space Sci. Rev.* 211,429 (2017b) doi:10.1007/s11214-016-0311-y

1640 Y. Nakamura, J. Dorman, F. Duennebier, D. Lammlein, G. Latham, *The Moon*, 13, 57 (1975)

1641 Y. Nakamura, *Bull. Seism. Soc. Am.*, 66, 593 (1976)

1642 Y. Nakamura, J. Koyama, *J. Geophys. Res.*, 87, 4855 (1982)

1643 Y. Nakamura, F. Duennebier, G. Latham, F. Dorman, *J. Geophys. Res.* 81, 4818 (1976)

1644 R. Nave, 2016, Mean Free Path, Hyperphysics (website hosted by Dept. Physics and Astronomy, Georgia  
1645 State Univ. 2016, <http://hyperphysics.phy-astr.gsu.edu/hbase/Kinetic/menfre.html>. ( last accessed  
1646 2017-3-13).

1647 G. Neugebauer, G. Münch, H. Kieffer, S. C. Chase Jr, E. Miner, *Astron. J.* 76, 719 (1969)

1648 R. H. Nilson, E. W. Peterson, K. H. Lie, N. R., Burkhard, J. R. Hearst, *J. Geophys. Res.*, 96, 21,933 (1991)

1649 S. A. Nowicki, P.R. Christensen, *J. Geophys. Res.* 112, E05007 (2007). doi:10.1029/2006JE002798

1650 Y. Ohsaki, R. Iwasaki, *Soils and Foundations*, 13, 61 (1973)

1651 F. D. Palluconi, H.H. Kieffer, *Icarus* 45, 415 (1981)

1652 B. I. Pandit, D. C. Tozer, *Nature*, 226, 335 (1970)

1653 S. Parolai, D. Bindi, A. Ansal, A. Kurtulus, A. Strollo, J. Zschau, *Geophys. J. Int.* 181, 1147 (2010)  
1654 doi:10.1111/j.1365-246X.2010.04567.

1655 M. D. Paton, A.-M Harri, H. Savijärvi, T. Mäkinen, A. Hagermann, O. Kempainen, A. Johnston, *Icarus*  
1656 271, 360 (2016)

1657 W. T. Pike, U. Staufer, M. H. Hecht, W. Goetz, D. Parrat, H. Sykulska-Lawrence, S. Vijendran, M. B.  
1658 Madsen, *Geophysical Research Letters*, 38, L24201 (2011) doi:10.1029/2011GL049896

1659 C. C. Pilbeam, J. R. Vaišnys, *J. Geophys. Res.* 78, 810 (1973)

1660 S. Piqueux, P. R. Christensen, *J. Geophys. Res.* 114, E09005 (2009a) doi:10.1029/2008je003308.

1661 S. Piqueux, P. R. Christensen, *J. Geophys. Res.* 114, E09006 (2009b). doi:10.1029/2008je003309

1662 S. Piqueux, P. R. Christensen, *J. Geophys. Res.* 116, E07004 (2011) doi: 10.1029/2011je003805.

1663 S. Planke, E. Alvestad, O. Eldholm, *The Leading Edge*, 18, 342 (1999)

1664 A.-C. Plesa, M. Grott, M. T. Lemmon, N. Müller, N. Piqueux, M. A. Siegler, S. E. Smrekar, T. Spohn, J.  
1665 *Geophys. Res. Planet.* 121, 2166 (2016) doi:10.1002/2016JE005127.

1666 L. K. Pleskot, E.D. Miner, *Icarus* 45, 179 (1981) Smith

1667 M. Prasad, R. Meissner, *Geophysics*, 57, 710 (1992)

1668 M. Prasad, M.A. Zimmer, P.A. Berge, B.P. Bonner, Tech. Rep. UCRL-JRNL-205155 (Lawrence Livermore  
1669 National Laboratory, USA, 2004)

1670 M. A. Presley, P. R. Christensen (1997a), *J. Geophys. Res.* 102, 9221 (1997a) doi:10.1029/97JE00271.

1671 M. A. Presley, P. R. Christensen (1997b), *J. Geophys. Res.* 102, 6551 (1997b)

1672 N. E. Putzig, PhD Thesis (University of Colorado, Boulder, 2006)

1673 N. E. Putzig, M.T. Mellon, *Icarus* 191, 68 (2007) doi:10.1016/j.icarus.2007.1005.1013

1674 N. E Putzig, N. E. Mellon, R.E. Arvidson, K.A. Kretke, 2005, *Icarus* 173, 325 (2005)

1675 A. Revil, D. Grauls, O. Brévar, *J. Geophys. Res.*, 107, 2293, (2002) doi:10.1029/2001JB000318, 2002.

1676 R. A. Robie, B. S. Hemingway, W. H. Wilson, *Science*, 167, 749 (1970)  
1677 doi:10.1126/science.167.3918.749.

1678 A. Robinson, J. Gluyas, *Marine and Petroleum Geology* 9, 319 (1992)

1679 J. Rossabi, in C. Ho, S. Webb, eds., *Gas Transport in Porous Media* (Springer, Ch. 16, 279, 2006)

1680 J. Rossabi, R. W. Falta, *Ground Water*, 40, 67 (2002)

1681 S. Roy, R. Raju, H. F. Chuang, B. A. Cruden, M. Meyyappan, *J. Appl. Phys.* 93, 4870 (2003)

1682 S. W. Ruff, P.R. Christensen, 2002, *J. Geophys. Res.* 107, 5127 (2002) doi:10.1029/2001JE001580

1683 S. W. Ruff, P. R. Christensen, D. L. Blaney, W. H. Farrand, J. R. Johnson, J. R. Michalski, J. E. Moersch,  
1684 S. P. Wright, S. W. Squyres, *J. Geophys. Res.*, 111, E12S18 (2006) doi:10.1029/2006JE002747

1685 N. Sakatani, K. Ogawa Y. Iijima M. Arakawa S. Tanaka S., 2016, *Icarus* 267, 1 (2016)  
1686 doi.org/10.1016/j.icarus.2015.12.012

- 1687 J. C. Santamarina, K. A. Klein, M. A. Fam, *Soils and waves* (Wiley, New-York, 2001)
- 1688 B. R. Scanlon, J. P. Nicot, J. W. Massmann, in *Soil Physics Companion*, A. W. Warrick, ed. (CRC Press,  
1689 Chap. 8, p. 297 2002) doi: 10.1201/9781420041651.
- 1690 E. Schreiber, *Proc. 8<sup>th</sup> Lun. Sci. Conf.* 1201 (1977)
- 1691 R. F. Scott, *Géotechnique*, 37, 423 (1987)
- 1692 C. Sens-Schönfelder, E. Larose, *Earthquake Sci.* 23, 519 (2010) doi:10.1007/s11589-010-0750-6
- 1693 A. Shaw, R. E. Arvidson, R. Bonitz, J. Carsten, H. U. Keller, M. T. Lemmon, M. T. Mellon, M. Robinson,  
1694 A. Trebi-Ollenu, *J. Geophys. Res.*, 114, E00E05 (2009) doi:10.1029/2009JE003455.
- 1695 E. M. Shoemaker, E.C. Morris, *Thickness of the regolith*, in *Surveyor: Program Results*, (NASA Special  
1696 Paper, v. 184 p. 96, U.S. Government Printing Office, Washington, 1969)
- 1697 D. E. Smith, M. T. Zuber, H. Frey J. B. Garvin. J. W. Head, D. O. Muhleman, G. H. Pettengill, R. J.  
1698 Phillips, S. C. Solomon, H. J. Zwally, W. B. Banerdt, T. C. Duxbury, M. P. Golombek, F. G. Lemoine,  
1699 G. A. Neumann, D. D. Rowlands, O. Aharonson, P. G. Ford, A. B. Ivanov, C. L. Johnson, P. J.  
1700 McGovern, J. B. Abshire, R. S. Afzal, X. Sun, *J. Geophys. Res.* 106, 23,689 (2001)
- 1701 P. H. Smith, L. Tamppari, R. E. Arvidson, D. Bass, D. Blaney, W. Boynton, A. Carswell, D. Catling, B.  
1702 Clark, T. Duck, T. Duck, E. Dejong, D. Fisher, W. Goetz, P. Gunnlaugsson, M. Hecht, V. Hipkin, J.  
1703 Hoffman, S. Hviid, H. Keller, S. Kounaves, C. F. Lange, M. Lemmon, M. Madsen, M. Malin, W.  
1704 Markiewicz, J. Marshall, C. McKay, M. Mellon, D. Michelangeli, D. Ming, R. Morris, N. Renno, W. T.  
1705 Pike, U. Staufer, C. Stoker, P. Taylor, J. Whiteway, S. Young, A. Zent, *J. Geophys. Res.*, 113, E00A18  
1706 (2009) DOI:10.1029/2008JE003083, 16 pp.
- 1707 S. W. Squyres, R. E. Arvidson, J. F. Bell III, J. Brückner, N. A. Cabrol, W. Calvin, M. H. Carr, P. R.  
1708 Chtritensen, B. C. Clark, L. Crumpler, D. J. Des Marais, C. d’Uston, T. Economou, J. Farmer, F.  
1709 Farrand, W. Folkner, M. Golombek, S. Gorevan, J. A. Grant, R. Greeley, J. Grotzonger, L. Haskin, K.  
1710 E. Herkenhoff, S. Hviid, J. Johnson, G. Klingelhöfer, A. Knoll, G. Landis, M. Lemmon, R. Li, M. B.  
1711 madsen, M. C. Malin, S. M. McLennan, H. Y. McSween, D. W. ming, J. Moersch, R. V. Morris, T.  
1712 Parker, J. W. Rice Jr, L. Richter, R. Rieder, M. Sims, M. Smith, P. Smith, L. A. Soderblom, R. Sullivan,  
1713 H. Wänke, T. Wdowiak, M. Wolff, A. Yen, 2004, *Science* 305, 794 (2004) doi:10.1126/science.1100194
- 1714 L. Soderblom, R. C. Anderson, R. E. Arvidson, J. F. Bell III, N. A. Cabrol, W. Calvin, P. R. Christensen,  
1715 B. C. Clark, T. Economou, B. L. Ehlmann, W. H. Farrand, D. Fike, R. Gellert, T. D. Glotch, M. P.  
1716 Golombek, R. Greeley, J. P. Grotzonger, K. E. Herkenhoff, D. J. jerolmack, J. R. Johnson, B. Jolliff,  
1717 G. Klingelhöfer, A. H. Knoll, Z. A. Learner, R. Li, M. C. Malin, S. M. McLennan, H. Y. McSween, D.

1718 W. Ming, R. V. Morris, J. W. Rice Jr, L. Richter, R. Rieder, D. Rodionov, C. Schröder, F. P. Seelos  
1719 IV, J. M. Soderblom, S. W. Squyres, R. Sullivan, W. A. Watters, C. M. Weitz, M. B. Wyatt, A. Yen,  
1720 J. Zipfel, *Science* 306, 1723 (2004)

1721 D. Sollberger, C. Schmelzbach, J. O. A. Robertsson, S. A. Greenhalgh, Y. Nakamura, A. Khan, *Geophys.*  
1722 *Res. Lett.*, 43 (2016) doi:10.1002/2016GL070883

1723 S. Stanchits, S. Vinciguerra, G. Dresen, *Pure Appl. Geophys.* 163, 974 (2006) doi:10.1007/s00024-006-  
1724 0059-5

1725 R. Sullivan, R. Anderson, J. Biesiadecki, T. Bond, H. Stewart, *J. Geophys. Res.*, 116, E02006 (2011)  
1726 doi:10.1029/2010JE003625.

1727 G. H. Sutton, F. K. Duennebieer, *J. Geophys. Res.*, 75, 7439 (1970)

1728 Z. Tan, 2014, Basic properties of gases, in *Air Pollution and Greenhouse Gases, From Basic Concepts to*  
1729 *Engineering Applications for Air Emission Control* (Springer, Singapore, p. 27, 2014)  
1730 [http://www.springer.com/cda/content/document/cda\\_downloaddocument/9789812872111-](http://www.springer.com/cda/content/document/cda_downloaddocument/9789812872111-c2.pdf?SGWID=0-0-45-1486659-p176923844)  
1731 [c2.pdf?SGWID=0-0-45-1486659-p176923844](http://www.springer.com/cda/content/document/cda_downloaddocument/9789812872111-c2.pdf?SGWID=0-0-45-1486659-p176923844) (pdf download; last accesses 2017-3-15).

1732 T. Tanaka, J. A. Skinner, J. M. Dohm, R. P. Irwin III, E. J. Kolb, C. M. Fortezzo, T. Platz, G. G. Michael,  
1733 T. M. Hare, *Geologic Map of Mars*. (U.S. Geol. Surv. Sci. Invest. Map 3292, 2014)

1734 T. Tanimoto, M. Eitzel, T. Yano, *J. Geophys. Res.* 113, E08011 (2008) doi:10.1029/2007JE003016

1735 N. Teanby, J. Stevanović, J. Wookey, N. Murdoch, J. Hurley, R. Myhill, N. E. Bowles, S. B. Calcutt, W.  
1736 T. Pike, *Space Sci. Rev.* ??, ??? (2016) doi:10.1007/s11214-016-0310-z

1737 B. R. Tittmann, *Phil. Trans. R. Soc. Lond. A*, 285, 475 (1977)

1738 B. R. Tittmann, M. Abdel-Gawad, R. M. Housley, in *Proc. 3rd Lunar Sci. Conf.* p. 2565 (1972)

1739 B. R. Tittmann, H. Nadler, V. Clark, L. Coombe, in *Proc. 10th Lunar Planet. Sci. Conf.* p. 2131 (1979)

1740 B. R. Tittmann, V. A. Clark, J. M. Richardson, T. W. Spencer, *J. Geophys. Res.* 85, 5199 (1980)

1741 N. M. Toksöz, D. H. Johnson, A. Timur, *Geophysics*, 44, 681 (1979)

1742 N. J. Tosca, S. M. McLennan, D. H. Lindsley, M. A. A. Schoonen, *J. Geophys. Res.*, 109, E05003 (2004)  
1743 doi:10.1029/2003JE002218.

1744 O. Uyanik, (2010) *Int. J. Phys. Sci.*, 5, 1034 (2010)

1745 A. R. Vasavada, D. A. Paige, S. E. Wood, *Icarus*, 141, 179 (1999) doi:110.1006/icar.1999.6175.

1746 A. R. Vasavada, S. Piqueux, K. W. Lewis, M. T. Lemmon, M. D. Smith, *Icarus* 284, 372 (2017)

1747 D. Velea, F. D. Shields, J. M. Sabatier, *Soil Sci. Soc. Am. J.*, 64, 1226 (2000)

1748 V. Vesovic, W. A. Wakeham, G. A. Olchoway, J. V. Sengers, J. T. R. Watson, J. Millar, *J. Phys. Chem.*  
1749 *Ref. Data*, 19, 763 (1990)

- 1750 S. Vinciguerra, C. Trovato, P.G. Meredith, P.M. Benson, *Int. J. Rock Mech. Min. Sci.*, 42, 900 (2005)  
1751 doi:10.1016/j.ijrmms.2005.05.022
- 1752 C. Vrettos, A. Becker, K. Merz, L. Witte, *Earth and Space 2014, 14th ASCE International Conference on*  
1753 *Engineering, Science, Construction and Operations in Challenging Environments (2014)*
- 1754 N. H. Warner, M.P. Golombek, C. Bloom, N. Wigton, C. Schwartz, 45th Lunar Planetary Science  
1755 Conference (Lunar and Planetary Institute, Houston, Abstract #2217, 2014)
- 1756 N. H. Warner, M.P. Golombek, J. Sweeney, A. Pivarunas, 47th Lunar Planetary Science Conference  
1757 (Lunar and Planetary Institute, Houston, Abstract #2231, 2016)
- 1758 N. H. Warner, M. P. Golombek, J. Sweeney, R. Fergason, R. Kirk, C. Schwartz, *Space Sci. Rev.* 211, 147  
1759 (2017) doi:10.1007/s11214-017-0352-x
- 1760 J. S. Watkins, R. Kovach, *Science* 175, 1244 (1972)
- 1761 J. S. Watkins, R. Kovach, *Geochim. Cosmochim. Acta (Suppl.)* 3, 2561 (1973)
- 1762 J. S. Watkins, L. A. Walters, R. H. Godson, *Geophysics* 37, 29 (1972)
- 1763 S. Whitaker, *Transp. Porous Med.* 25, 27 (1996)
- 1764 B. B. Wilcox, M.S. Robinson, P.C. Thomas, B.R. Hawkes, *Meteor. Planet. Sci.* 40, 695 (2005)  
1765 D. F. Winter, J. M. Saari, *Astrophys. J.* 156, 1135 (1969) doi:10.1086/150041.
- 1766 A. Yen, R. Gellert, C. Schröder, R. V. Morris, J. F. Bell III, A. T. Knudson, B. C. Clark, D. W. Ming, J. A.  
1767 Crisp, R. E. Arvidson, D. Blaney, J. Brückner, P. R. Christensen, D. J. DesMarais, P. A. de Souza Jr,  
1768 T. E. Economou, A. Ghosh, B. C. Hahn, K. E. Herkenhoff, L. A. Haskin, J. A. Hurowitz, B. L. Joliff,  
1769 J. R. Johnson, G. Klingelhöfer, M. B. Madsen, S. M. McLennan, H. Y. McSween, L. Richter, R.  
1770 Rieder, D. Rodionov, L. Soderblom, S. W. Squyres, N. J. Tosca, A. Wang, M. Wyatt, J. Zipfel, (2005).  
1771 *Nature*, 436, 49 (2005) doi:10.1038/nature03637
- 1772 K. Yomogida, T. Matsui, *J. Geophys. Res.* 88, 9513 (1983)
- 1773 A. S. Ziarani, R. Aguilera, 2012, *Transp. Porous Med.*, 91, 239 (2012) doi:10.1007/s11242-011-9842-6.
- 1774 M. A. Zimmer, M. Prasad, G. Mavko, *The Leading Edge* 21, 178 (2002) doi:10.1190/1.1452609
- 1775 M. A. Zimmer, M. Prasad, G. Mavko, A. Nur, *Geophysics*, 72, E1 (2007) doi:10.1190/1.2399459

1776

## 8. Appendix

1777

Soil mechanical parameters, definitions, and units. Units indicated by empty brackets are dimensionless.

Parameter	Notation - definition	Unit
Volume of the voids	$V_v$	m <sup>3</sup>
Volume of the solid grains	$V_s$	m <sup>3</sup>
Volume of the soil	$V = V_v + V_s$	m <sup>3</sup>
Mass of the solid grains	$M_s$	kg
Mass of the soil	$M$ ( $M = M_s$ in dry soils)	kg
Specific gravity of the grains	$\rho_s$	kg/m <sup>3</sup>
Bulk density of the soil	$\rho$	kg/m <sup>3</sup>
Void ratio (pores between the grains)	$e = V_v / V_s = n / (1 - n)$	[ ]
Porosity	$n = V_v / (V_v + V_s) = e / (1 + e) = 1 - (\rho_b / \rho_s)$	[ ]
Unit mass of the soil (bulk density)	$\rho = M / V = \rho_s(1 - n)$	kg/m <sup>3</sup>
Maximum void ratio (minimum bulk)	$e_{max}$	[ ]
Minimum void ratio (maximum bulk)	$e_{min}$	[ ]
Relative density (or density index)	$D_r = (e_{max} - e) / (e_{max} - e_{min})$	%
$D_{60}$ (from grain size distribution curve)	60% of the grains have diameter smaller than	μm
$D_{10}$ (from grain size distribution curve)	10% of the grains have diameter smaller than	μm
Angle of internal friction	$\phi$ Shear strength parameter	°
Strain	$\varepsilon$	[ ]
Young's modulus	$E$	[ ]
Poisson's ratio	$\nu$	[ ]
Compressional wave velocity	$v_p$	m/s
Shear wave velocity	$v_s$	m/s
Seismic quality factor	$Q$	[ ]

1778